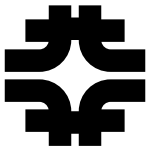

Fermi National Accelerator Laboratory

FERMILAB-FN-641
D0

The D0 Upgrade: Forward Preshower, Muon System and Level 2 Trigger

S. Abachi et al.
The D0 Collaboration

Fermi National Accelerator Laboratory
P.O. Box 500, Batavia, Illinois 60510

April 1996

Operated by Universities Research Association Inc. under Contract No. DE-AC02-76CHO3000 with the United States Department of Energy

Disclaimer

Contents

1 Introduction

The goal of the DØ Upgrade[1] is to exploit fully the potential of the Tevatron Collider in the high luminosity Main Injector environment. With an integrated luminosity of 2 fb^{-1} accumulated at up to $2 \times 10^{32}\,\text{cm}^{-2}\text{s}^{-1}$, the detector will be capable of:

- Precise studies of large-statistics samples of the top quark, including single-top production;
- Precision electroweak measurements including the mass of the W and $\sin^2\theta_W$ for light quarks, and studies of multi-boson production;
- Measurements of QCD processes with large statistics in new regions of phase space (large η, large E_T) and with new probes ($W/Z/\gamma+\text{jets}$), as pioneered by DØ in Run I;
- Powerful searches for physics beyond the Standard Model: DØ currently has the world's best mass limits on the squarks, gluinos and light stop quark of supersymmetric models, and on the mass of a new heavy W boson;
- A well-focused B-physics program including CP violation in the $B \to J/\psi K_S^0$ system, B_s mixing, heavy quark spectroscopy (B_c, Λ_b, etc.) and rare decays.

The DØ detector has proved to be an excellent instrument for the study of the Standard Model. Its finely segmented calorimeter and large angular coverage for electron and muon identification and measurement have enabled a wide range of physics studies to be addressed in Run I[2]. The upgrade program aims to maintain this excellent performance during the Main Injector era, when the Tevatron luminosity will be increased by a factor of 10 to $2 \times 10^{32}\,\text{cm}^{-2}\text{s}^{-1}$ and the bunch spacing will be reduced from the present 3.6 μs to 396 ns, and eventually 132 ns. Further, the upgrade will significantly enhance the capabilities of the detector:

- b-quark decays will be tagged using displaced vertices in the silicon tracker;
- muon identification and triggering will be enhanced, especially at low p_T;
- electron identification and triggering will be improved using preshower detectors and magnetic central tracking, and electron charge will be determined.

The architecture of the upgraded DØ detector is ideally suited to operation at a high-luminosity hadron collider, because:

- the calorimeter-based triggering and electron-identification strategies are relatively insensitive to luminosity;
- the small decay volume and thick calorimeter keep muon trigger rates to a minimum;
- uniform tracking, electron and muon coverage extends out to $\eta \sim 2 - 2.5$;
- integrated forward shielding provides an elegant way of ameliorating the problem of particle backgrounds in the muon system.

The baseline cost of the DØ Upgrade was established by a Director's Review in early 1995, and the project was endorsed by the PAC at its April 1995 meeting. The scope of the upgrade remains unchanged since then, and indeed since originally proposed in 1990. In this document we present information on three of the subsystems of the upgrade: the Forward Preshower, the Muon System and the Level 2 Trigger. Our understanding of these systems has evolved considerably over the last year. This has led to a modest increase (about 10%) in the baseline cost estimate.

The Forward Preshower detector is essential for electron triggering in the region $1.4 \lesssim |\eta| \lesssim 2.5$. Detailed Monte Carlo simulations of this detector have confirmed its performance and enabled us to establish the specifications, develop a construction strategy, and fix the costs.

The muon system design is driven by the observation (presented at the Aspen PAC meeting in 1995) that the present proportional drift tubes deteriorate too rapidly with integrated luminosity to be used in the forward region in Run II. We have developed an integrated solution that will replace the forward drift tubes with plastic mini-drift tube planes, incorporate scintillator planes for triggering over all η, and combine the present forward muon iron absorber with additional hermetic shielding around the beamline to minimize particle backgrounds in the muon system.

It has always been realized that a Level 2 trigger system would be essential to provide adequate rejection and achieve reasonable trigger rates in the upgrade. Over the last year, our understanding of the Level 2 system has benefited from simulations of the expected trigger rates including multiple interactions at high luminosities. We have concluded that significant computational power will be needed at Level 2 to meet our bandwidth goals at luminosities of $\mathcal{L} = 2 \times 10^{32}\,\mathrm{cm}^{-2}\mathrm{s}^{-1}$.

This document summarizes and extends the information presented to the PAC in January 1996, and addresses the concerns raised at that meeting. We seek the approval of the PAC for these three subsystems, so that the review process may be brought to a conclusion and we may embark on the challenging but exciting task of preparing the DØ Upgrade detector for the physics questions of the next century. We note that a full technical, cost and management review of the project by the Department of Energy is scheduled for May 7–9, 1996.

2 Importance of Forward Leptons

The ability to trigger on, identify and measure electrons and muons in the forward region ($\eta \gtrsim 1$) is an important strength of the present DØ detector. For the upgrade we aim to maintain and enhance this capability. Both the forward preshower detector and the muon system upgrade are crucial parts of this strategy. Before describing these detectors, it is therefore worth reviewing the importance of forward lepton detection.

Most physics measurements will benefit from the increased acceptance that forward coverage provides compared to the acceptance of the central calorimeter and muon system alone. For some of the most interesting physics processes it is essential. In the following we list some examples.

2.1 Top and W-pair production

The range in pseudorapidity η for leptons from top and WW events is shown in figure 1 [6]. Increasing the $|\eta|$ coverage from 1.0 to 2.0 significantly increases the geometric detection efficiency from 50% to 90% for leptons from W decay in top events. The $|\eta|$ distribution of b-jets is essentially the same as for the leptons, so the same efficiency gains are realized for μ-tagging of b's. Similarly, the acceptance rises from 35% to 80% for WW events.

2.2 Lepton Charge Asymmetry in W Decays

Two effects contribute to the observed lepton charge asymmetry from the decay of W bosons produced in $p\overline{p}$ collisions. There is a production asymmetry due to the different momentum distributions of u and d quarks in the proton. W^+ bosons tend to be produced in the direction of the incoming protons and W^- bosons in the direction of the incoming anti-protons. Due to the $V-A$ coupling of the W bosons to leptons, the charged lepton from W^+ decays tend to be emitted against the direction of the incoming protons and vice-versa for W^- bosons. The second effect is exactly predicted by the Standard Model and the observed asymmetry

$$\mathcal{A} = \frac{N^+ - N^-}{N^+ + N^-},$$

where $N^{+/-}$ is the number of positively/negatively charged leptons, can be compared with predictions using different assumptions about the proton structure. It can also be used as an input to the fit for parton distributions

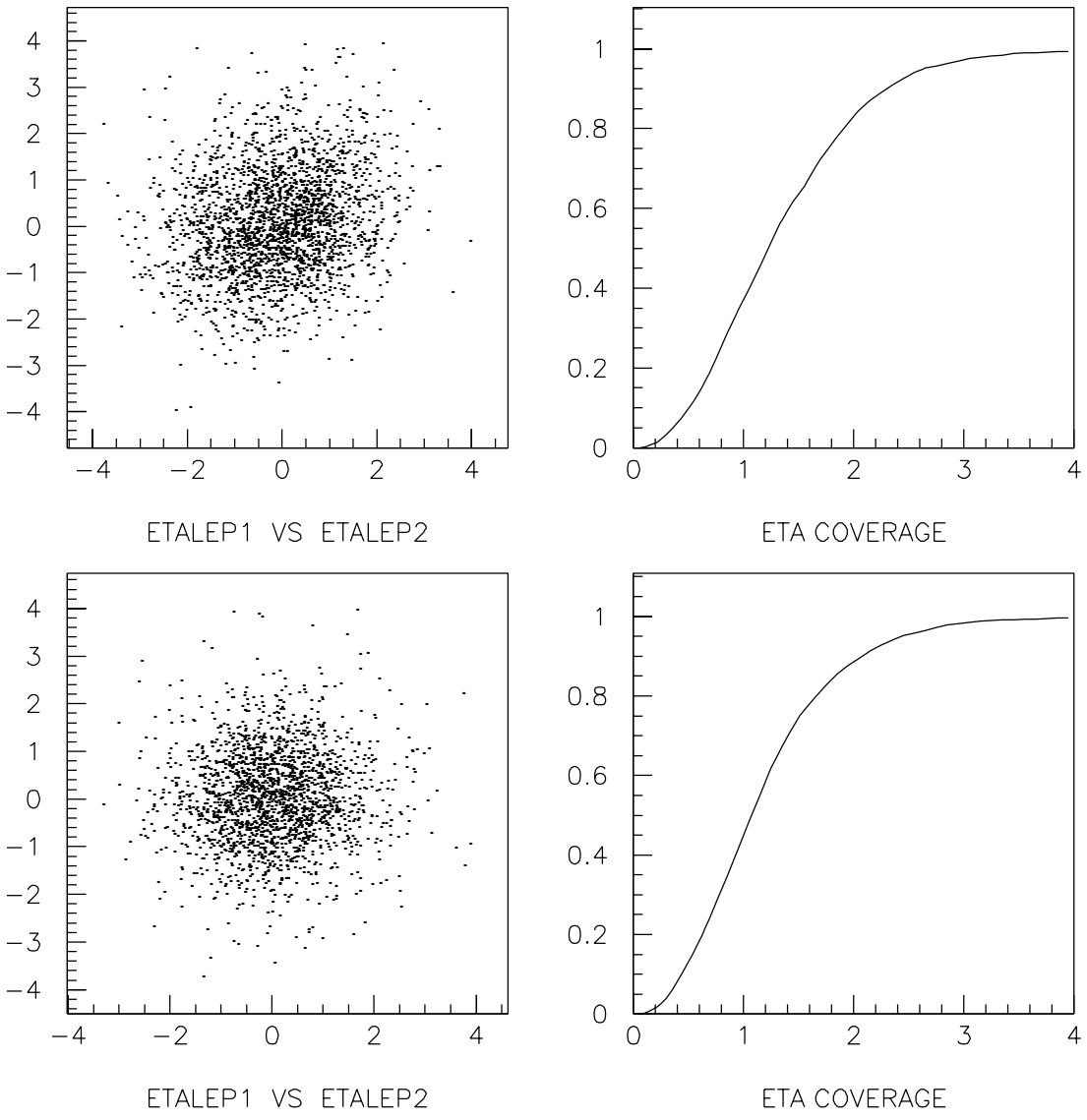

Figure 1: Shown (left upper and lower) are the $|\eta|$ distributions of leptons from the decay of W's in WW production (upper) and $t\bar{t}$ (M_{top} = 180 GeV/c^2)(lower). The efficiency as a function of $|\eta|$ coverage of the detector is shown (right).

of the proton. A precise knowledge of the distribution functions (u/d ratio) is required for a precise measurement of the W boson mass and for $\sin^2\theta_W$ from the forward-backward asymmetry in Z decays.

The upper plot in Fig. 2 shows $|\mathcal{A}|$ as a function of the lepton pseudorapidity $|\eta^{lepton}|$, predicted by two parton distributions (CTEQ2M [7], MRSD$-$ [8]). The lower plot shows the significance $\sqrt{\chi^2}$ with which the two can be distinguished as a function of the pseudorapidity coverage of the detector. Including forward leptons in the measurement increases the discrimination power by a factor of two.

The two parton distributions shown in Fig. 2 are already discriminated by the measurement performed by CDF using data from Run Ia [9]. The constraint on parton distributions from this measurement translates into an uncertainty in the W mass measurement of about 50 MeV. In Run II we aim to measure the W mass to better than 50 MeV, which means that a much tighter constraint on proton structure is required. We therefore need to measure the asymmetry $\mathcal{A}$ as precisely as possible in Run II, which suggests that we be able to trigger on electrons out to $|\eta| \approx 2.5$.

2.3 Forward-Backward Asymmetry in Z Decays

The process $p\overline{p} \rightarrow \ell^+\ell^-$ exhibits a forward-backward asymmetry in the charge of the leptons, which depends on the vector and axial vector couplings of the Z to quarks and leptons and is therefore sensitive to $\sin^2\theta_W$. With an integrated luminosity of 2 fb^{-1} a measurement of $\sin^2\theta_W$ can be obtained with a precision of 0.001[5]. The precision of this measurement is statistically limited and therefore the largest possible lepton acceptance is desirable. Figure 3 shows the acceptance for this process as a function of the pseudorapidity coverage for leptons. Including the forward region up to $|\eta| \approx 2.5$ more than doubles the acceptance. The largest systematic effect arises from the uncertainty in the ratio of u and d quarks in the proton. This can be constrained by the measurement of the lepton charge asymmetry in W decays, described in the previous section. By measuring the W mass, the forward-backward asymmetry in Z decays and the charge asymmetry in W decays in $p\overline{p}$ collisions, we can test the Standard Model while simultaneously reducing the uncertainty due to proton structure functions.

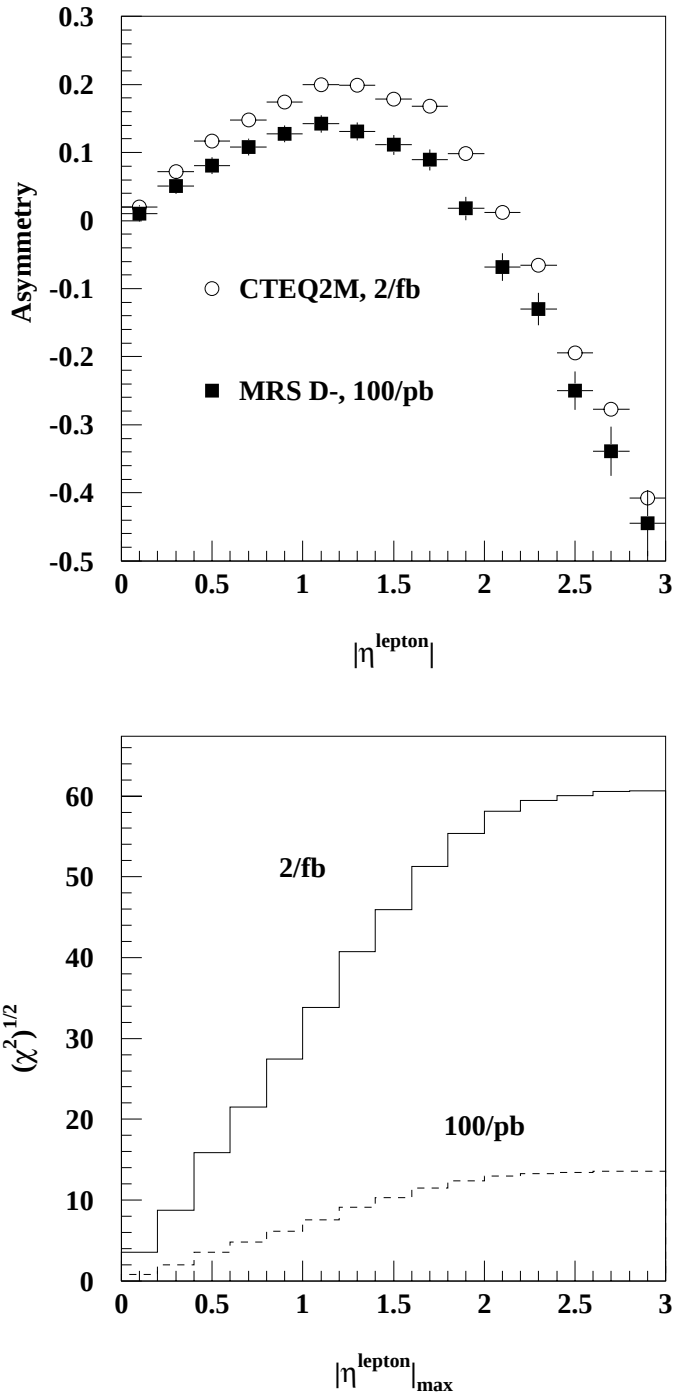

Figure 2: Top: lepton charge asymmetry predicted by CTEQ2M and MRSD− structure functions versus lepton pseudorapidity; bottom: significance with which the two curves can be distinguished for integrated luminosities of 2 and 100 pb^{-1}.

Figure 3: Acceptance for $Z \to \ell^+\ell^-$ decays versus pseudorapidity coverage for all decays (solid curve) and for decays in which both leptons have $p_T > 20$ GeV (dashed curve).

2.4 $W\gamma$ Production

All amplitudes for the process $q\overline{q} \to W\gamma$ vanish for a particular value of the scattering angle, θ^*, of the W boson in the $W\gamma$ rest frame[10],

$$\cos\theta^* = \pm\frac{1}{3}.$$

This effect is known as "radiation zero". Non-standard $WW\gamma$ couplings in general destroy this effect. Its observation therefore would be a powerful confirmation of the Standard Model.

In practice it is difficult to reconstruct θ^* because the neutrino from the decay of the W boson escapes unobserved. The best way to observe the radiation zero in Run II is through rapidity correlations between the charged lepton from the W decay and the photon. Figure 4 shows the expected rapidity difference between lepton and photon[3]. The dip at $\Delta y \approx -0.3$ is a manifestation of the radiation zero. Figure 5 shows a simulation of this distribution for a data sample of 1 fb^{-1}[4]. The left plot includes forward and central leptons and photons and a statistically significant dip is observable. The right plot includes only central leptons and photons and no statistically significant dip is observable. We conclude that again we must be able to trigger on forward leptons in order to be able to observe the radiation zero in $W\gamma$ production in Run II.

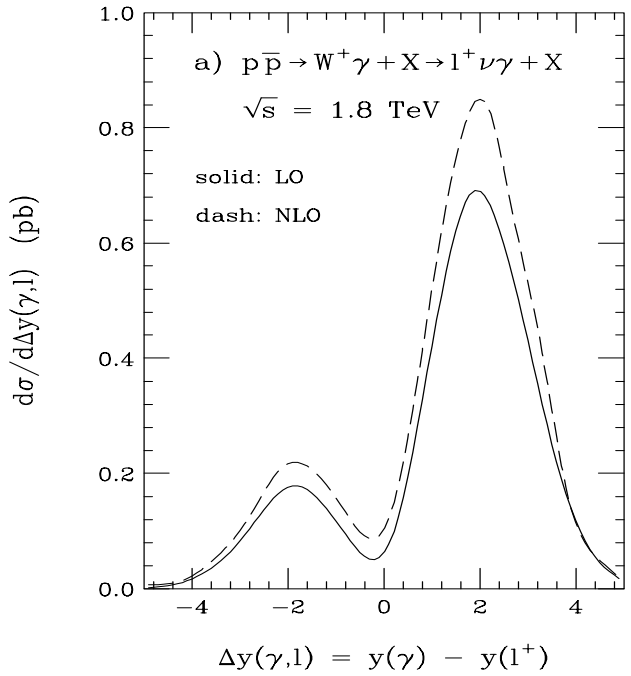

Figure 4: Predicted rapidity difference between charged lepton and photon in $W(\to \ell\nu) + \gamma$ production at the Tevatron.

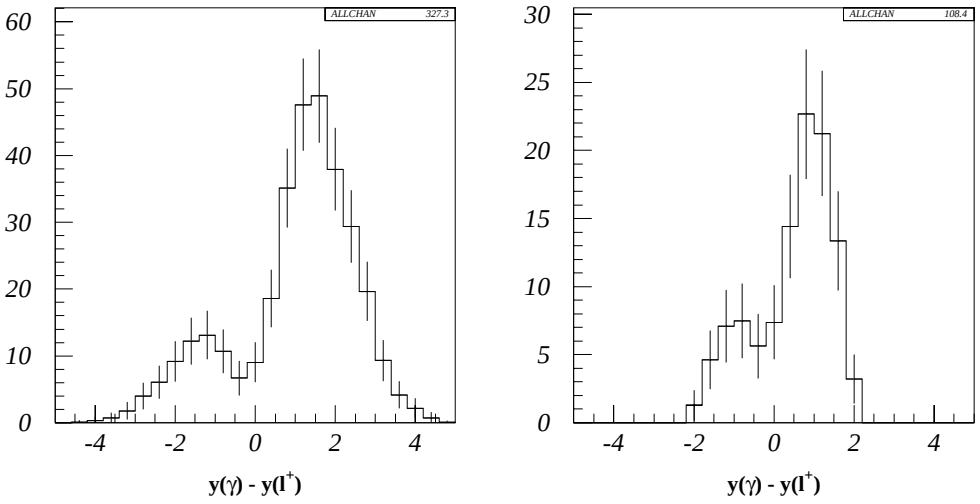

Figure 5: Simulation of lepton-photon rapidity difference observed in a data sample of 1 fb^{-1}. Left plot: central and forward leptons and photons, right plot: central leptons and photons only.

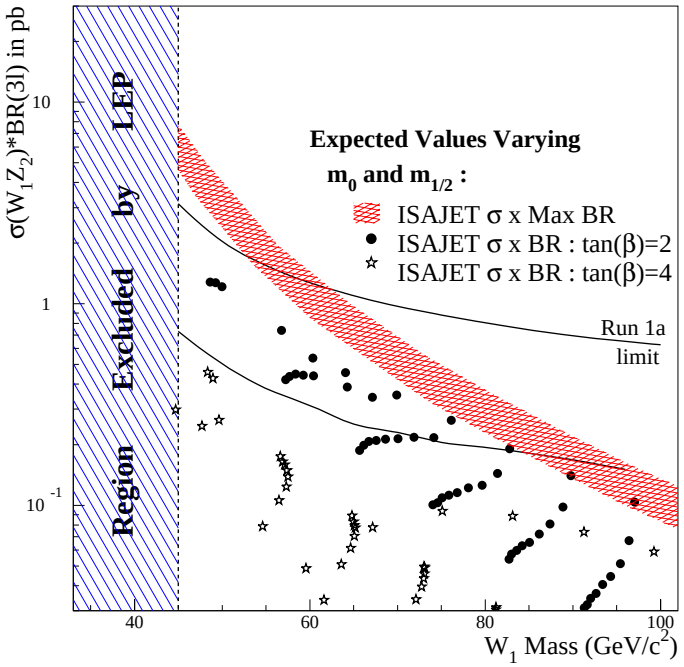

Figure 6: Expected σB as a function of the chargino mass and various choices of SUSY parameters. The upper solid curve shows the limit obtained using the data collected by DØ during Run Ia and the lower curve shows the limit expected for an integrated luminosity of $\approx$100 pb^{-1}. The parameters m_0 and $m_{1/2}$ are the scalar and gaugino masses at the unification scale.

2.5 Search for Chargino-Neutralino Production

Among the most exciting physics topics to be pursued during Run II is the search for SUSY signals. In particular, with the expected large integrated luminosities it should be possible to observe the pair production of charginos and neutralinos for a wide range of SUSY parameters.

Charginos are the SUSY partners of the W and charged Higgs bosons, neutralinos the SUSY partners of the Z boson and the photon. Minimal SUSY models predict chargino masses near the W and Z masses. The lightest chargino ($\widetilde{W}_1$) and second lightest neutralino ($\widetilde{Z}_2$) are expected to have similar masses and are pair produced in $p\overline{p}$ collisions through $q\overline{q}$ annihilation to a virtual W or through squark exchange. Charginos may decay via $\widetilde{W}_1 \rightarrow \ell^{\pm}\nu\widetilde{Z}_1$ and neutralinos via $\widetilde{Z}_2 \rightarrow \ell^{+}\ell^{-}\widetilde{Z}_1$, where $\widetilde{Z}_1$ is the lightest neutralino, which escapes detection. This decay chain results in tri-lepton final states which have very little background. Excluding final states with τ leptons, there are four such channels: eee, μee, $\mu\mu e$, $\mu\mu\mu$, all with equal branching ratios. In Fig. 6 we show the expected cross sections σB for chargino-neutralino production and decay to a tri-lepton channel for various values of SUSY parameters. The predicted values of σB are small, ranging from a maximum of 1 pb at a chargino mass of 45 GeV to a few fb for chargino masses above 100 GeV. The figure also shows the cross section limit obtained

using the data collected by DØ during Run Ia and the limit expected for an integrated luminosity of $\approx$100 pb^{-1}[11].

The largest anticipated background process producing truly isolated leptons is WZ pair production with an expected σB into any particular tri-lepton channel of order 1 fb. Other sources of backgrounds are heavy flavor production and Drell-Yan or Z plus jets production where a jet is misidentified as an electron. The suppression of these backgrounds requires very good lepton isolation and identification.

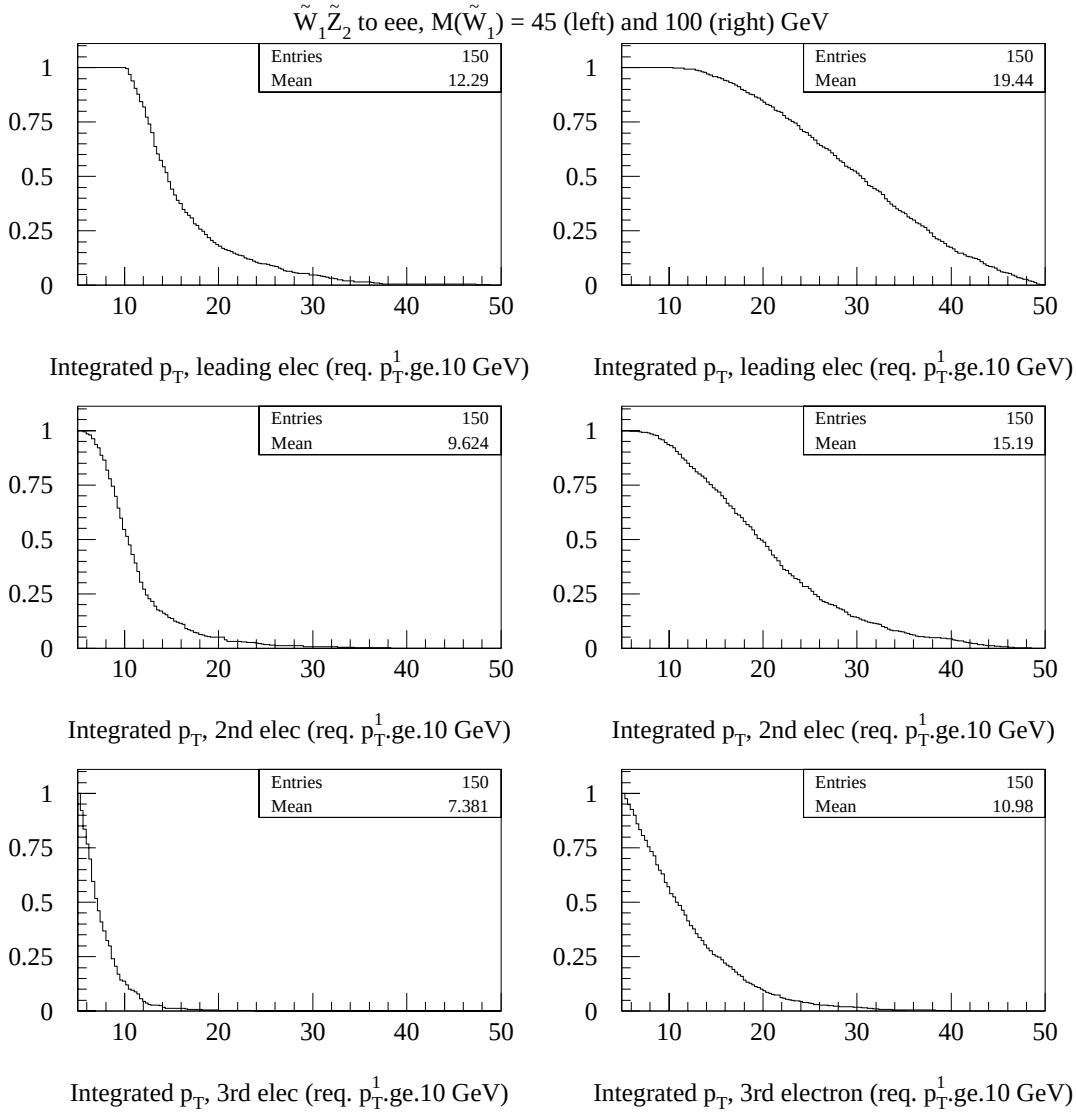

Figure 7: Acceptances as a function of lepton p_T threshold in tri-lepton decays for chargino masses of 45 and 100 GeV. Leptons are ordered in p_T.

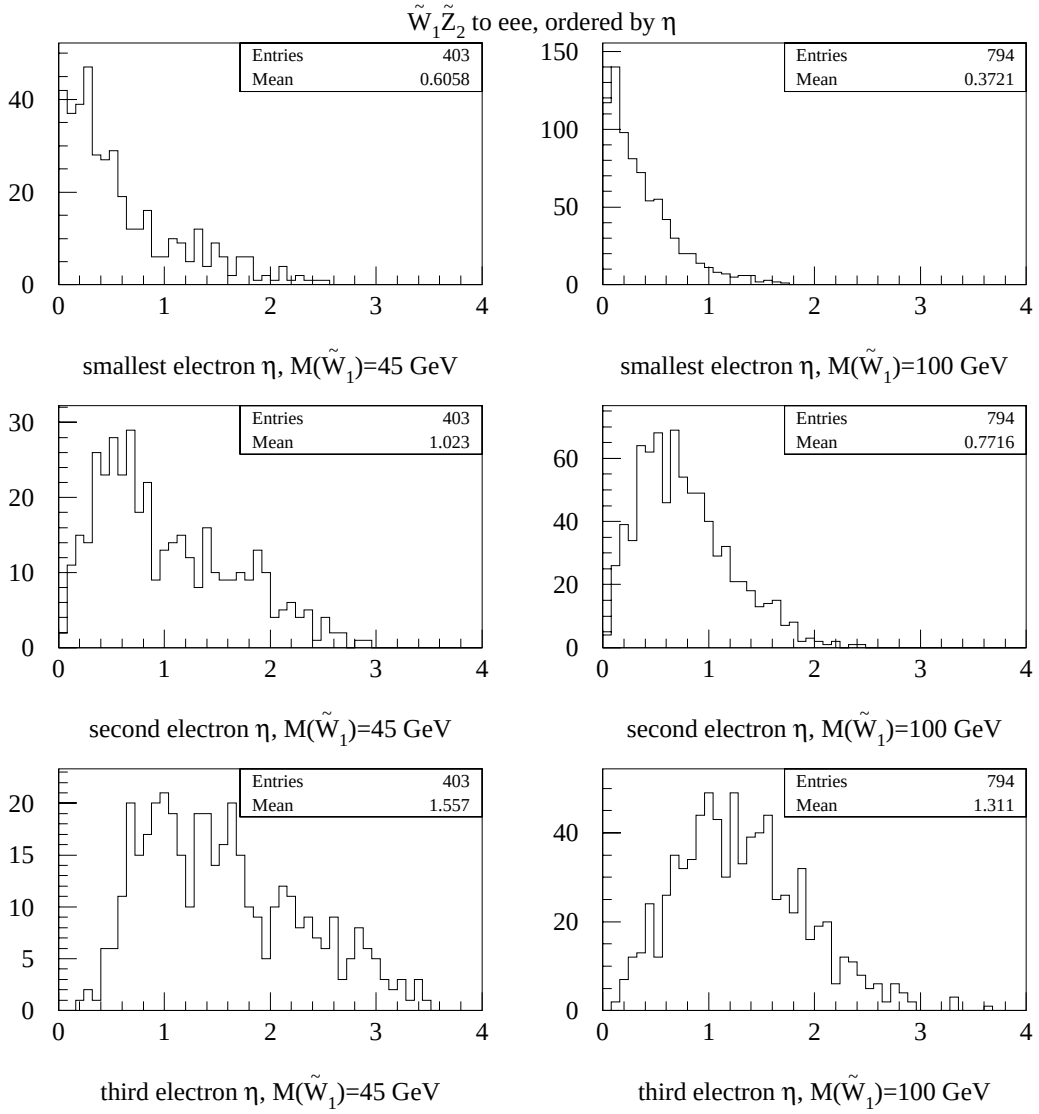

Figure 8: η distributions for leptons in tri-lepton decays for chargino masses of 45 and 100 GeV. Leptons are ordered in η.

Given the small cross sections, it is critical to have large geometric acceptances to be sensitive to the range of SUSY parameters shown in Fig. 6. In Fig. 7 we show the acceptance as a function of p_T threshold for each of the leptons (ordered in p_T) and in Fig. 8 the η distribution of the leptons ordered in η. Between 30% and 40% of the events have at least one lepton with $|\eta| > 1.4$ (the region covered by the Forward Preshower Detector) while between 90% (45 GeV mass) and 50% (100 GeV mass) of the events have at least one lepton with $p_T < 10$ GeV. It is obvious from these figures that, in order to achieve high acceptances, one needs to trigger on and reconstruct leptons down to relatively low p_T (5 GeV or less) and up to high η ($|\eta| > 2.0$).

3 Forward Preshower Detector

3.1 Introduction

The Forward Preshower Detector (FPS) will enhance the capabilities of the upgraded DØ detector to trigger on electrons in the forward region ($1.4 < |\eta| < 2.6$). It will also improve the offline identification of electrons and photons. In the previous section we have shown why we need to accept electrons in the forward region. In the following we will demonstrate that without the FPS, we cannot trigger on these electrons without incurring trigger prescales for many important physics topics. We will show that the proposed FPS will give us the required additional rate reduction. Finally we will present a conceptual design of the FPS and a cost estimate.

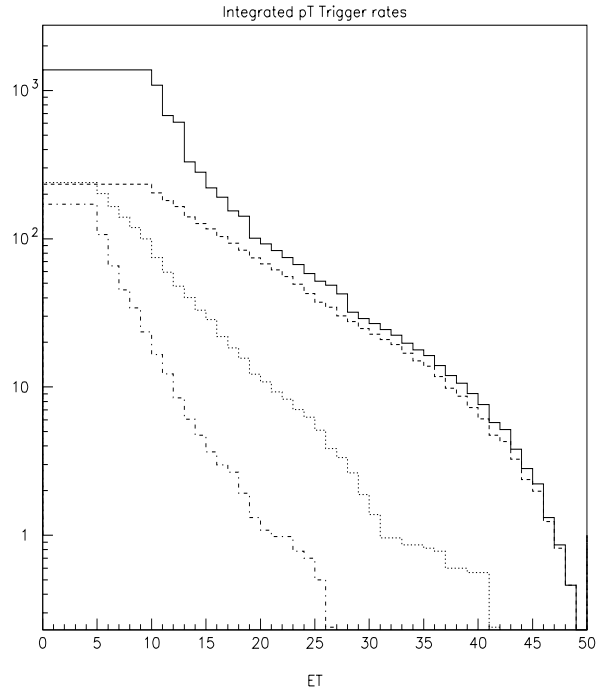

Figure 9: Trigger rates as a function of calorimeter EM tower E_T threshold at $2 \times 10^{32}\text{cm}^{-2}\text{sec}^{-1}$ luminosity. The solid histogram is for a single tower. The dashed histogram is the rate after adding the requirement of a second EM tower with $E_T > 5$ GeV. The dotted histogram is the rate as a function of the E_T threshold of the second tower. Finally the dot-dashed histogram gives the rate as a function of the E_T threshold for 3 towers.

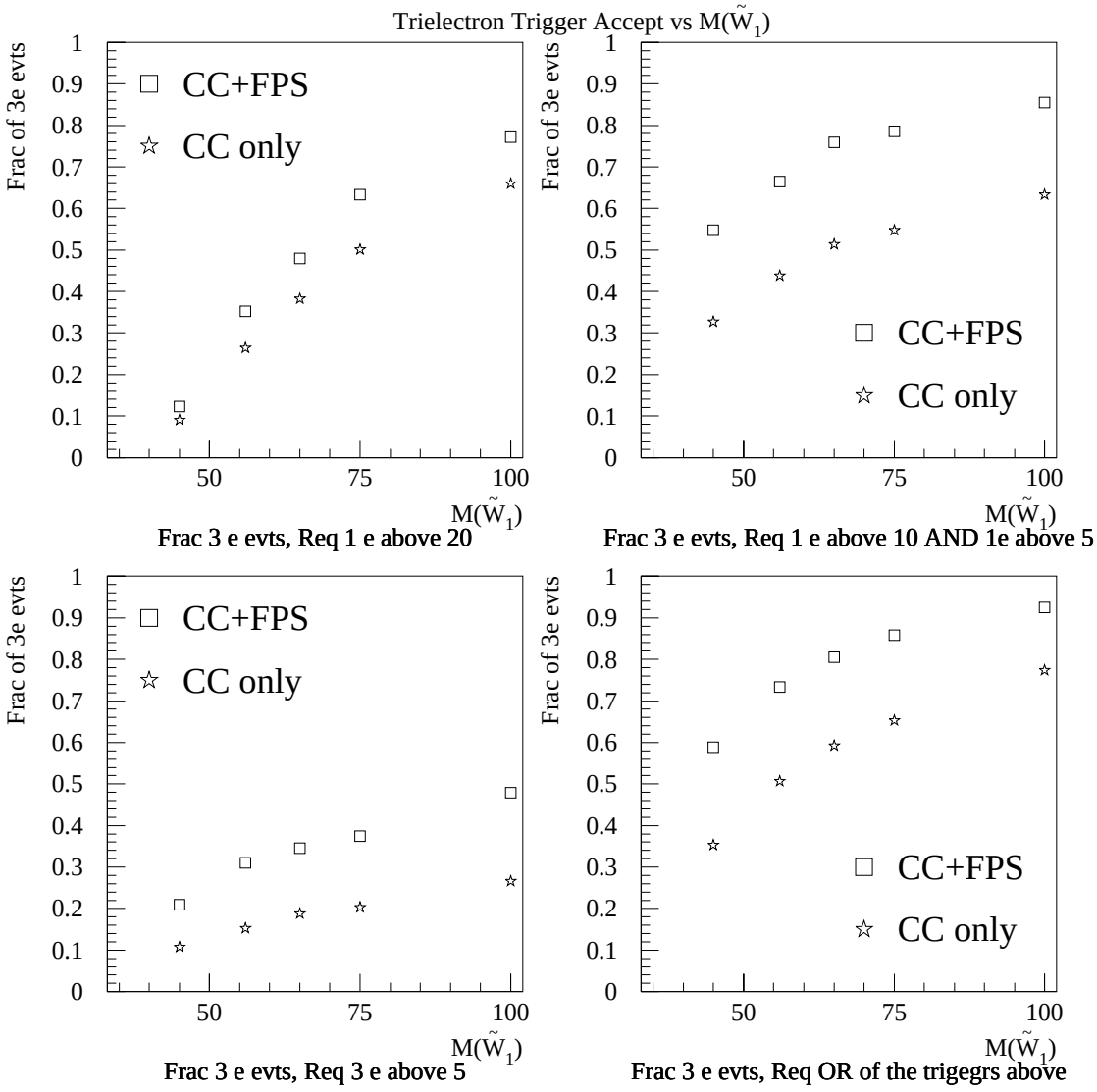

Figure 10: Acceptances as a function of chargino mass in a the eee channel for 3 sets of triggers: a) Single electron with $p_T > 20$ GeV, b) Two electrons, $p_T > 10$ GeV and $p_T > 5$ GeV c) Three electrons with $p_T > 5$ GeV, d) logical "OR" of all 3 triggers.

3.2 Trigger Rates

Based on our experience from Run I, we can estimate the trigger rates for some important physics topics in Run II. We have seen that in order to keep acceptances high we will need to trigger on electrons down to relatively low thresholds, in both central and forward calorimeters. In Fig. 9 we show expected rates at a luminosity of $2 \times 10^{32}\text{cm}^{-2}\text{sec}^{-1}$ as a function of E_T threshold in an electromagnetic trigger tower ($\Delta\eta \times \Delta\phi = 0.2 \times 0.2$) for various trigger conditions. The highest rate is for single electrons. We can see that the rates go up rapidly for $E_T < 20$ GeV, reaching 1.2 kHz at 10 GeV (the central and forward calorimeters contribute roughly equally to the rate). A single electron trigger such as this would be used for $W \to e\nu$. The rate at 10 GeV can be reduced by a factor of 5 by requiring a second EM tower with $E_T > 5$ GeV, as would be used for $Z \to ee$. For chargino/neutralino triggers, somewhat lower rates can be obtained by requiring 3 EM towers with $E_T > 5$ GeV. We note that once a second EM tower is required the rates are not reduced rapidly by raising the E_T of the leading tower. Combining a single EM tower trigger of $E_T > 20$ GeV, a two EM tower trigger ($E_T > 10$ GeV and $E_T > 5$ GeV) and a three EM tower trigger (all with $E_T > 5$ GeV) we can achieve high trigger acceptances over the whole mass range of chargino/neutralino from 45 to 100 GeV (see figure 10) in the 3 electron channel with a combined Level 1 rate of 300 Hz.

Table 1 lists a few specific Level 1 trigger conditions, their cross sections measured in Run I and the trigger rates scaled up to a luminosity of $2 \times 10^{32}\text{cm}^{-2}\text{s}^{-1}$. Level 1 trigger conditions are either on the transverse energy deposited in a trigger tower in the EM calorimeter (e) or the EM+hadronic calorimeter (j).

process	Level 1 trigger	cross section	rate (2×10^{32})
$W \to e\nu$	$e > 10$ GeV	2.4 μb	480 Hz
$Z \to ee$	$2e > 7$ GeV	1.0 μb	200 Hz
$t\bar{t} \to e + jets$	$e > 12$ GeV and $j > 5$ GeV	2.0 μb	400 Hz
$\widetilde{W}_1\widetilde{Z}_2 \to eee$	$e > 20$ GeV or ($e > 10$ GeV and $e > 5$ GeV) or $3e > 5$ GeV		300 Hz (MC)

Table 1: A few Level 1 trigger conditions and measured cross sections from Run I, together with the expected rate at $2 \times 10^{32}\,\text{cm}^{-2}\text{s}^{-1}$.

Obviously these are only a small subset of the physics topics that we would like to study in Run II. Their cumulative rate is 1.4 kHz, which might

be accommodated in our anticipated Level 1 acceptance rate of 5–10 kHz, but it is incompatible with the rate at which events may be accepted by Level 3 (800 Hz). Substantial rate reduction is required in Level 2, which in the central region is afforded by inclusion of the Central Fiber Tracker (CFT) and the Central Preshower Detector in the trigger decision. In the forward region the calorimeter alone can provide only the same trigger capability as in Run I. Since there will be no dedicated forward tracking system an additional device is required in this region to reduce the electron trigger rate. A factor of approximately 3–5 in rejection is required and this establishes the benchmark specification for the Forward Preshower detector.

3.3 Conceptual Design

We propose to build Forward Preshower Detectors (FPS) to augment the electron trigger capabilities of the end calorimeters. One FPS will be located in front of each end calorimeter (EC) and cover the region $1.4 < |\eta| < 2.6$. They will consist of lead converters, 2 X_0 thick, sandwiched between finely segmented charged particle detectors. The detector before the lead converter will register the position of charged particles from the interaction. Photons and electrons shower in the converter and the charged particles in the shower will be detected behind the converter. Heavier charged particles like hadrons or muons will traverse the converter without showering most of the time.

We can therefore identify electrons in the FPS by requiring a large energy deposit in the detector behind the converter and a spatially matched hit in the detector before the converter. We reject photons from π^0 decays because they are not detected before the lead and charged hadrons because they do not deposit as much energy behind the lead. The dominant backgrounds for the electron signature are photons (from π^0 decays) that converted before the FPS and hadrons that either interacted in the converter, creating a shower of secondaries, or that overlap spatially with a photon.

The charged particle detectors must thus have the following properties: a minimum ionizing signal must be well separated from pedestal in the detector in front of the converter. The detector behind the converter must provide a pulse height measurement. Both must have good spatial resolution. The signals from the detectors should be available quickly enough to be used in a Level 1 trigger. In addition, there should be as little material in front of the FPS as possible to minimize the probability of photon conversions, and the thickness of the converter in nuclear interaction lengths should be as small as possible to minimize the probability for hadrons to shower.

Tracks that originate from the center of the detector traverse the beam

pipe, the silicon vertex detector (SVX), and (sometimes) the CFT before reaching the FPS. Tracks with $|\eta| \lesssim 1.6$ must also traverse the cryostat and coil of the superconducting magnet. Figure 11 shows the amount of material in the tracking system, including magnet and central preshower detector, in radiation lengths (X_0) and nuclear interaction lengths (λ_0) for tracks at different pseudorapidities η [12]. In the region $1.4 < |\eta| \lesssim 1.6$ tracks have to traverse the magnet before reaching the FPS. The large amount of material in the magnet will serve as a converter and the lead will be reduced in thickness so that the amount of material traversed is 2 X_0, approximately independent of η.

Each FPS will consist of 16 azimuthal wedges. Each wedge will consist of a layer of scintillator segmented in strips that run perpendicular to one radial edge (u layer), another layer of scintillator in which the strips run perpendicular to the other radial edge (v layer), a 2 X_0 thick layer of lead, and another pair of u and v scintillator layers. The last two u and v layers will extend over the region $1.4 < |\eta| < 2.6$ and the first two u and v layers and the lead over $1.6 < |\eta| < 2.6$. We number the scintillator layers from 1 to 4, starting with the layer closest to the interaction point. For the Monte Carlo simulations described in the following section we used a strip width of 5 mm. Figure 12 shows a schematic layout of one wedge in this geometry.

3.4 Monte Carlo Studies

The Forward Preshower Detector was implemented in the `GEANT` Monte Carlo simulation of the DØ detector to study its performance.

3.4.1 Occupancy

We determine the occupancy of the strips from Monte Carlo two-jet events with $10 < p_T < 500$ GeV. Figure 13 shows the probability that a strip in layers 1 or 2 has a signal above pedestal versus the strip index (counting from the outer radius inwards). Figure 14 shows the probability that a strip in layers 3 or 4 has a signal with energy above 5, 10, or 15 MeV. Occupancies before the lead are about 1%, while after the lead they are about 0.1%.

3.4.2 Trigger

We define a simple trigger algorithm for electrons which consists of the following elements:

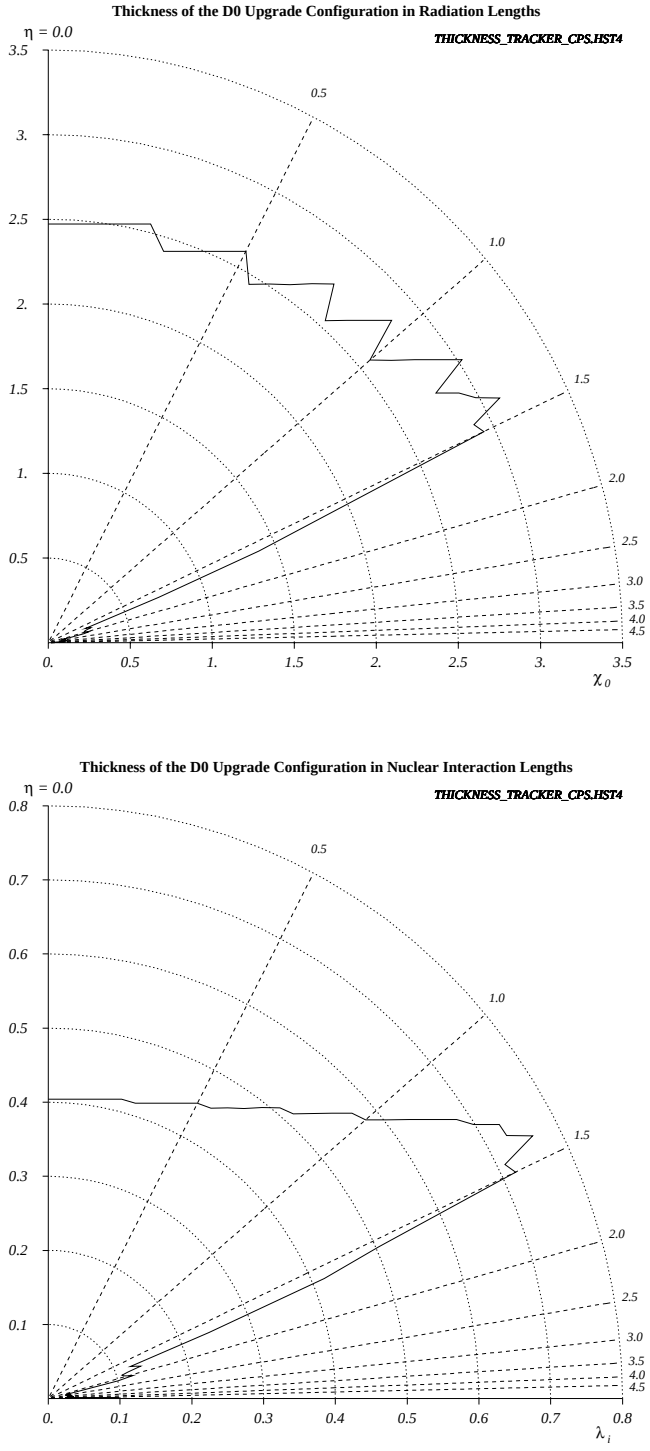

Figure 11: Amount of material traversed before the FPS by tracks originating at the center of the detector in radiation lengths (top) and nuclear interaction lengths (bottom).

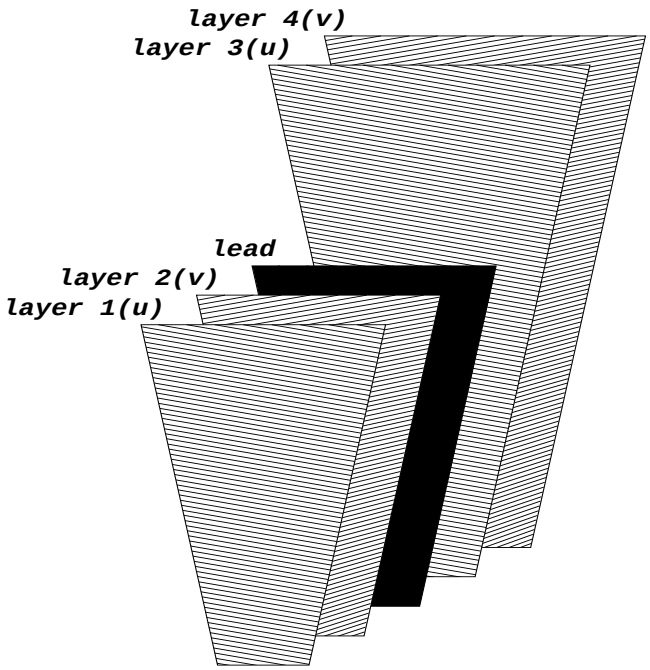

Figure 12: Schematic layout of one azimuthal wedge.

- **energy:** large energy deposits ($\gtrsim$ 14 MeV) in at least one u and v segment in layers 3 and 4 behind the converter and a hit in the corresponding u and v segments in layers 1 and 2 in front of the converter. For $1.4 < |\eta| \lesssim 1.6$, layers 1 and 2 are not present and only energy in layers 3 and 4 is required. This condition must be satisfied for overlapping u and v strips.

- **isolation:** little energy in the two u and v segments on either side of a group of seven segments, centered on the segment that satisfied the energy requirement. The sum of these four segments must be below 15 MeV.

- **calorimeter match:** spatial match of a FPS trigger with an EM trigger tower above a threshold. This match uses a look-up table that maps the u and v coordinates into a set of calorimeter towers. In azimuth the match is typically to one calorimeter tower, except for hits close to tower boundaries. In pseudorapidity the match is to several towers, corresponding to the spread in z vertex positions.

The trigger efficiency depends on the electron energy because the track multiplicity in the preshower increases with the energy of the incident electron. Table 2 lists the efficiency of the trigger algorithm for MC samples of electrons with different p_T values. We also measure the efficiency of this trigger for electrons from $Z \rightarrow ee$ decays. This sample consists of fully simulated $Z \rightarrow ee$ decays. The calorimeter match is 100% efficient for electrons.

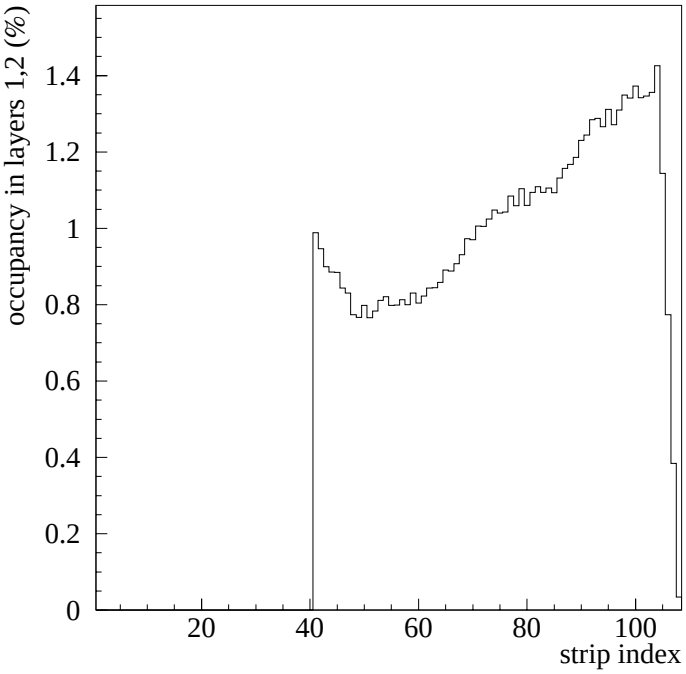

Figure 13: Occupancy of strips in scintillator layers 1 and 2. Strips 1–40 are not present in this layer.

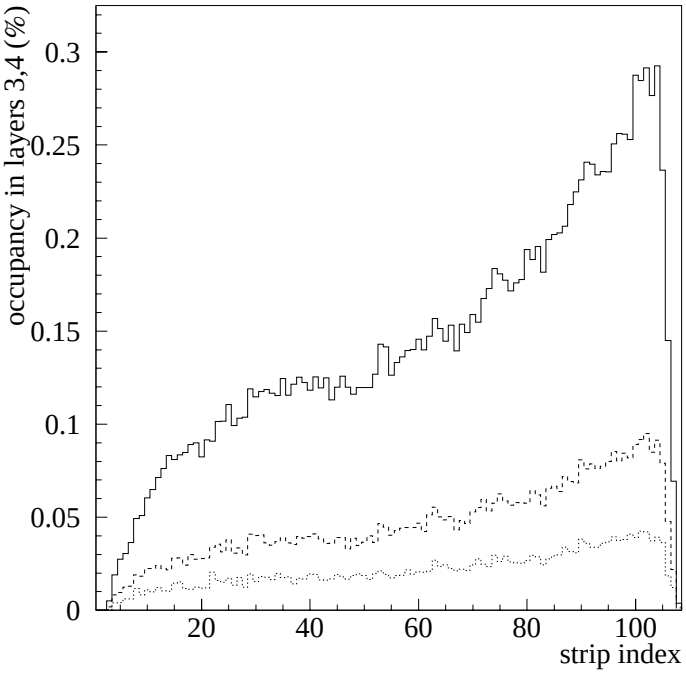

Figure 14: Occupancy of strips in scintillator layers 3 and 4 for signals with energy above 5 (——), 10 (- - -), and 15 MeV (.....).

FPS trigger	Single electrons			electrons from
	$p_T = 5$ GeV	$p_T = 20$ GeV	$p_T = 50$ GeV	$Z \to ee$
energy	0.67±0.02	0.90±0.01	0.95±0.01	0.88±0.02
+ isolation	0.67±0.02	0.90±0.01	0.93±0.01	0.85±0.02

Table 2: Trigger efficiency for different electron samples.

FPS trigger	Location of trigger tower	EM trigger tower thresholds		
		$T = 5$ GeV	$T = 10$ GeV	$T = 15$ GeV
none	anywhere	36 μb	4.3 μb	0.50 μb
none	EC	19 μb	1.3 μb	0.22 μb
rate reduction factors with respect to EC calorimeter rate				
energy	EC	4.0	2.2	1.6
+ isolation	EC	4.2	2.7	1.8
+ isolation	matched to FPS	7.4	3.4	2.8
rate reduction factors for events with 3 additional minbias interactions				
energy	EC	1.7	1.5	1.6
+ isolation	EC	1.8	1.9	1.6
+ isolation	matched to FPS	6.9	2.9	2.0

Table 3: Trigger cross section/rejection factors for different FPS algorithms and EM trigger tower thresholds T.

This condition can only be implemented at Level 2, because no information on the location of the EM trigger towers is available at Level 1.

We determine trigger cross sections from two-jet events which dominate the cross section for inclusive electron triggers. We used the standard two-jet samples generated with `ISAJET/GEANT` in bins of jet p_T. To estimate the effect of multiple interactions we give results for two-jet events containing only one interaction and for events containing an additional three soft interactions. Figure 15 shows the cross section as a function of calorimeter EM tower threshold for different FPS conditions.

The first row in Table 3 lists the Level 1 cross section for an inclusive EM calorimeter trigger (no preshower). In order to give a useful estimate of the reduction in cross section due to various FPS trigger algorithms, we restrict the Level 1 calorimeter trigger to the End Calorimeters (EC's). In order to get the absolute trigger rate for the full acceptance of the detector, the rate for central electron triggers has to be added with corrections for overlaps between the two fiducial regions. The second row lists the Level 1 cross

section for events with an EM trigger tower above threshold in the EC. The next three rows list the *rejection* for EM triggers including FPS information relative to the EC trigger rate without the FPS. Row three requires the FPS energy term and row four the FPS isolation term. At the output of Level 1 the FPS reduces the rate for electron triggers in EC by about a factor 2–4. The fifth row includes the spatial match with the EM trigger tower and the numbers in Table 3 show that at the output of Level 2 the rate is reduced by about a factor 3–7, depending on the calorimeter threshold. The last three rows give the rejections for dijet events with an additional three minbias interactions superimposed. We see that they decrease at Level 1 for low thresholds, while the rejection out of Level 2 is only slightly affected.

These simulations show that the required trigger rejections can indeed be obtained.

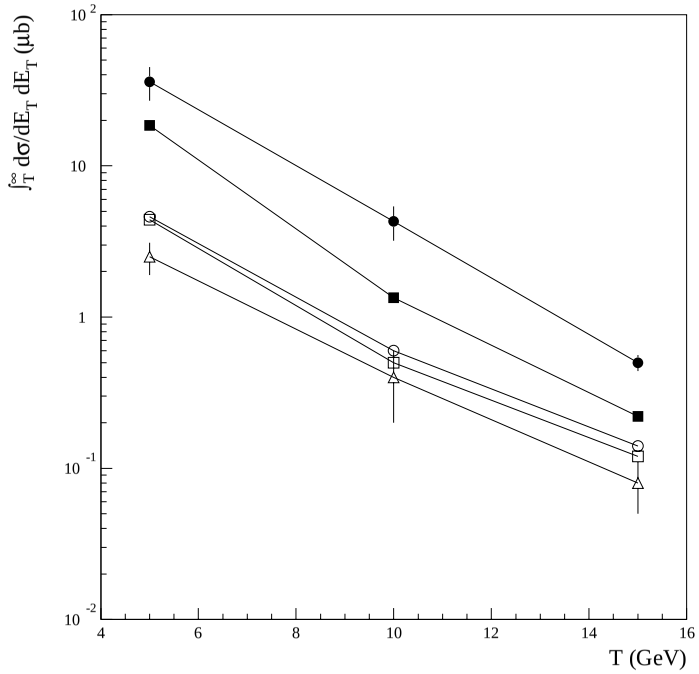

Figure 15: Trigger cross sections versus Level 1 EM trigger tower E_T threshold T. Errors are only shown on the sets of points with the highest and lowest cross sections. The FPS conditions for the five sets of points correspond to the five rows in Table 3 for single interactions.

3.4.3 Segmentation Studies

Since the cost of the detector depends on the number of channels, we have investigated geometries with different channel counts. We can reduce the

channel count by increasing the strip width from 0.5 to 1.5 cm or by eliminating the track stub detector in front of the converter. Increasing the strip width reduces the rejection by 20%, while eliminating the planes before the lead reduces the rejection by 40%. We also studied increasing the segmentation in azimuth to 32 wedges and found that the rejection is improved by only 10%. We conclude that a division into 16 azimuthal wedges and roughly 5 mm wide strips represents a good balance between performance and cost.

3.4.4 Offline Electron ID

After offline event reconstruction, the event vertex and the position of EM showers in the calorimeter will be known with high precision, allowing a much tighter match between calorimeter and FPS than at the trigger level. Both isolated and non-isolated electrons will benefit from this extra information. Reduced background for top, W and supersymmetry signals with isolated electrons will result. We note that in the present Run I detector, the forward electron sample is rather less pure than the central, and that extra background rejection will therefore be welcome. Studies of electron identification and background rejection in W+jets events, using the FPS, are in progress.

To demonstrate the potential for non-isolated electrons, we have performed a study of the improvement in background rejection due to the FPS information, for electrons from b decays. As a signal sample we use $p\overline{p} \rightarrow b\overline{b}$ ISAJET events in which the b quarks were forced to decay to $e\nu c$. As a background sample we use ISAJET dijet events with $2 < E_T^{jet} < 100$ GeV. Both samples were processed through GEANT to simulate the detector response.

We start with energy clusters that are reconstructed in the electromagnetic section of the ECs. We only accept clusters for which the line connecting the shower centroid with the event vertex passes through the FPS detector. We then cut on the energy deposited in the three adjacent FPS segments in each layer that are closest to this line. We require energy deposits consistent with one minimum ionizing particle (mip) or greater in layers 1 and 2, indicating an incident charged track that points to the calorimeter cluster. We require at least 10 MeV ($\approx$ 10 mips) in layers 3 and 4 to ensure that the particle started to shower in the lead absorber.

The efficiency of this simple algorithm is given by the fraction of clusters in the signal sample that are accepted. We use clusters that are due to electrons, as verified using the ISAJET information, to determine the efficiency. The rejection against background clusters is given by the fraction of clusters in the background sample that are rejected by the algorithm. Figure 16 shows the smaller of the layer energies before the lead for the two samples and figure 17 shows the smaller of the two layer energies after the lead. The

algorithm rejects 99% of all background clusters, while accepting 70% of the electron clusters.

These results are preliminary. Without a more complete investigation of signal and background rates, one cannot conclude that useful b-tagging in the electron mode will be possible. This study should be taken as an illustration of the potential improvements in offline electron identification that the FPS will provide.

3.4.5 Photon/π^0 Separation

The fine segmentation of the FPS makes it useful for distinguishing photons from neutral pions. Neutral pions copiously produced in QCD processes are the main source of background for both photons and electrons. Even at moderate π^0 energies the two photons from the $\pi^0 \rightarrow \gamma\gamma$ decay are usually spatially close to each other so that the EM calorimeter can not resolve the two EM showers from these photons. When identifying electrons, requiring a single charged track pointing toward the EM cluster with an E/p match eliminates most of the $\pi^0 \rightarrow \gamma\gamma$ decays. For final states involving a photon this is no longer possible. One needs an EM shower detector with fine position resolution in order to permit π^0/photon separation. The FPS is such a detector.

The typical spatial separation of photons from π^0 decay in the FPS detector as a function of the π^0 rapidity is shown in figure 18 for three π^0 transverse energies: 10, 20, and 50 GeV. Since the preshower spatial resolution is limited by the 5mm strip-width, it is clear from this figure that π^0/photon separation is only possible at low transverse energies ($\lesssim 50$ GeV). However, since QCD production drops rapidly with jet transverse energy, this is exactly the energy range where the QCD background dominates.

One of the ways to distinguish between π^0s and photons in the FPS is to measure the root-mean-square width (*RMS*) of the shower energy profile in the last two layers of the preshower detector. The *RMS* distributions for photons and π^0s with transverse energy of 10 GeV are shown in figure 19 with solid and dashed lines, respectively. Both distributions can be well fitted with a Gaussian curve, and there is a significant difference in the mean of the two Gaussians.

The difference in the *RMS* distributions for π^0s and photons can be used either for a statistical π^0/γ-separation or to reduce the π^0 background by cutting on the *RMS* value. The rejection versus efficiency for the latter method is shown in figure 20 for three π^0/photon transverse energies: 10, 20, and 50 GeV. As one would expect, the rejection power of this method is lost

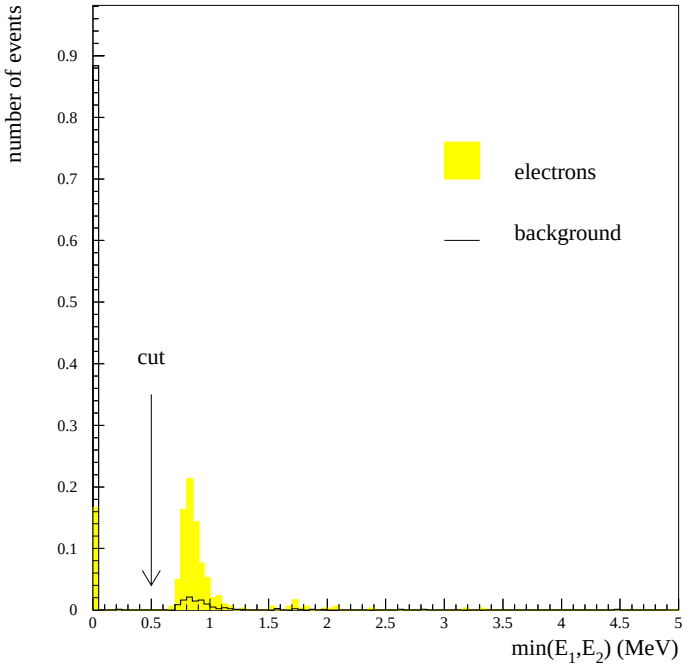

Figure 16: Minimum of energies in layers 1 and 2 for electrons and background clusters.

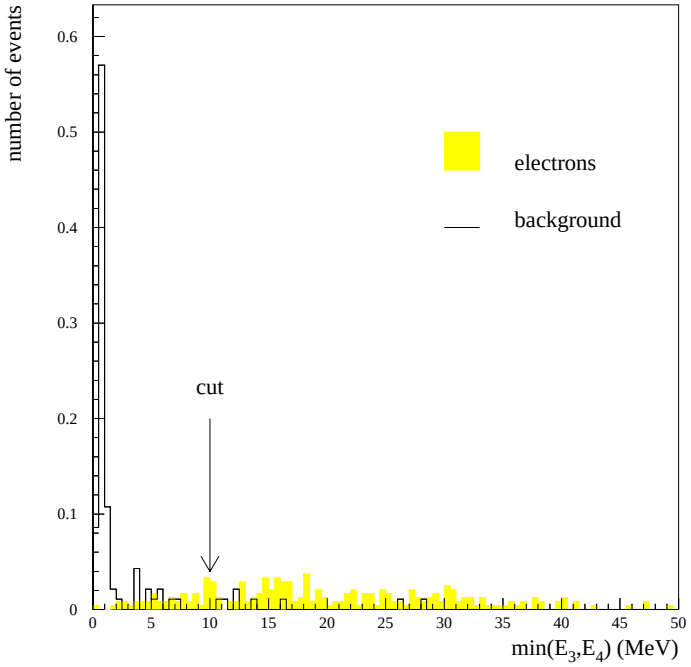

Figure 17: Minimum of energies in layers 3 and 4 for electrons and background clusters.

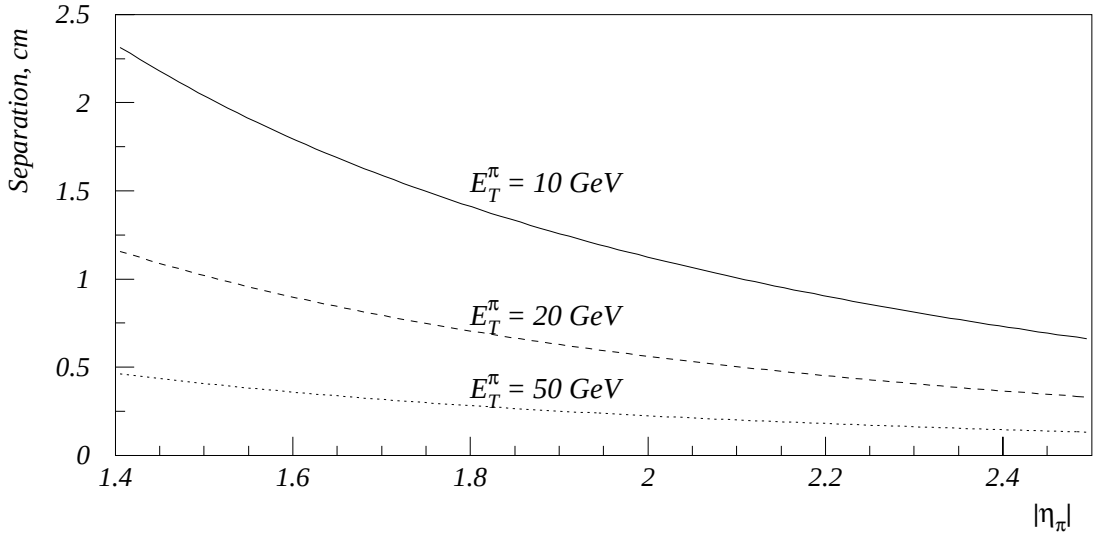

Figure 18: Separation of the photons in $\pi^0 \to \gamma\gamma$ symmetric decay for fixed transverse energy of the π^0 (E_T^π) as a function of the π^0 pseudorapidity. Solid, dashed and dotted lines correspond to $E_T^\pi = 10,\ 20$ and 50 GeV, respectively.

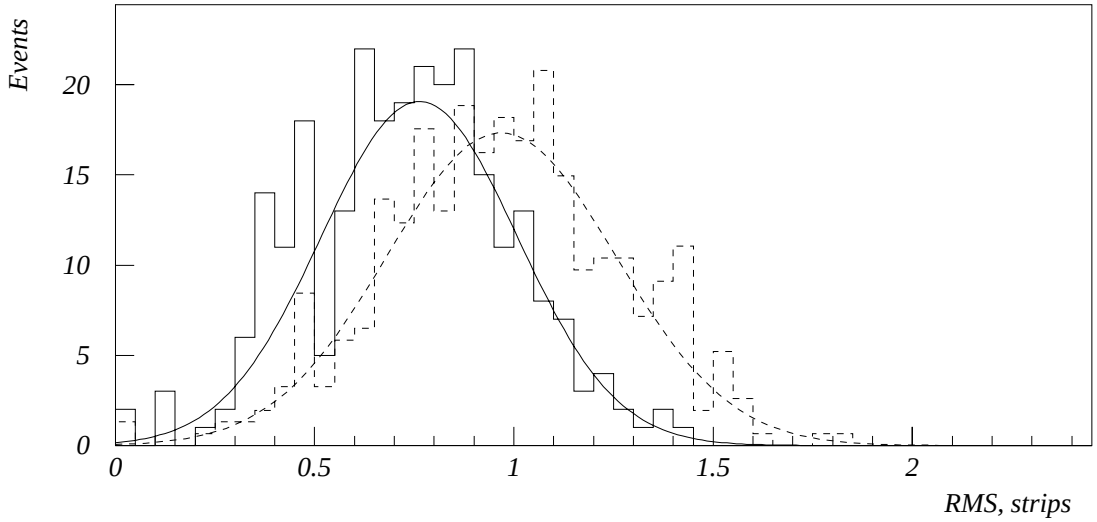

Figure 19: *RMS* distributions for the photons (solid histogram) and π^0s (dashed histogram) with transverse energy of 10 GeV. Solid and dashed lines show the fits to Gaussian curves.

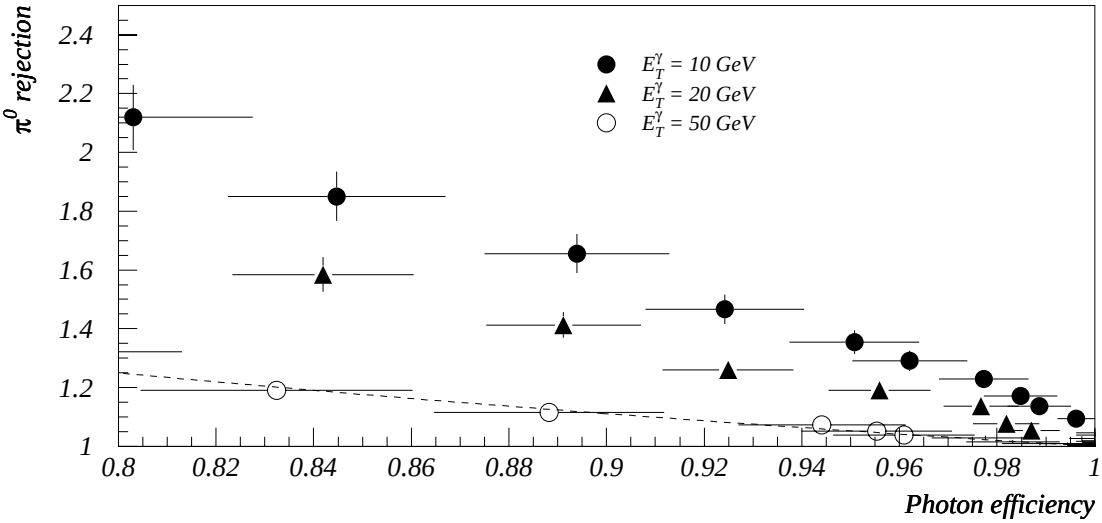

Figure 20: Rejection for π^0s versus efficiency for photons based on the *RMS* cut for three π^0/photon transverse energies: 10 GeV (solid circles), 20 GeV (solid triangles), and 50 GeV (open circles). Above the dashed curve additional rejection for π^0s comparing to the photons can be gained. There is no additional rejection against the π^0s for transverse energy $\gtrsim$ 50 GeV.

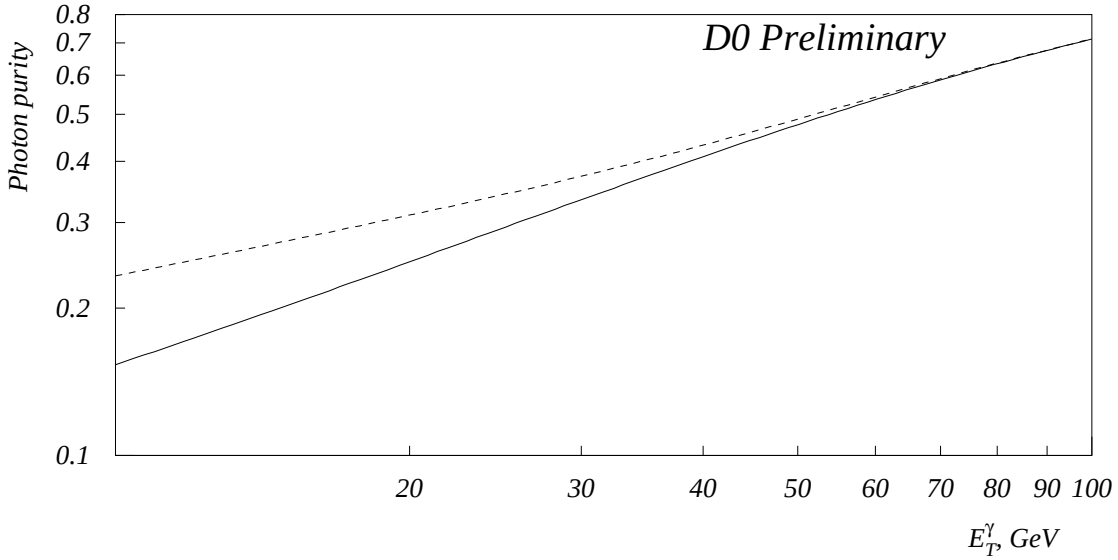

Figure 21: Purity of the forward photon sample collected with the DØ detector in 1992–1993 (solid line, DØ preliminary). The dashed line shows the improvement in the purity after using an *RMS* cut which is 90% efficient for photons.

for π^0 transverse energies $\gtrsim$ 50 GeV, but at lower transverse energies, one can achieve a rejection factor of $1.5 - 2$ against π^0's with 90% efficiency for photons.

A possible use of the additional π^0 rejection is the direct photon analysis, where the purity of the photon sample rapidly deteriorates for lower photon transverse energies. Figure 21 shows the purity of the forward photons in the direct photon candidate sample as a function of their transverse energy for 1992–1993 DØ data (solid line)[13]. Since the number of minimum bias interactions per crossing will be much higher for the upgraded Tevatron, the photon purity in run II will be even worse than the one shown in this figure. Using the *RMS* cut which is 90% efficient for photons, one can significantly improve the photon purity at the lower end of the spectrum, as is shown with a dashed line in the same plot.

Another physics analysis which can gain from additional π^0 rejection is $W\gamma$, $Z\gamma$ production. The sensitivity to non-standard tri-boson couplings is affected by uncertainties in the QCD background (the main source of background in these processes), so an additional suppression of this background helps to increase the sensitivity.

3.5 Detector Design

In this section we describe our preliminary design of the detector, including a scheme for signal routing and detector assembly. We also present a brief discussion of the radiation dose that can be expected in the forward region during Run II.

3.5.1 Technology

We have opted to pursue the same technology for the FPS as used for the central preshower (CPS) [14]: triangular scintillator strips with embedded wavelength-shifting (WLS) fibers, read out by visible light photon counters (VLPCs). This saves the cost and time involved in the R&D that would be necessary to develop a different technology. We will be able to use identical front-end and trigger electronics for both detectors. The many design considerations common to the two detectors, such as light yield requirements, scintillator properties and fabrication, and detector assembly techniques, will allow us to benefit from the considerable amount of research and development that has gone into the design of the CPS. We expect to base many components of the design of the FPS, such as connector design, detector calibration and temperature monitoring, fiber bundling, and scintillator extrusion

on CPS R&D, introducing appropriate modifications, and additions or deletions, as they are warranted. We refer the reader to [14, 15, 16, 17, 18, 19], and references therein, for more details on the CPS design and readout, specifics of the VLPCs, and other related details.

Tight spatial constraints apply to the construction of the FPS, because signal cables, cooling fixtures, and other attendant support hardware that service the inner tracking detectors have to be routed through the region defined by the magnet/cryostat boundaries to the outside of the detector (see Fig. 22). The intrinsic compactness of a lead/scintillator detector, coupled with the ease with which it can be made to conform to the shape of the EC cryostat heads, allows the construction of the detector in the available space.

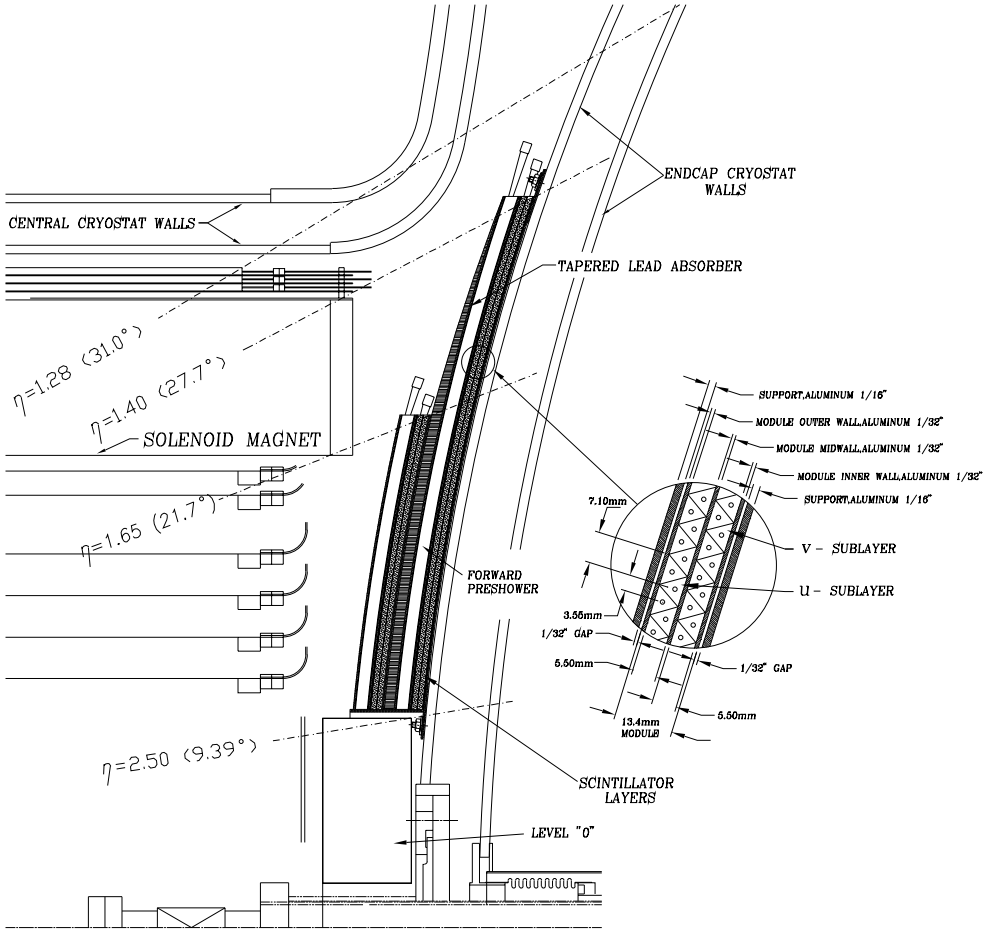

Figure 22: One-quarter view (in r-z) of the FPS, with detail of a scintillator u-v layer.

As in the CPS, each scintillator layer will consist of two nested layers of triangular-shaped scintillator strips. This design eliminates dead regions re-

sulting from projective cracks and has been shown to give position resolution substantially better than the inter-strip separation when light-sharing information between adjacent strips is incorporated into the analysis: a position resolution of $\approx$0.6 mm has been achieved with cosmic ray muons using strips with a base length of 9 mm and a height of 4.5 mm [14].

The strip dimensions are driven primarily by the expected occupancies, the desired position resolution, the light yield required, and detector cost. The strip dimensions shown in figure 22 are those currently proposed for the CPS: a strip width of $\approx$ 8.1 mm and a strip height of $\approx$ 5.5 mm.

3.5.2 Detector Segmentation and Signal Routing

The detector will be composed of four structurally distinct layers, with each layer consisting of eight wedges or modules (see figure 23). Each module will subtend 45° (one octant) in ϕ, and will consist of both a u and a v scintillator sublayer. The active region of each sublayer will subtend the central 22.5° of a module, plus an additional 12.8 mm on either side to provide an overlap region of coverage between layers, in order to eliminate projective cracks. The logical segmentation of the detector into two distinct regions in pseudorapidity (defined by the presence or absence of the magnet coil) dictates that the modules will be of two different sizes. The two inner (outer) layers are composed of small (large) modules, with the inner layer situated closer to the nominal interaction point (see figure 24). The module positions in successive layers will be staggered by 22.5° in order to cover the full azimuthal angle.

The scintillator strips will be oriented perpendicular to the radial edge of the active volume of a module. The central hole in each triangular scintillator strip shown in the inset of Fig. 22 accommodates a WLS fiber, which is routed to the edge of the module. The fibers then run radially to the perimeter of the module. The outer $\approx$ 11° on either side of each module provide space and mechanical support for routing the WLS fibers to the outer radius. Space restrictions prohibit the mounting of connectors anywhere but at the periphery of the detector.

Connectors that couple the WLS fibers on the detector end to clear transmission fibers are mounted at the end of each fiber-routing channel. The clear fiber is then brought around the circumference of the FPS and down to the platform below the detector, where the VLPCs will be housed. The precise mapping of FPS strips into VLPC channels has yet to be determined.

Based on our studies, we anticipate that a strip width of $\approx$ 8.1 mm and a strip height of $\approx$ 5.5 mm will provide the required performance, while not

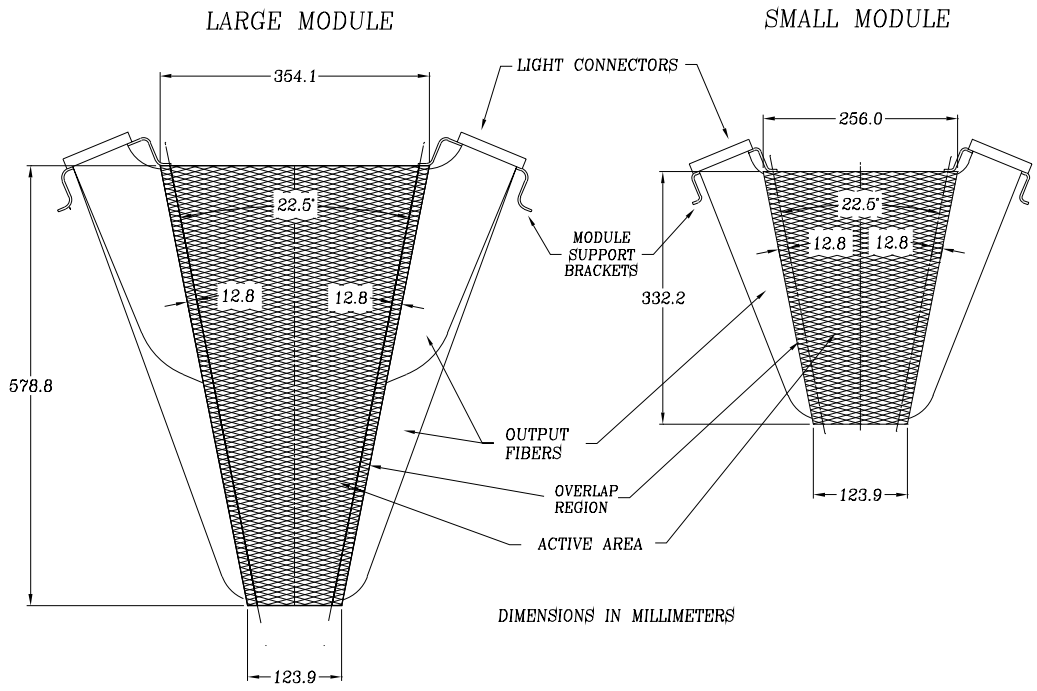

Figure 23: Representative large (left) and small (right) detector modules for the FPS. The active scintillator volume is contained in the central cross-hatched region. The outer pathways are for routing the emerging WLS fibers, with the fibers from the u and v sublayers routed in separate pathways.

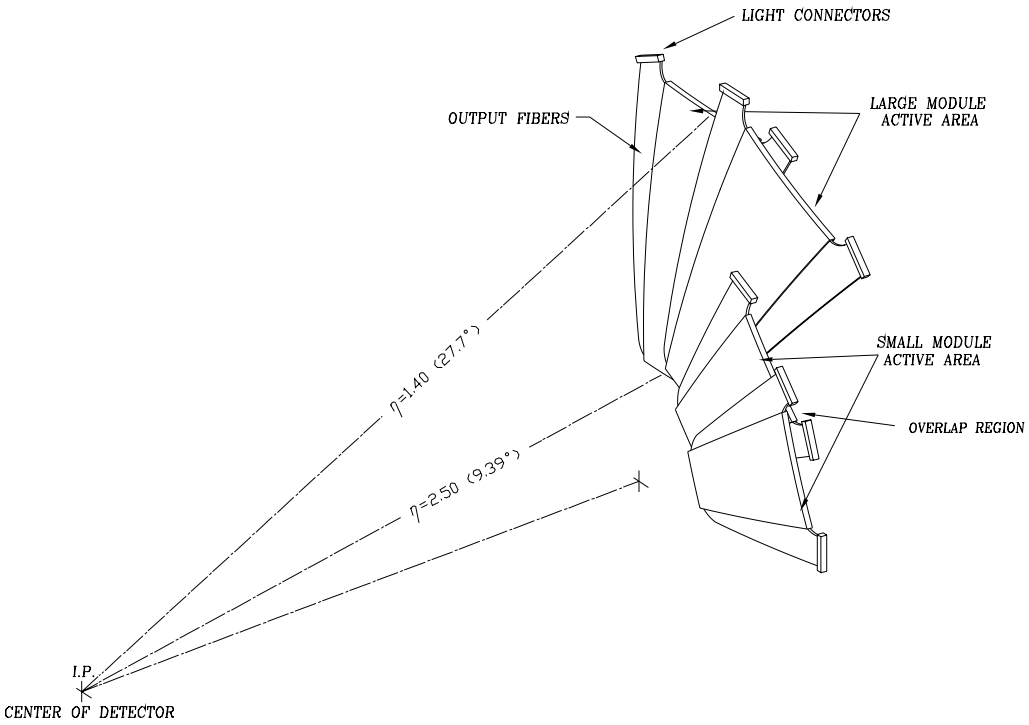

Figure 24: Three-dimensional view of the position of the modules in the four layers of the FPS, showing the 22.5° staggering from layer to layer, and the overlap region.

exceeding the available number of VLPC cassettes. Given these dimensions, a small (large) module will contain 95 (155) strips in each u or v layer. The total channel count for the detector is then (95 + 155) strips $\times$ 2 sublayers (u and v) per module $\times$ 8 modules per layer $\times$ 2 detector layers for each module type $\times$ 2 sides = 16,000 channels.

The lead will consist of two radiation lengths in the region $1.6 \lesssim |\eta| < 2.6$ and will be tapered in the region $1.4 < |\eta| \lesssim 1.6$ in order to equalize the amount of material traversed as a function of pseudorapidity.

3.5.3 Module and Detector Assembly

The strips in the u and v sublayers in each module will be individually wrapped with mylar for optical isolation, and epoxied to 1/32 inch thick aluminum backing sheets. The module will be covered with another aluminum sheet, creating a sandwich of aluminum support and scintillator. The light connectors at the periphery of the module will be supported by aluminum brackets at the edge of the module. The brackets, connected to the outer edge of the module on one end and one of the support ribs on the other, are designed to both strain-relieve the fiber/connector interface, and to hold the module in place.

The structure of the assembled detector is schematically illustrated in Fig. 25. The structural support for each layer consists of 1/16 inch thick aluminum sheets that have been appropriately shaped to allow the final detector to conform to the head of the end calorimeter cryostat. (The bending radius for each layer will appropriately compensate for the incremental difference in radius from layer to layer due to the nested structure.) Eight radial support ribs, which help align and support the modules and the sublayer, will be fastened at equal angular intervals on the aluminum sheet. After the supporting layers (aluminum sheet plus ribs) are constructed, they will be successively mounted to one another until the entire supporting unit of the detector is assembled. The modules, which have been independently constructed and tested, will be inserted into the support structure and re-tested. The fully constructed detector will be mounted to the end cryostat at both its inner and outer radii via aluminum extensions to the support ribs on the outermost FPS layer. The extensions will be bolted to stainless steel mounting brackets welded to the outer cryostat shell.

The modular structure of the FPS detector will allow installation to be performed sectionally by mounting successive modules in place on the EC cryostat head. Alternatively, should installation logistics favor preassembly, the north and south FPS systems could be assembled in their entirety and installed on the EC as a monolith.

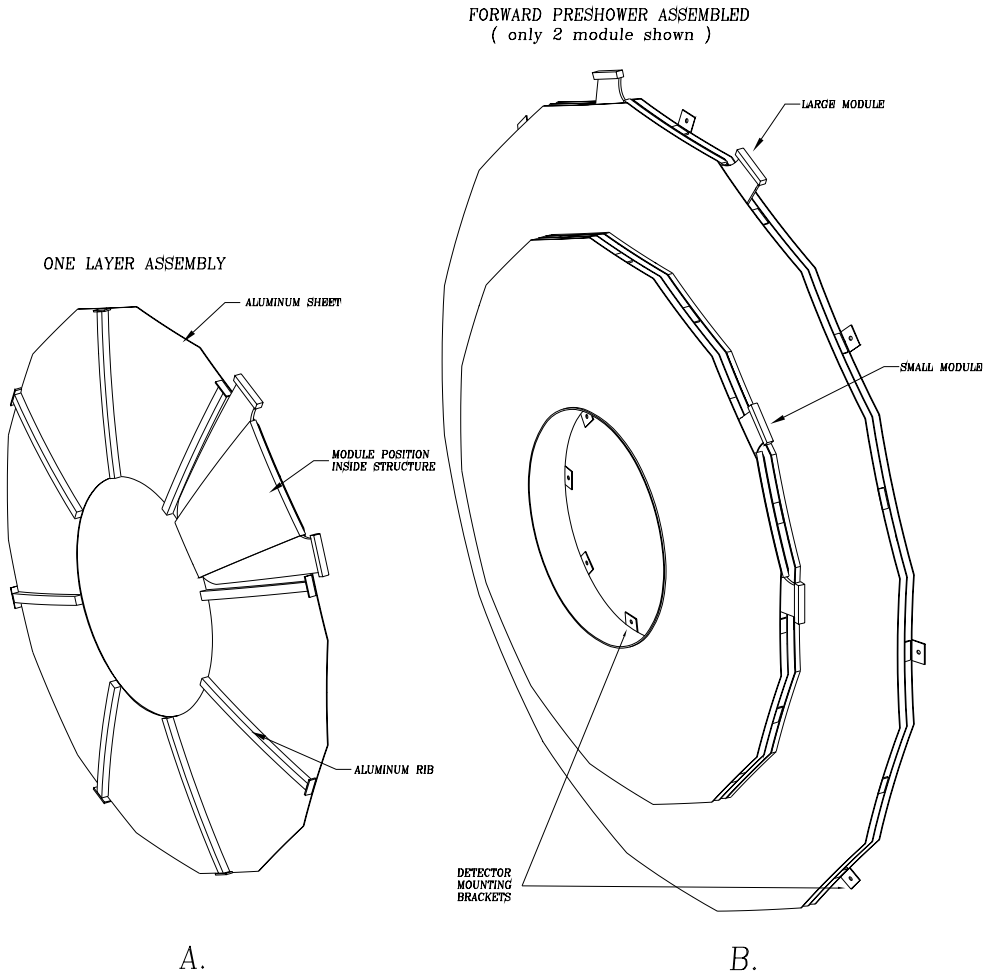

Figure 25: (A) One FPS layer, showing the structural aluminum sheet, eight support ribs, and a module inserted. (B) The fully constructed detector, showing the four concentric nested layers (two inner small layers, and two outer large ones), and the mounting extensions on the two ends of the support ribs of the outermost layer.

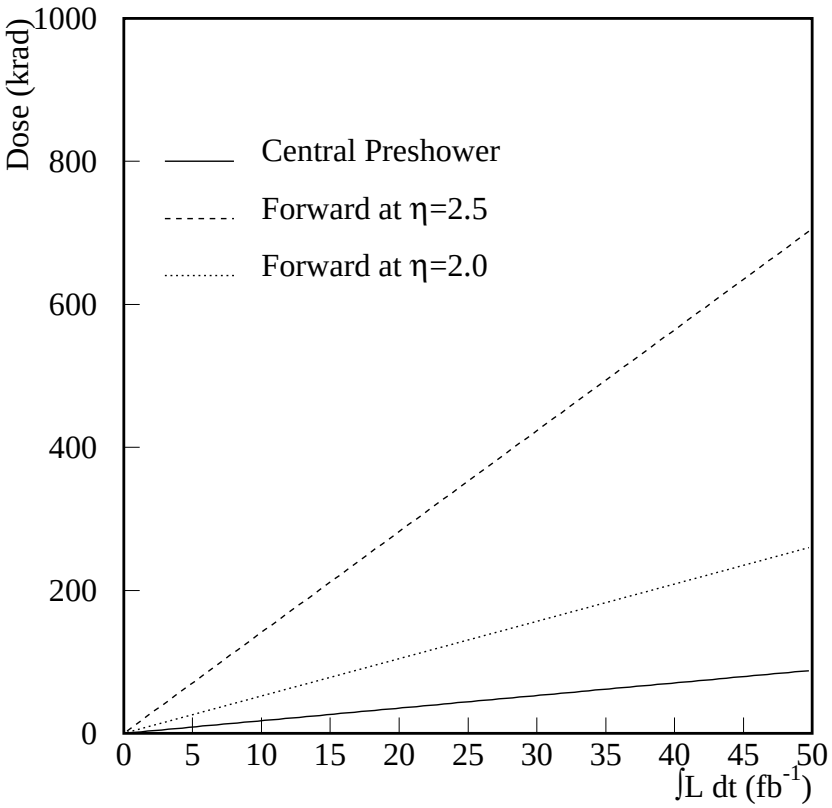

Figure 26: The estimated total radiation dose in the CPS, and at $\eta = 2.0$ and $\eta = 2.5$ in the FPS, as a function of the integrated luminosity.

3.5.4 Radiation Dose

The potential for radiation damage of scintillator/fiber detectors, particularly at high luminosities, is an obvious concern at forward pseudorapidities. A detailed calculation has been done in order to estimate the expected dose rate in the Run II environment [20]. The calculation incorporates both the charged and neutral hadron fluxes from minimum bias events, and the effect of albedo neutrons from the calorimeter surface. The minimum bias cross section is assumed to be 50 mb, with each minimum bias interaction producing four charged particles per unit of pseudorapidity. Assuming the neutral hadron flux to be half of that for charged particles, and including effects resulting from looping of low-p_T tracks, the expected dose rate at a luminosity of $\mathcal{L}$=10^{32}cm^{-2}sec^{-1} is given by:

$$\frac{dD}{dt} = 2.2 \times 10^{-5} \text{ rad/s} + \frac{0.8}{(r_\perp/1 \text{ cm})^2} \text{ rad/s}, \qquad (1)$$

where $r_\perp$ is the perpendicular distance from the beamline to the region where the dose is being calculated. The first term on the right is the contribution due to albedo neutrons; the second term is that due to minimum bias interactions.

In the course of extensive studies of radiation resistance of the scintillator and fibers carried out by the CPS group, it was found that a dose of 350 krad was needed to reduce the light yield of a 1 m fiber by 10%. The total dose for the central and forward preshower detectors as a function of the integrated luminosity is shown in Fig. 26. The dose that the FPS will be exposed to for the expected integrated luminosity of 2 fb^{-1} in Run II is $\approx$10 krad at $\eta = 2$ and $\approx$30 krad at $\eta = 2.5$. Radiation damage is therefore not a concern for either of the preshower detectors.

3.6 Cost Estimate and Schedule

Our estimate of the cost of the FPS is summarized in Table 4. This estimate does not include any contingency. The incremental cost for additional VLPC cassettes, incurred by the addition of the FPS, is included. (The VLPCs for the scintillating fiber tracker and the preshower detectors, have already been ordered.) The single item that contributes the most to the detector cost is the clear lightguide fibers ($255K), which are used to route the signals along the 13 m run from the perimeter of the FPS to the remote VLPCs.

We also include a list of our anticipated schedule target dates in Table 5.

Item	Estimated Cost k$
Engineering and Design	60.0
Scintillator Extrusion and Strip Preparation	34.5
Fiber and Connector Fabrication/Testing	307.2
Module Assembly	78.0
Calibration System	52.5
Detector Assembly/Installation	100.0
Total Detector Cost	632.2
VLPC readout	620.0
TOTAL COST	1252.2

Table 4: Estimated costs, including labor, for the FPS. Contingency is not included. The VLPC cost given is the incremental cost incurred by adding the forward preshower.

Item	Approximate Begin/End Target Dates
Finalize Design	4/96 – 12/96
Scintillator and Fiber Procurements	6/96 – 1/97
Parts Preparation (jigs, scintillator/fiber preparation)	6/96 – 2/97
Module Preparation and Construction	6/96 – 1/98
Construction and Testing of First Prototype Module	1/97 – 8/97
Preparation of Detector Assembly Hardware	1/97 – 6/97
Detector Assembly	6/97 – 6/98
Detector Shipment to FNAL/Installation at DØ	6/98 – 6/99

Table 5: Outline of anticipated target dates for procurement, construction, prototype testing, and installation of the FPS.

4 The Muon System

The upgrade of the DØ muon system to permit improved triggering at high luminosity was originally presented in 1990, and approved in 1991. In this section we describe the implementation of the upgraded muon system based on a better understanding of the performance of the present muon system. We will describe why it is necessary to replace the existing muon chambers in the forward region; we will explain the need to shield against backgrounds and how this is achieved. We will show that plastic mini-drift tubes are the appropriate technology for the new chambers. We will describe why scintilator trigger planes are needed, and how they are used to trigger on muons.

4.1 Introduction

The upgrade of the DØ muon system for Run II was last reviewed at the April 1995 PAC meeting. At that time, the muon upgrade consisted of the existing Wide Angle Muon System (WAMUS) Proportional Drift Tubes (PDTs) with new electronics and a new forward trigger system made up of scintillator pixels and pad chambers. Since that review, the design of the upgraded muon system has undergone a major evolution. The primary reason for the change is the aging of the WAMUS PDTs. The chambers suffer from a radiation-induced buildup of material on the anode wires derived from the cathode pad polyresin material. This cladding can be driven off the wire by applying a short-duration high voltage pulse to the wire (called "zapping") which restores the wire gain to its original value.

Studies of the aging of the forward WAMUS chambers (the "EF" PDTs) reveal that these chambers will not survive Run II [21]. This conclusion results from consideration of Fig. 27 where the luminosity which reduces the wire gain by a factor of $1/e$ is plotted for various groupings of chambers [22]. We can define PDT "lifetime" as this luminosity and stipulate that the chamber must be 'zap cleaned' [23] after one lifetime. For example, Fig. 27 shows that the EF B-layer PDTs (EFB) must be zapped $10-20$ times during Run II ($2\,\mathrm{fb}^{-1}$). Past experience with the time-consuming and difficult zapping operation has shown that a long shutdown is necessary to clean the forward chambers. Given that these shutdowns occur only several times during the course of the run, we conclude that PDTs which require zap-cleaning more than about three times during Run II are not usable. All EF chambers are in this category. The bottom line from the aging studies is that the forward WAMUS PDTs will have to be replaced in order to retain coverage beyond $|\eta| \approx 1$.

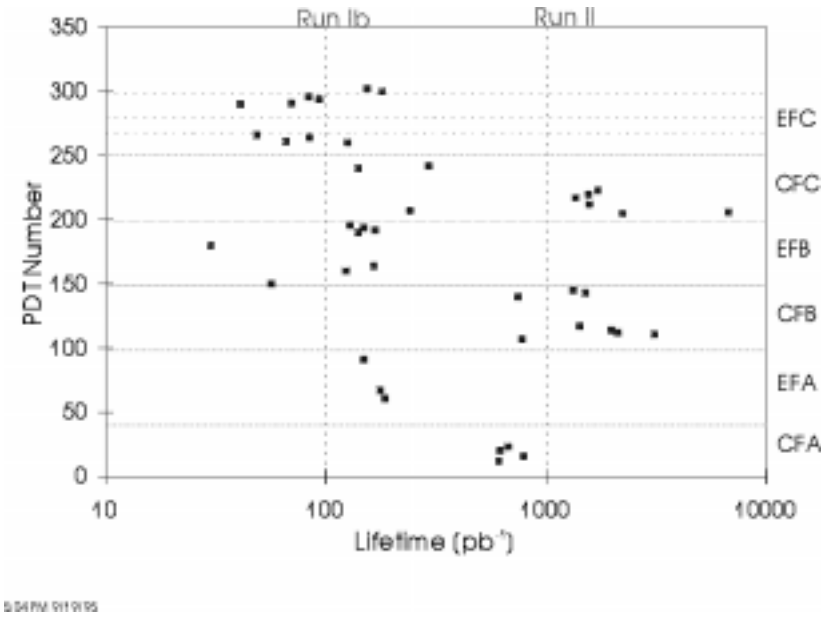

Figure 27: "Lifetime" of WAMUS PDTs versus chamber number. The approximate corresponding region is shown on the right hand axis. (EF=forward; CF=central; Letters A,B,C refer to the three stations before and after the toroid.

Most of the hits in the forward muon detectors are due to remnants of hadronic and electromagnetic showers around the beam pipe [24, 25, 26]. Major improvements in the detector operation, reduced aging, trigger rates and fake track reconstruction probability can be achieved by additional shielding in the region of the beam pipe [24, 26, 27, 28]. Indeed, the most forward PDTs in the central region (CF), the so-called "ring" chambers, will require a shielding factor of $\gtrsim 3$ just to survive.

In light of this, a new design for the upgraded muon system has been developed. The new design was driven by the DØ Run II physics goals. The physics motivations for going to the highest luminosities are to study low-cross-section, high-p_T processes, such as top and W/Z, and to search for new phenomena. In order to maximize the acceptance for muons from these processes, we need sufficient detector coverage and an efficient, unprescaled trigger. It was shown in Section 2 that $|\eta|$ coverage to ~ 2 is required for DØ's physics goals to be met. The new design satisfies this requirement.

The muon trigger in Run II will combine track candidates from the fiber tracker trigger (CFT) with information from the muon system. The effective η range of this trigger for single muons is thus defined by the end of the CFT trigger, *i.e.* at $|\eta| \sim 1.7$. (The second muon in dimuon triggers can extend up to $|\eta| = 2.0$). Studies of Run II trigger rates [30, 31] show that the combined muon/CFT trigger will be unprescaled for high-p_T single muons

($p_T \gtrsim 8$ GeV) and low-p_T dimuons ($p_T \gtrsim 3$ GeV).

Triggering in the high rate environment of Run II requires the use of fast trigger elements with good time resolution. In the central region, the maximum drift time in the existing PDTs of 750 ns exceeds the Run II bunch spacing of 396 or 132 ns, and scintillators will provide the necessary time stamp. In the forward region, accidental triggers from uncorrelated particles in the three layers will be reduced by the use of scintillation counters.

The individual components of the new design will be discussed in more detail in subsequent sections; a brief overview is given here. In general, we have attempted to minimize the number of regional boundaries, chamber technologies, and distinct electronics boards. We have also built in hooks to allow a natural upgrade to $\mathcal{L} = 10^{33}$ cm^{-2} s^{-1}.

The three layers of the muon system are designated A,B,C, where A is closest to the interaction region, and the toroid magnet is located between the A and B layers. For $|\eta| \lesssim 1$, the WAMUS PDTs will be retained but the electronics, from the front-ends to the Movable Counting House (MCH), will be replaced. There will be two layers of scintillator: the existing Central Muon Scintillator C-layer (CMSC C-layer) just outside the WAMUS C-layer PDTs and a new set of CMSC A-layer scintillation counters located between the calorimeter and the A-layer, as discussed and approved over the past two years. There will be a CFT·CMSC A-layer trigger with good geometric acceptance that will enable a trigger on low-p_T muons ($\gtrsim 1.5$ GeV/c) in the central region. There will also be a trigger based on the hits in the PDTs, as in Run I.

For the Forward Muon System (FAMUS), $1 < |\eta| < 2$, the PDTs will be replaced with planes of plastic Mini-Drift Tubes (MDTs). The cells are square in cross section and 1 cm wide. They will be arranged in three layers (A,B,C) with (4,3,3) decks of tubes per plane. There will be three layers (A,B,C) of Forward Muon Scintillator (FMSC) pixels arranged in an $R - \phi$ geometry. The trigger will be provided by a CFT·FMSC requirement. As in the central region, a Run I-style trigger based on the MDT wires will also be implemented, as this will give finer p_T resolution.

To summarize, we have converged on a new baseline design for the DØ muon system upgrade. The performance of this system will allow us to meet the challenges of Run II. However, we will need new tracking detectors for the forward region, in addition to the approved triggering planes, and, in order to provide enough shielding, we must restrict the forward coverage to $|\eta| \lesssim 2$. Therefore the Small Angle Muon System(SAMUS) stations will be removed after Run I. The upgrade system will survive the harsh environment of Run II and upgrade pathways (such as full readout of the WAMUS pads

and precision time readout of the MDTs) are available to handle luminosities up to 10^{33} cm^{-2} s^{-1}. We are ready to complete the detailed design work and proceed to build the system.

4.2 Shielding

The upgrade of the DØ muon system will include the addition of shielding material. This shielding will block non-muon background particles originating from the three hottest sources [27]. The main source is scattered proton and antiproton fragments which interact with both the exit of the calorimeter (producing a background in the central and forward muon A-layer) and the beampipe and low-beta quadrupoles (producing showers in the forward B and C-layers). (The accelerator-produced background which comes from the tunnel is small compared to the direct contribution from interactions thanks to improved shielding that was installed in the tunnel during Run Ib [25].) Shielding these background sources is important because it will reduce the occupancy of the detectors. This decreases the fake trigger and track probabilities and increases the detector lifetime by reducing aging.

The main feature of the B and C-layer shield is a thick iron, lead, and polyethylene casing surrounding the beampipe and final low-beta quadrupole magnet. This is shown in Fig. 28, extending from the calorimeter to the accelerator tunnel. The shield is $\sim$ 170 cm wide on the outside and has an inside hole $\sim$ 50 to 65 cm wide for the accelerator equipment.

The appropriate thicknesses of the iron, lead and polyethylene was determined by Monte Carlo simulations (`GEANT` and `MARS`) for various shielding configurations. Figure 29 (upper) shows the energy deposition from hadrons and electromagnetic showers in the Run I detector configuration for a luminosity of 2×10^{32} cm^{-2}s^{-1}. Figure 29 (lower) depicts the energy deposition from hadrons and electromagnetic showers in the shielded detector. The effect of the shielding is striking. We find that the energy deposition from proton and antiproton remnants is reduced by approximately a factor of 100 with a shield comprised of 39 cm of iron, 15 cm of polyethylene, 2 cm of lead and an additional 8 cm of iron located on the inner core of the shield at the exit of the muon toroid in front of the low-beta quadrupole magnet. As a result, the number of hits in counters is expected to be reduced by about a factor of 40.[32].

Additional polyethylene shielding will be mounted in the gap between the End Calorimeters and the EF toroids to reduce the rates in the CF A-layer detectors due to shower propagation at the rear of the calorimeters through the liquid argon and insulating vacuum space. These shields are shown in

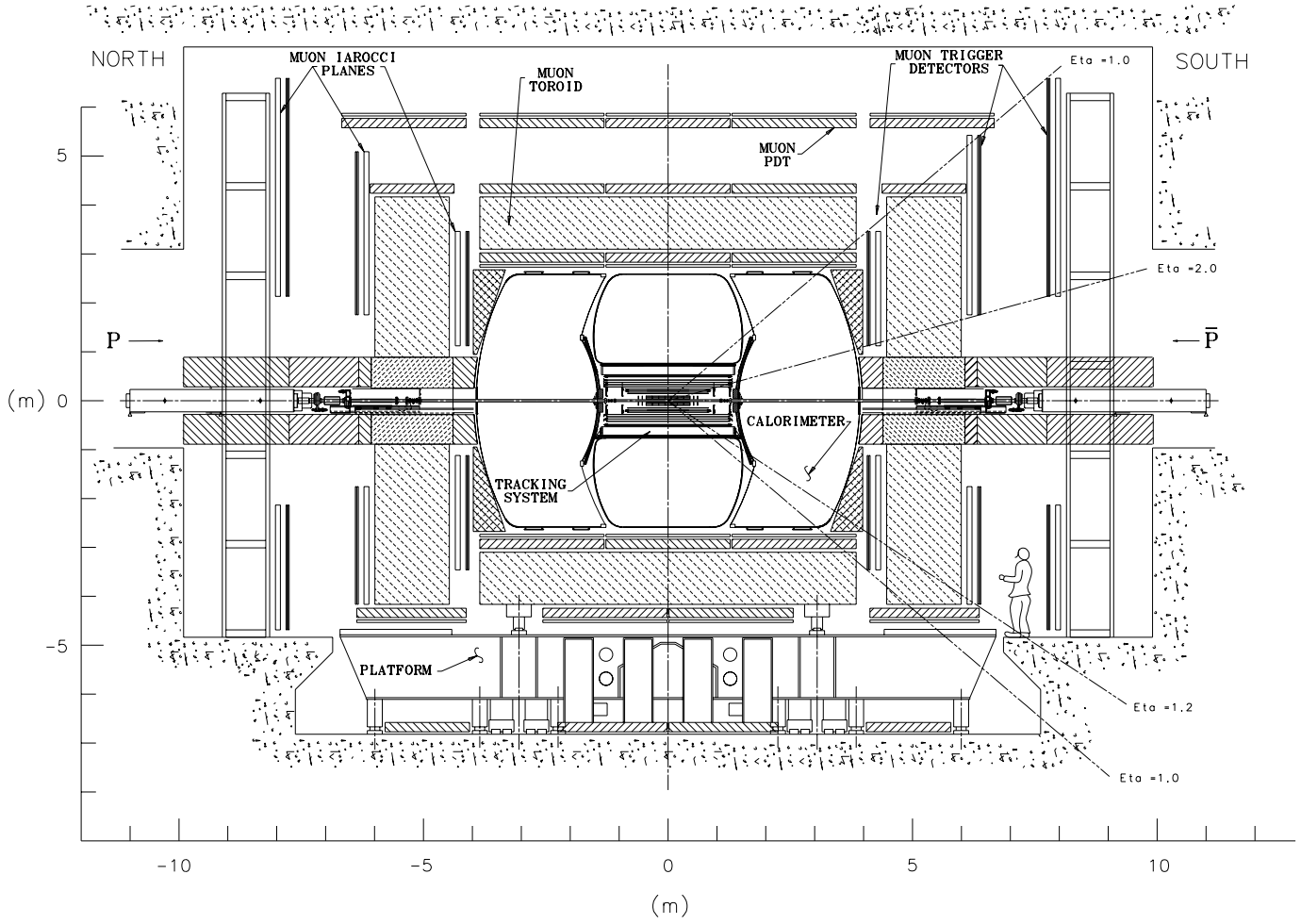

Figure 28: Side view of the DØ detector during Run II showing the various elements of the muon system upgrade and the shielding.

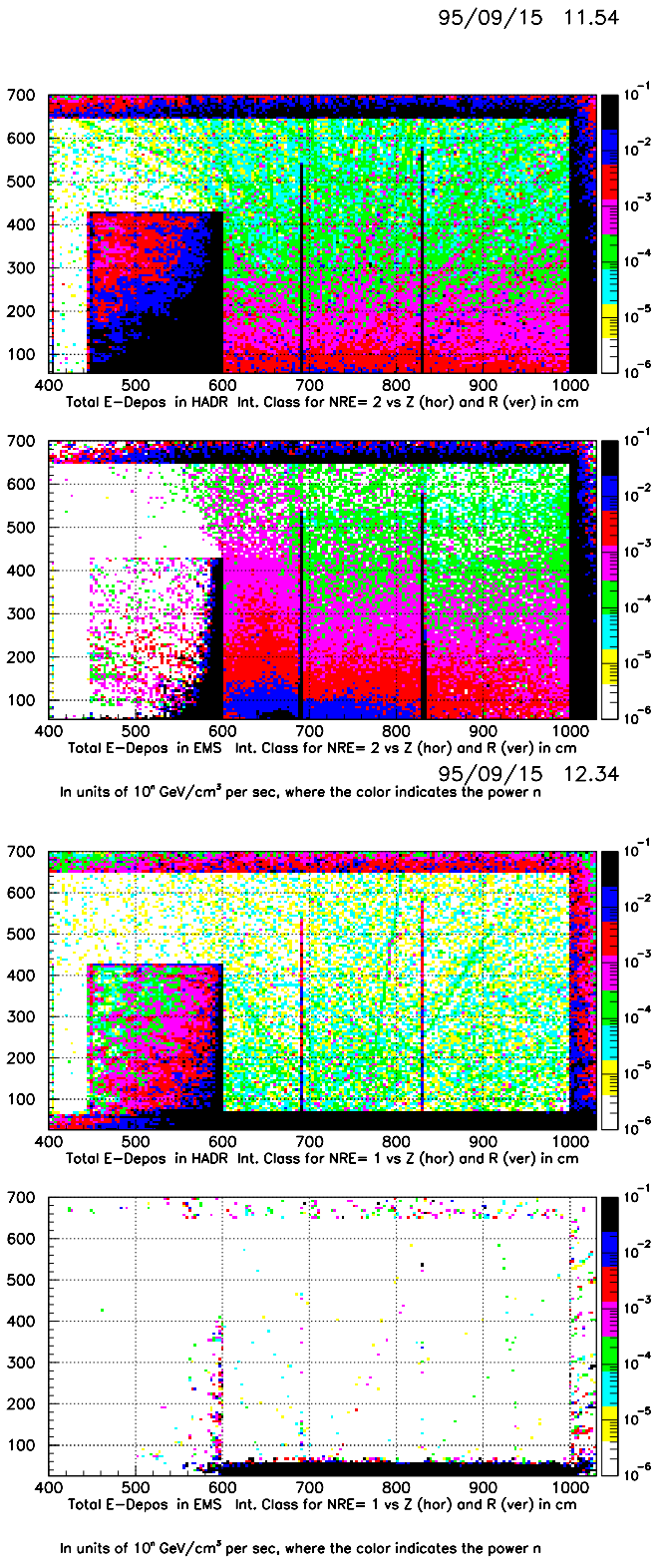

Figure 29: From top: Energy deposition from hadrons (1) and electromagnetic showers (2) in the unshielded detector. Energy deposition from hadrons (3) and electromagnetic showers (4) in the shielded detector. A luminosity of 2×10^{32} cm^{-2}s^{-1} is assumed.

Item	Layer		
	A	B	C
WAMUS PDTs (Drift Cells)	18 (1728)	38 (2424)	38 (2616)
CMSC C-layer (PMTs)	-	-	240 (480)
CMSC CF Bottom B-layer (PMTs)	-	40 (80)	-
CMSC EF Bottom B-layer (PMTs)	-	36 (72)	-
CMSC Bottom C-layer (PMTs)	-	-	40 (80)
CMSC A-layer Counters (PMTs)	630 (630)	-	-

Table 6: Channel count for the various central muon upgrade detectors.

Fig. 28 as cross-hatched triangular sections.

4.3 Central Muon Detectors

The DØ muon detector is composed of detector planes arranged as the surfaces of a box, with the top, bottom, and sides forming the central region and the box ends the forward region. The boundary between the two regions is at approximately $|\eta| = 1.0$. While muon detection for the forward region is being completely redesigned for Run II, we will retain much of the present system in the central region. The 94 CF WAMUS drift chambers and the 480 scintillation counters of the existing CMSC C-layer will receive new electronics. New scintillation counters will be added to the bottom B- and C-layers and to the central A-layer, for triggering purposes. They are shown in Fig. 28 and a channel count is provided in Table 6. The new detectors exploit features of the existing detector (thick calorimeter and iron magnet, small π/K decay volume, etc.), and add high rate capability and good time resolution while enabling the transverse momentum threshold for muon triggers to be reduced.

4.3.1 WAMUS

The WAMUS central region consists of three layers of drift chambers, one layer inside and two layers outside the iron toroid magnet. The purpose is to provide muon identification and a confirming momentum measurement independent of the central tracking. The muon momentum resolution in the central region in Run II will be dominated by the central tracking system. The drift chambers produce the following measurements for each hit: the drift-time T perpendicular to the anode wire; the time difference, ΔT, in the arrival time of the hit between a hit cell and its neighbor (jumpered at the

far end), providing the distance along the wire; and the charge deposition on inner and outer vernier pads, yielding a more accurate measure of the distance along the wire. The Run Ib gas mixture was 90% Argon, 6% CF_4 and 4% CO_2. The maximum drift time was 750 ns (5 cm drift), with the wires operating at 4.56 kV and the pads operating at 2.3 kV. In order to reduce the number of crossings which occur during one drift interval, we are considering using a faster gas mixture during Run II. The gain, drift-time-to-distance and aging characteristics of 80% Argon, 10% CF_4 and 10% CH_4 are being studied. Preliminary results indicate the maximum drift time can be reduced to 450 ns with the wires operating at $\sim$ 5.0kV and the pads operating at $\sim$ 2.5kV. The contribution to the hit uncertainty due to diffusion is estimated at less than 500 microns, worse than the present $\sim$ 300 microns, but smaller than the 700 micron residual typically achieved in WAMUS chambers during Run I. The trade-off in resolution is offset by the reduced occupancy and benefits to triggering and reconstruction achieved by decreasing the number of crossings in one drift time from 6 to 4 for 132 ns bunch spacing operation.

The electronics will be modified to provide a deadtimeless front-end readout with either 396 or 132 ns bunch spacing. We will read out the T and ΔT from all of the chambers. Although not instrumented initially in all chambers, readout of the pad information can be added. The latched hit cells will be available for the Level 1 muon trigger, as in Run I.

4.3.2 Central B- and C-layer Scintillation Counters

The existing CMSC C-layer counters[33] cover the top and sides of the central region with 12 divisions in ϕ and 20 divisions in z. The purpose is to provide a fast trigger detector outside of the toroid magnet and to tag the crossing for hits in the WAMUS B and C-layers. The background rate is small in comparison with other detector regions; very tight timing is not necessary to achieve adequate rejection. These counters exist and have been used during Run I to reject cosmic ray muons. They have achieved timing resolution of 2.5 ns after offline corrections (online, the counters have timing resolution of $\sim$ 5 ns).

The bottom of the central region was not covered with scintillation counters during Run I but must be for Run II. The "CMSC Bottom" includes the CF Bottom B- and C-layer counters and the EF Bottom B-layer counters. The design is similar to the existing counters: scintillator sheets with wavelength shifting fibers for light collection. Forty counters will be located on the B-layer chambers underneath the CF muon toroid. These are referred to as the "CF B-layer Bottom" counters. A minor difference between these counters and those in the CMSC C-layer is that these counters will be oriented with the short dimension along ϕ so that they cover an interval of

approximately $4\frac{1}{2}$ degrees. The smaller ϕ segmentation is advantageous for matching with the CFT trigger tracks. The counters are $15\frac{3}{4}$ inches wide or $22\frac{3}{8}$ inches wide and $98\frac{1}{8}$ inches long. The narrower counters are located directly under the calorimeter supports where there is no A-layer coverage. A full-size prototype has been built and tested. Construction of these counters began at the Tata Institute in February, 1996. The EF B-layer bottom, located on the PDTs just underneath the North and South EF toroid magnets, consists of 36 counters 88 inches long and $15\frac{3}{4}$ inches wide. The CF C-layer Bottom counters are located underneath the north and south ends of the platform and consist of approximately 40 counters similar in design to those described above.

4.3.3 Central Muon Scintillator A-layer Counters

The CMSC A-layer counters [34] will be located between the Central Calorimeter and the WAMUS central A-layer PDTs. The purpose is to provide a ϕ measurement matching high and low p_T triggers with the central tracking system, and to reject out-of-time backgrounds originating at or near the exit of the calorimeter. The counters divide the A-layer into rows covering $4\frac{1}{2}$ degrees of ϕ. Each row contains nine counters that cover three 100 inch wide PDTs. The counter widths vary from 10 to 17 inches in order to maintain a constant segmentation in ϕ. Figure 30 shows a view of the CMSC A-layer scintillator array on the east or west A-layer wall. The scintillator is $\frac{1}{2}$ inch thick Bicron 404a and light collection is accomplished with Bicron G2 waveshifter fiber. This waveshifter has a fast (2.7 ns) decay time and is well-matched to the scintillator and PMTs. The photomultipliers are Russian MELZ 115M tubes which have a 1" diameter. Prototype counters have been studied with this configuration. Over the surface of the counter, the response to minimum ionizing particles is constant to within $\sim$ 10% with a timing spread of about 4.7 ns. We have operated test counters in the CF A-layer during Run Ic, and have verified that muons are well separated from the background and in good agreement with Monte Carlo.[34]

All these counters will be outfitted with new, pipelined electronics for a deadtimeless readout. A hit in-time with a narrow gate ($\sim$ 20ns) will be latched and the time will be measured with a TDC. The latched hits will be used in the Level 1 trigger. An electronics pulser and an LED light pulser will be used for time and gain calibration.

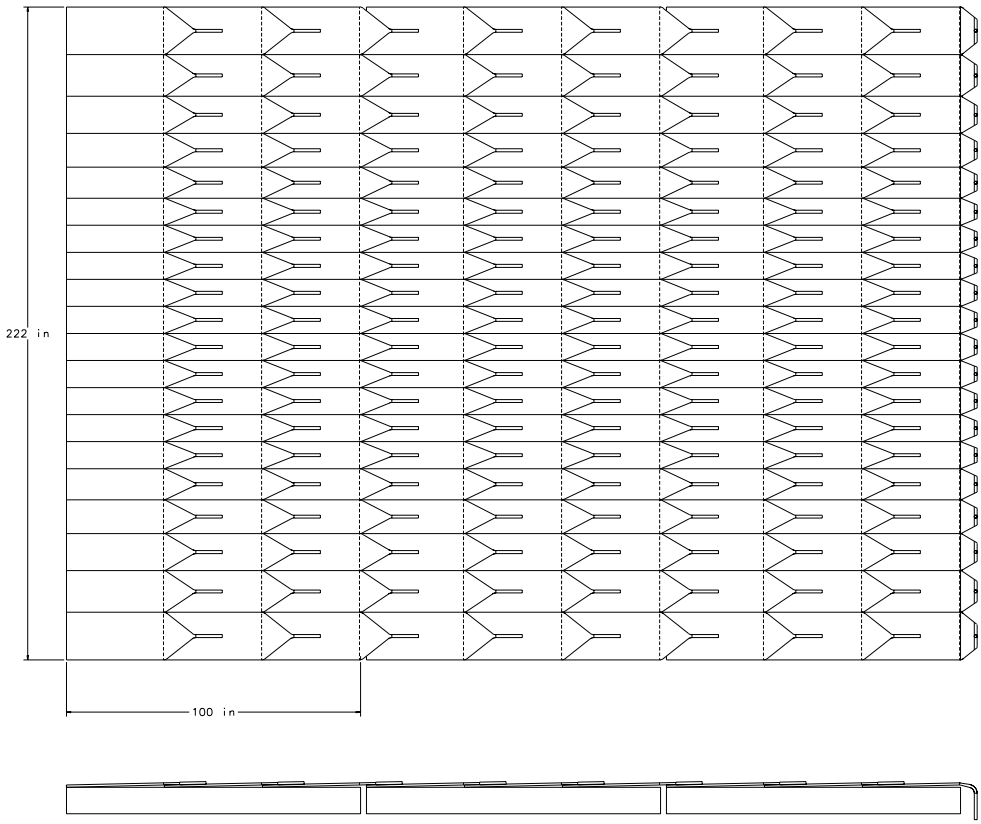

Figure 30: The CMSC A-layer counter array of the east or west wall A-layer.

4.4 Forward Muon Detectors

Plastic mini-drift proportional tube planes and scintillation counters will be used for forward muon triggering and track reconstruction.

4.4.1 Mini Drift Tube System

The Mini Drift Tube (MDT) design has a 10×10 mm^2 internal cross section with 50 μm anode wires in the center of each cell. The cells, in packs of eight, are made from plastic extrusions as long as 5 m. The internal surfaces of the tubes are covered with conductive paint (1 kΩ/square) to form the cathode electrode. The extruded tube construction is the same as that used in Iarocci counters, which have been used extensively in collider experiments [35]. Iarocci tubes are usually operated in limited streamer mode with cathode readout, but in this application the tubes will be run in proportional mode with readout of the anode wires in order to facilitate high-rate operation. Filled with a fast gas mixture, such as Ar(80%)+CF_4(10%)+CH_4(10%), these tubes will have a maximum electron drift time of 60 ns. The planned gate width of 90 ns is well within the 132 ns bunch spacing. This constitutes a significant advantage over the larger drift cells in the WAMUS system.

The layout of one MDT plane is shown in Fig. 31. The tubes are oriented along magnetic field lines (the field shape in the EF toroids is more "square" than "circular"). The flux of particles decreases with increasing distance from the beam pipe, so the occupancy per cell is approximately constant: using the geometry shown in Fig. 31 the occupancy of individual cells will vary only a factor of two over the entire plane.

A typical time distribution of C-layer hits is shown in Fig. 32 (with shielding discussed above). This figure was obtained from a `GEANT` simulation for a single bunch crossing. There is a long time tail with decay time around 2 μs. Overlap of these tails from many crossings provides an almost uniform background, which is not included in Fig. 32.

An additional advantage of the MDTs is the small gas volume. They have only one fifth the sensitivity to fast neutrons of the WAMUS chambers [36].

The intrinsic efficiency of an individual MDT cell is near 100%, but due to the tube walls, the efficiency of a plane is 90% for normal incidence (1 mm wall/10 mm cell). In practice, most tracks will not be at normal incidence, so the geometric efficiency is higher than 90% per layer. We assume a single-layer efficiency around 92%, which corresponds to results from prototype studies at 45° incidence. In order to have a track vector from each layer,

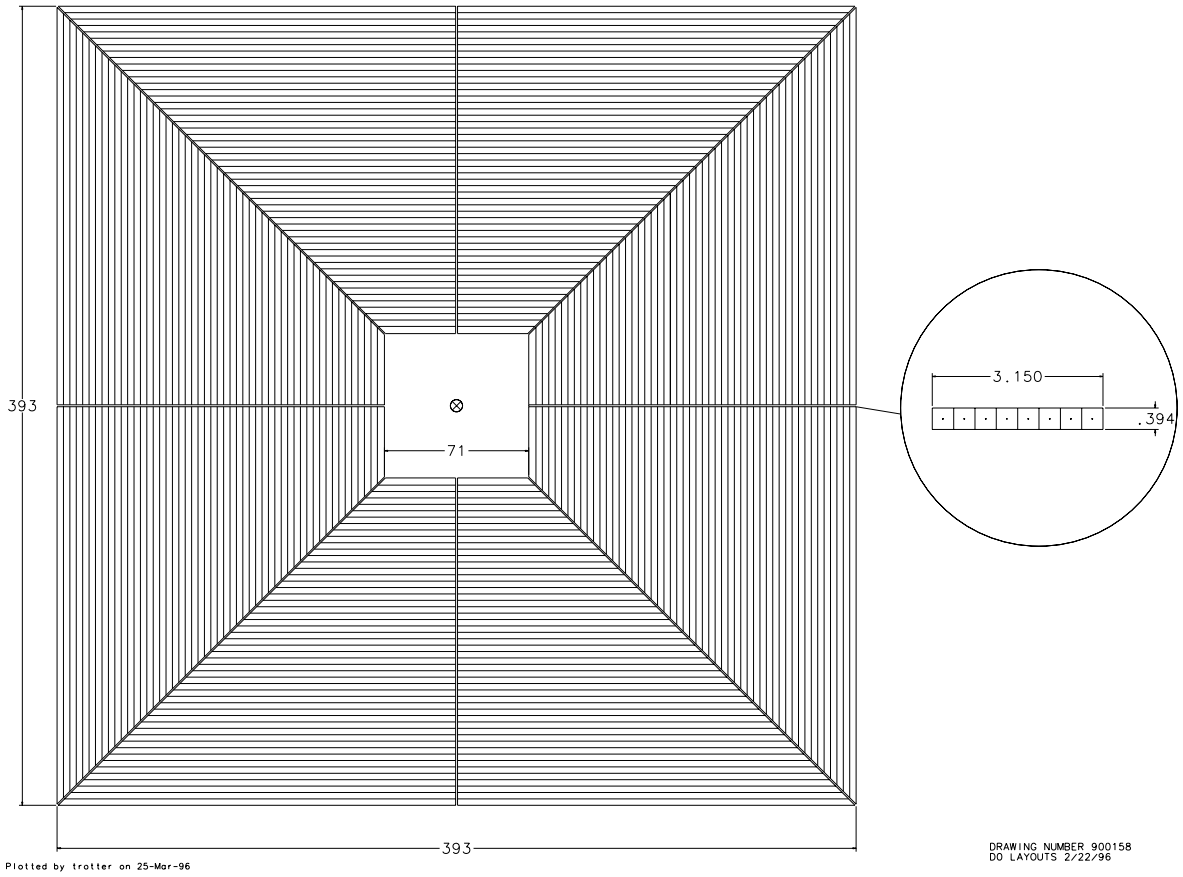

Figure 31: Mini Drift Tubes: individual 8 tube module and one complete plane

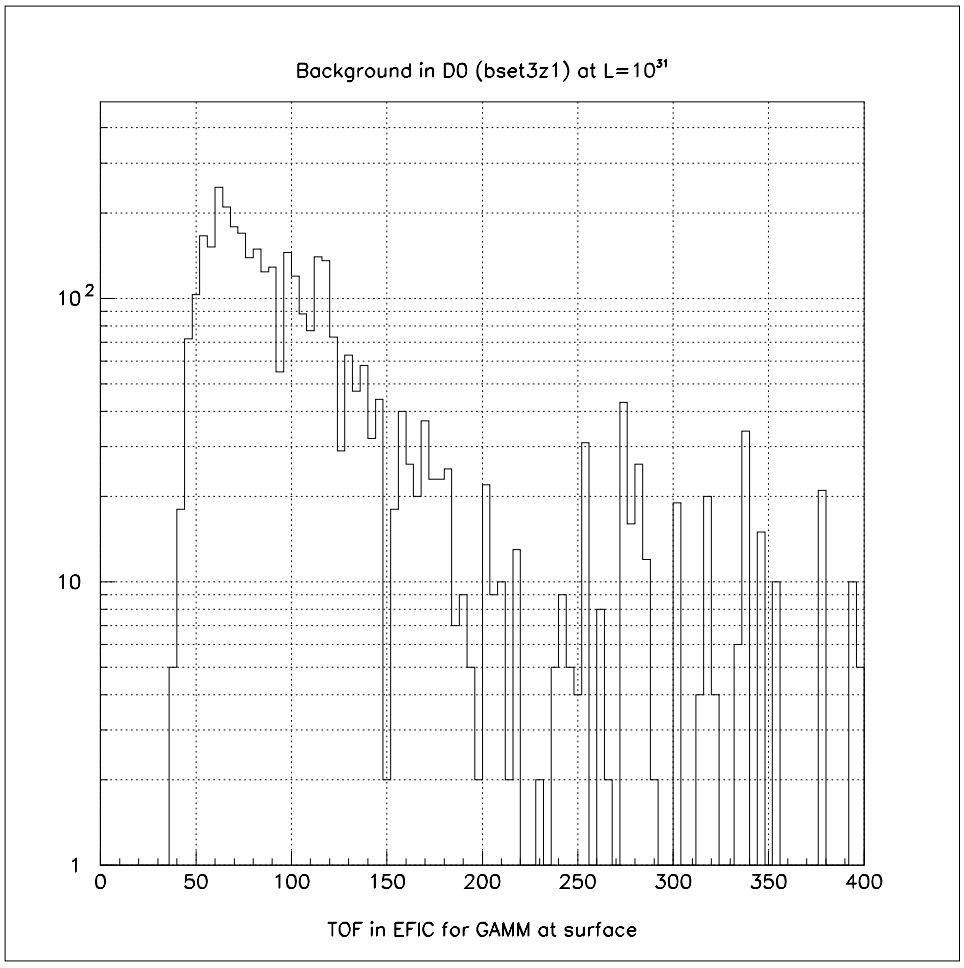

Figure 32: Time distribution [ns] of hits in the C-layer muon detectors. The real prompt muon peak is at 27 ± 7 ns.

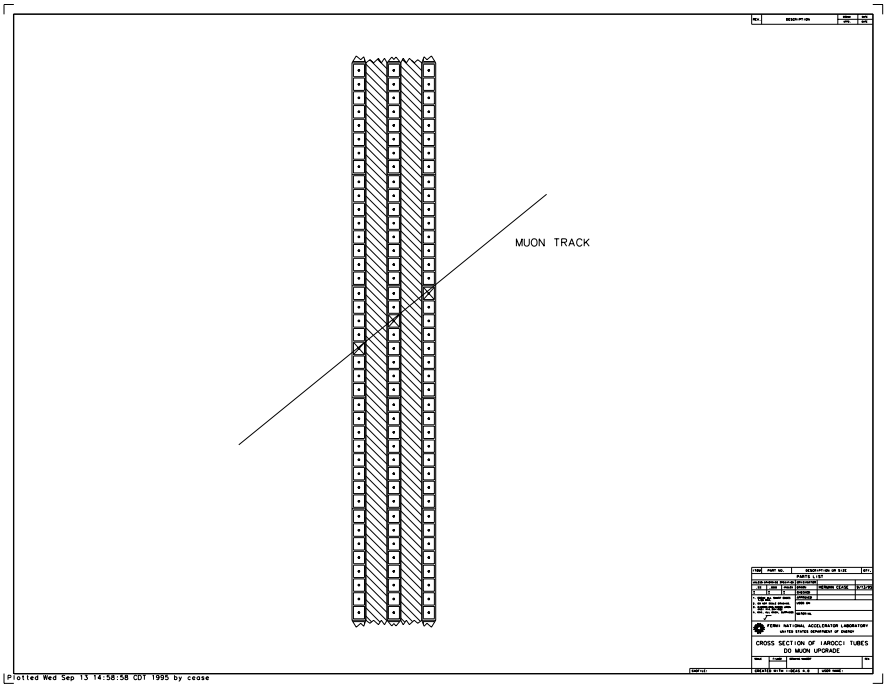

Figure 33: MDT B and C-layers design

the planes will be separated by 20 mm (see Fig. 33). In order to reduce the probability of track segment formation by low energy electrons, the gap between the MDT planes will be filled with polyethylene. The energy of electrons from neutron interactions is below 1 MeV and they can be absorbed by 5 mm of polyethylene.

To reconstruct muon track segments, at least two hits per layer are needed. For three planes per layer (as shown in Fig. 33) the efficiency for two-out-of-three hits is 98%. For the B and C layers we propose to use three planes of mini-drift tubes per layer, while the A-layer has four planes since the A-layer background flux is a factor of 3 higher than for B and C. In order to detect soft muons (that range out in the EF toroid) we will use three points on an A-layer track segment: two to find a segment and the third to confirm it. The 3-out-of-4 efficiency is above 96%. The reasonably large number of points on a track will improve the accuracy of the track reconstruction (both the momentum resolution and the match with the central detector) and make track reconstruction algorithms more robust. The 4(A-layer)+3(B-layer)+3(C-layer) design is similar to the central WAMUS design.

The solenoid tracker momentum resolution falls off in the forward direction and the contribution from the muon system becomes significant. The momentum resolution of the muon system is limited by multiple scattering and the coordinate resolution of the muon detector. The typical coordinate

resolution of WAMUS and SAMUS detectors (per layer) in Run I was around 1 mm. Mechanical inaccuracies, survey accuracy, and the time-to-distance calibration are the major factors limiting resolution. For three planes of MDTs, the per layer effective coordinate resolution is around 1.7 mm, and thus not the limiting factor in resolution.

The total number of MDT 8-cell modules is 6,000 (48,000 individual channels). They will be produced and tested at JINR (Dubna) and shipped to FNAL for final assembly. We plan to use the existing SAMUS high voltage (HV) and gas systems. These HV power supplies can produce currents sufficient for operation at the Run II design luminosities. In total, 48 HV channels will be used, one per octant.

We plan to use the MDTs for both track reconstruction and triggering. Since the gate width can be set below the 132 ns bunch crossing time, simple amplifiers/latches can be used.

Experience with SAMUS tubes shows that an integrated charge of 50 C/cm on the anode wire can be accumulated without changes in gas amplification using a freon-methane gas mixture (similar to the one we propose for the MDT's). Preliminary studies of the MDTs show that there is no outgassing from their internal surfaces. This suggests that MDTs can run for many years at $\mathcal{L} = 1 \times 10^{33}$ cm^{-2} s^{-1} without aging. Studies of MDT aging with the selected gas mixture in the proportional mode show gain decreases of less than 2% for integrated charges of 2C/cm. This charge is considerably more than that expected in the lifetime of the experiment.

4.4.2 Forward Scintillator Counters

The time and energy spectra of background particles are substantially different than those from real muons. Scintillation counters will register substantially fewer background hits than other types of detectors [37, 34]. Use of a 20 ns gate (instead of 100 ns) reduces the number of background hits per plane by a factor of five. The minimum ionizing energy deposition in 1/2 inch plastic is 2.5 MeV. Setting a detection threshold at 0.5 MeV will reduce the counting rate due to neutrons by a factor of three[38].

We propose to install three layers of Forward Muon Scintillation counters (FMSC A-, B- and C-layers) with $\Delta\phi = 4.5°$ and $\Delta\eta = 0.1$ segmentation in the forward region (Fig. 34). This segmentation has been optimized with respect to multiple scattering, the fiber tracker trigger azimuthal segmentation, the minimum muon momentum, background trigger rates, and the number of channels [30]. The minimum pixel size is dictated by the requirement of triggering efficiently on muons down to $p_T = 3$GeV, where the typical multiple

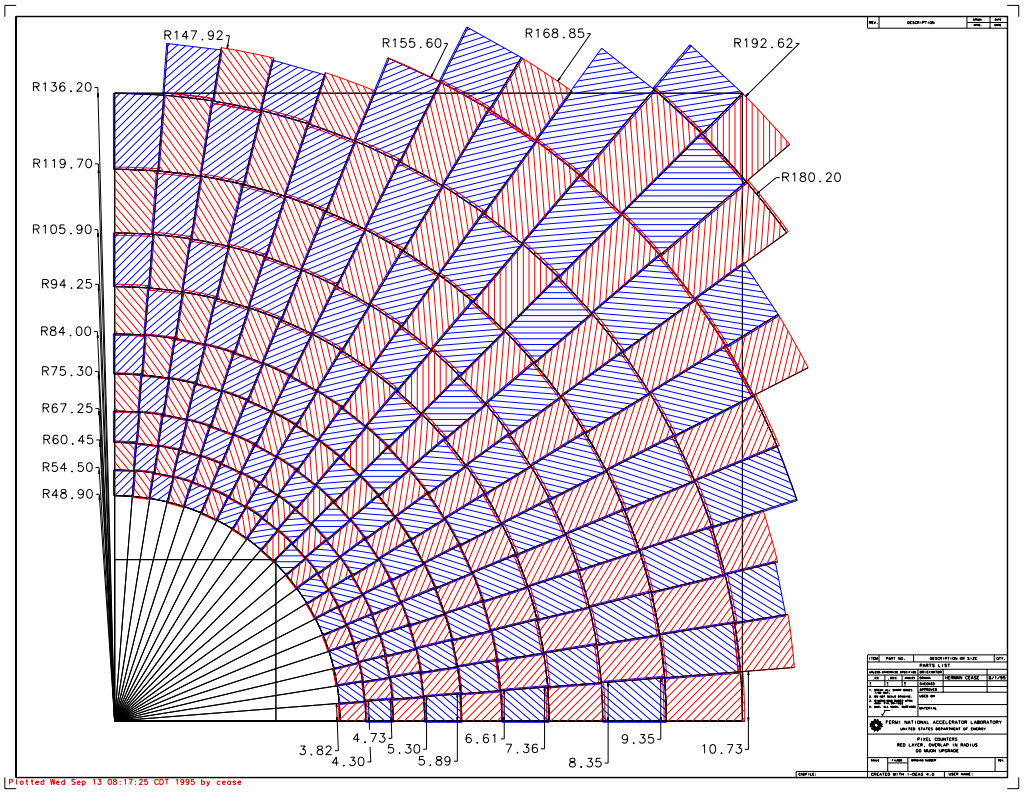

Figure 34: One quadrant of scintillation pixel plane.

scattering angle is about 3°. On the other hand, fine granularity is needed in order to keep the combinatoric backgrounds under control. Since the combinatoric rejection varies as n^3 for 3 layers of n scintillator pixels in coincidence with the CFT trigger, a factor of two coarser granularity would give almost an order of magnitude increase in accidental triggers. Each plane consists of two overlapped sub-planes in order to remove any dead zones between counters. The maximum counter size is 60×110 cm^2.

A tower of three layers of prototype counters located at $\eta \approx 1.6$ was tested in Run Ic, at luminosities which correspond to the same average number of interactions/crossing that is expected in Run II at $\mathcal{L} = 2 \times 10^{32}$ cm^{-2}s^{-2} with 132 ns bunch spacing. These tests showed that the background hits in the three layers were largely uncorrelated. A three layer coincidence of the prototypes achieved a signal-to-background ratio of about 1:140. After corrections for the expected reductions from shielding and the larger size of the actual trigger towers with respect to the prototypes, a signal-to-background of about 1:10 is expected from the scintillator coincidence alone. Additional rejection from the CFT and/or MDT planes should reduce the combinatoric background even further.

There are two options for the FMSC light collection design under detailed study. The first is based on two wavelength shifting (WLS) bars used for collection of light into the photomultiplier [37]. The high transparency of Bicron BC404A 1/2" scintillator provides a large number of photoelectrons (more than 60 for the largest counters) and good uniformity (within $\pm 10\%$). In the second design, twelve 1 mm diameter WLS fibers (Bicron G2 fibers with decay time of 2.7ns) are installed around the counter perimeter to collect light from all four sides of the plastic. This design has the advantage of a better photomultiplier connection and counter design, but fewer photoelectrons and a more complex assembly/production procedure. Each design has been selected from prototype studies with about 10 different geometries, and the performance of these two optimized configurations is quite comparable, with about 60 photoelectrons from a minimum ionizing particle passing through the center of the counter. A time resolution of 0.8–1.4 ns has been obtained for test counters. Both counter designs use 1 inch Russian MELZ 115M photomultipliers. These PMTs offer substantial cost savings over the similar tubes from EMI ($50/tube vs. $150/tube).

The total number of FMSC counters in the proposed system is 4608. They are grouped into octants matching the MDT arrays. There are about 96 counters per octant.

Calibration of the scintillation counters (time and amplitude) is necessary in order to maintain high efficiency for muon detection. A calibration system using pulsed LEDs is under development. We plan to perform long term stability studies using prototype pixel counters to verify the reliability of this system. In addition, the rate of muons with low p_T (around 3 GeV/c) produced in $p\overline{p}$ interactions should be sufficient to refine the calibration. At $\mathcal{L} = 2 \times 10^{32}$ cm^{-2} s^{-1}, the inclusive muon rate will be of order 1×10^2 Hz. Estimates show that we can collect around 5×10^2 events per counter during a 30 minute calibration run.

4.5 Front-End Electronics

There will be new front-end electronics for all the muon detectors in Run II. The electronics design is well developed[39]. The readout part of the WAMUS electronics is the basic model for the fast trigger-detector electronics design.

4.5.1 Wire Amplifier

The wire amplifier design takes advantage of new, lower power commercial IC's to achieve comparable noise performance to the present system. Per-

formance improvements include the addition of transformer coupling at the high voltage distribution boards to provide a true differential connection and avoidance of low impedance ground paths between the chambers and the preamplifier inputs. The determination of which tube in a pair is hit will be achieved by separating the arrival time by about 20ns, through the use of a lumped constant delay line in series with the jumper joining the far ends of the tube pair. Similar preamplifiers will be used for the FAMUS MDT system.

4.5.2 Time Digitization

The drift time measurement will be made with a four channel pipelined digital TDC chip (TMC) developed by Arai at KEK [40], which matches our needs very closely. The bin width, when run at 26 MHz, is 1.2 ns and the maximum delay is 4.8 μs, enough to cover the Level 1 trigger latency of 4.1 μs. The pipeline can store one hit per clock cycle, which means that there is no practical limit to the maximum number of wire hits recorded during one drift time interval.

The time of arrival difference between each end of the WAMUS tube pairs is used to break the ambiguities of the repetitive pad pattern. For a least count time ΔT, the resolution is $\sim c \cdot \Delta T/5$. Therefore, to resolve the pads (pattern repeat length = 61 cm) with a resolution of 30 cm, a least count resolution of ~ 5 ns is required. We propose to calculate ΔT by subtracting time values from adjacent tubes.

The drift times themselves determine the muon momentum. On a test chamber using cosmic rays, we have achieved 0.4 mm resolution[41]. For WAMUS, even with a fast gas ($V_d^{-1} = 16$ ns/mm), this implies a time resolution of 6.4 ns or a least count of 22 ns. The time difference requirement drives the specification and the TMC resolution makes a small contribution to the drift distance measurement error. This resolution is also well matched to the time resolution of the FMSC counters, which also use the TMC chip for time digitization. In the 48,000 channel FAMUS MDT system, each input channel will have a latch similar to the scintillator counter card design and a digital delay based on commercial 18 bit FIFO instead of the TMC chip. This will allow deadtimeless operation for all the components of the muon system.

4.5.3 Charge Integration

At present, pad charges are sampled synchronously with the bunch crossings. The majority of the charge is delivered in 350-400 ns and we will sample

only for this time. The new charge preamplifier will feature a reset switch to eliminate saturation problems, and reduced input impedance in order to collect the pad charge as rapidly as possible. The new pad integrator has about the same wide band RMS noise (1.2 mV) as the old amplifier and the same gain (300 mV/pC). The recovery time of the integrator is about 20 ns which allows us to use a reset pulse 50 ns wide.

The pulse height ratio in the pads yields the coordinate orthogonal to the drift direction. For the pad repeat pattern of 61 cm, we achieved a resolution of $\sim$2 mm on a test chamber[41]. In order to achieve that resolution we need to make 1% measurements of the individual pad pulse heights. This performance can be achieved with low cost 10-bit 15-Msps ADCs.

4.6 The Muon Trigger

4.6.1 Introduction

One of the design specifications for the DØ muon system upgrade is that detectors provide enough information to the Level 1 and Level 2 muon triggers to ensure an unprescaled moderately high p_T single muon trigger and unprescaled low p_T dimuon trigger. Details of the Level 1 muon trigger are described in this section.

There are two major components of the trigger rate at a given luminosity: real muon rates (π/K decays, heavy quark decays, W/Z, Drell-Yan, *etc.*) and background (combinatoric) rates. The single inclusive muon rates can be estimated with precision using measured muon cross sections [42]. The typical single muon rate for $p_T > 3$ GeV/c is of order 10^2 Hz at $\mathcal{L} = 2 \times 10^{32}$ cm^{-2} s^{-1}. The real muon rate is reduced to a few Hz for p_T above a threshold of 10 GeV/c. The combinatoric background is considerably more difficult to estimate. The typical rejection needed in an inclusive muon trigger is 10^6 and therefore very large Monte Carlo samples are needed in order to make direct estimates. There has been considerable progress since the last PAC review in estimating muon trigger rates through detailed simulation using `GEANT`. This simulation work is discussed below. In addition, rough estimates have been made by using a fully parametrized simulation based on expected detector occupancies [30, 31] and by performing Monte Carlo calculations at high background levels (where trigger rejection is lower) and extrapolating to lower background levels [37]. These background rate estimates are in good agreement with the full `GEANT` trigger simulation.

The muon Level 1 trigger will include MSC counters, WAMUS PDTs or FAMUS MDTs, and the central fiber tracker (CFT). Raw data (times) from

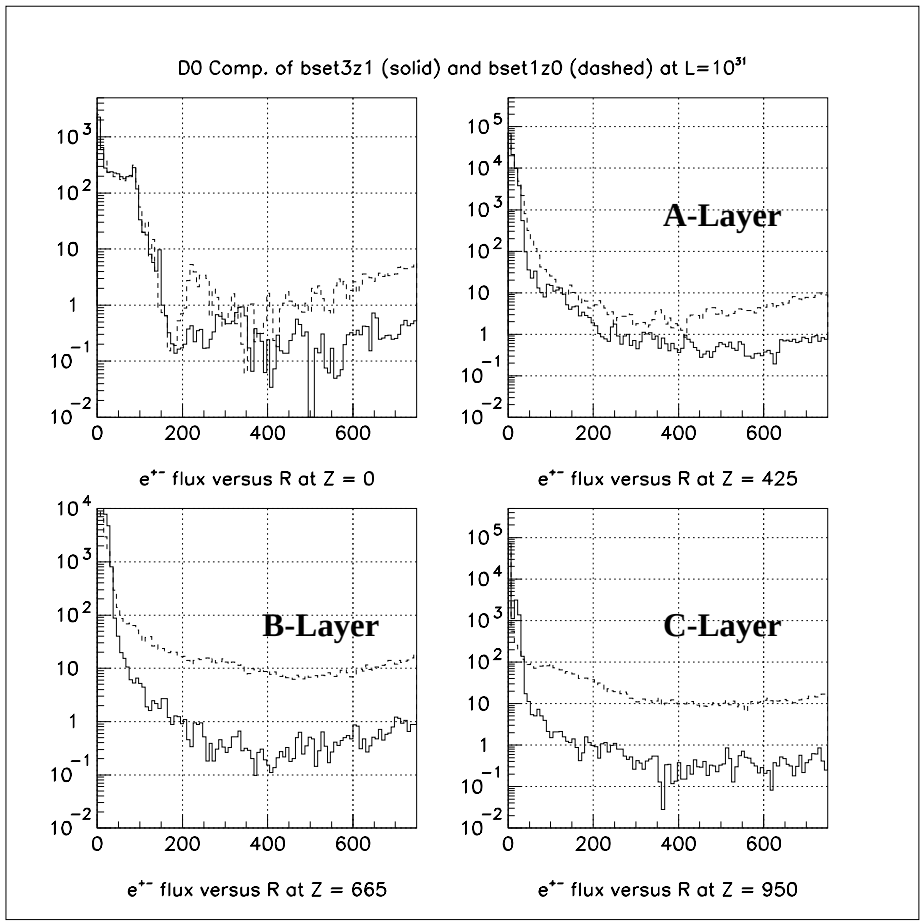

Figure 35: Radial (in cm) electron/positron flux distributions for different z positions: for unshielded (dotted) and shielded (solid) scenarios. The luminosity for this plot is 1×10^{31} cm^{-2} s^{-1}.

the same devices will be used at Level 2 in conjunction with processed information from other detectors. All DØ detector elements (including calorimetry for muon energy deposition confirmation and central tracking detectors) will be used for muon identification at Level 3.

In the central region, the complete hit map for a particular collision cannot be determined until the maximum drift time has elapsed. Since the sensitive time of the WAMUS detectors is greater than the crossing interval, the trigger logic cannot correlate hits and crossings. Thus the Level 1 trigger hardware will use the scintillation counters to eliminate most of the false candidates.

Use of MDTs for the forward Level 1 trigger has two substantial advantages: the possibility of making a high p_T trigger with a threshold around

10 GeV/c (the MSC counters can only provide a p_T cut at 3 GeV/c or below) and additional reduction of combinatoric background. Even for the conservative assumption that the hits in planes of one layer are 100% correlated, we calculate an MDT-based rejection of combinatoric background triggers of a factor of 100 ($\mathcal{L} = 2\times10^{32}$ cm^{-2} s^{-1}, 396 ns bunch crossing time). Taking into account the possible match between MDT-octants and FMSC-towers, additional background rejection can be obtained. Our estimates show that the proposed detectors can be used for muon triggering and track reconstruction up to the $\mathcal{L} = 10^{33}$ cm^{-2} s^{-1} range.

Typical fluxes of electrons/positrons vs. distance from the beam axis are presented in Fig. 35. For $|\eta|$=2, the distance from the beam pipe is around 1.5 m. In this region the variation of background fluxes is relatively small. Using average fluxes from Fig. 35 and the method from Ref. [30], we can estimate the single muon trigger combinatoric rates for the FMSC counters. For $\mathcal{L} = 2 \times 10^{32}$ cm^{-2} s^{-1} and bunch spacing of 396 ns, the rate will be around 2×10^2 Hz ($1.0 < |\eta| < 2.0$). The accidental coincidence rate is proportional, in our case, to $\mathcal{L}^3$ while the real muon rate increases only linearly with luminosity. Any correlations between hits in the A, B and C-layers will increase background trigger rates. Studies with prototype FMSC counters in Run Ic showed that the rates are dominated by uncorrelated combinatoric hits, as long as the layers are spaced sufficiently far apart. The rejection was seen to degrade with respect to the ideal case when the layers were positioned $\approx$ 1m or closer to one another.

4.6.2 Level 1 Muon Trigger

A block diagram of the Level 1 muon trigger is shown in Fig. 36. The Level 1 muon trigger makes use of all muon detector elements as well as the central fiber tracker. Note loose timing windows are used on all scintillator front end cards and hence scintillator timing cuts are an implicit element of the muon trigger logic.

The need to have high rejection and low deadtime dictates the use of multiple levels of triggering. In order to eliminate deadtime, there must be a way of storing data long enough for a trigger decision to take place. For the TMC, this storage is already present in the chip. For the cathode pad ADCs, we must supply a pipeline and tag bits externally. If the trigger latency is of order 4 μs, then the pipeline has to be about 100 locations deep.

The trigger logic generates a candidate list of hit bits at a 7.59 MHz rate (in the case of 132 ns crossings). The need to send trigger bits to the Level 1 processor at this speed defines the bandwidth requirements for the highest-speed link in the muon system. One WAMUS chamber can generate

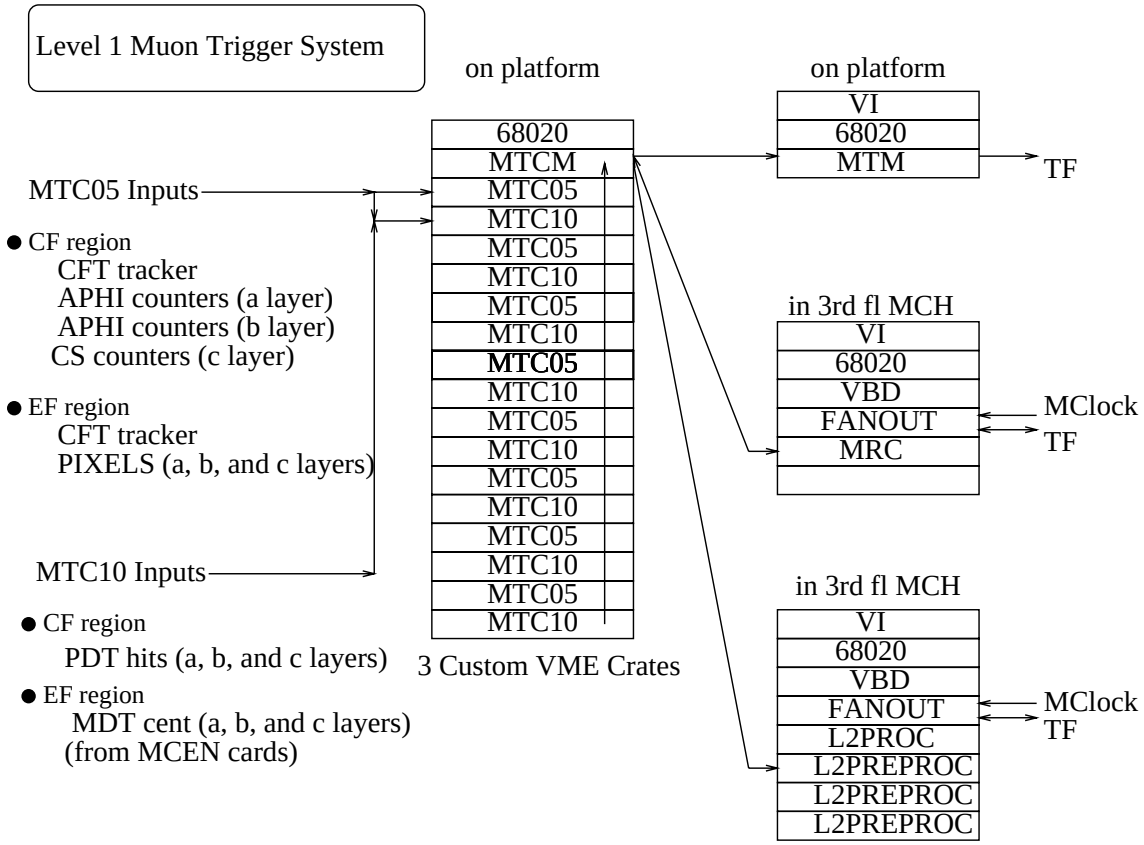

Figure 36: Block diagram of the Level 1 muon trigger.

a maximum of 96 hits. Six 16 bit words must then be sent every 132 ns which is 90 Mbytes/s. Relatively low cost serial links with rates as high as 1 Gbit/s developed for telecommunications have recently become available. These links meet the Level 1 bandwidth requirements and carry data on a single coaxial cable.

The Level 2 input bandwidth requirements will be much lower than those for Level 1. If we assume 30% occupancy, a WAMUS chamber can produce 32 hits. These hits could be encoded in about 120 bytes. If we assume a link bandwidth of 10 Mbyte/s, the event is transferred to the Level 2 processor in about 12 μs, a fraction of the 100 μs Level 2 accept time. Tests have been performed to determine the maximum bit rate sustainable on the coaxial cables presently used for sending analog data to the MCH from the platform. It appears that data can be transmitted over these lines at 160 Mbit/s, which is more than adequate for the Level 2 trigger requirements.

The maximum mean rate for Level 2 accepts is 1 kHz. If again a 10 Mbyte/s link is used, it is obvious that, at 12 μs per event transfer time, a small fraction of the link bandwidth would be used. We can easily transmit data on the cables already installed. The use of all digital systems should also greatly simplify operation.

The trigger system will consist of three crates corresponding to the central region and each of the two forward regions. Each region is further subdivided azimuthally into octants. In each region of the detector (north, central, and south) trigger decisions are made locally in each octant using MTC05 and MTC10 cards. In the central region, MTC05 cards make local trigger decisions based on coincidences between CFT tracks and CMSC A-layer (CMSCA) and CMSC scintillation counters. Central MTC10 cards make trigger decisions using coincidences between A, B, and C layer PDT centroids as well as coincidences between CMSC A-layer counter hits and A-layer PDT centroids. End region MTC05 cards form triggers based on coincidences between CFT tracks and the three layers of FMSC counters. End region MTC10 cards make trigger decisions based on coincidences between A, B, and C layer MDT centroids. A and B-layer FMSC information is also used in the EF MTC10 trigger decision.

A crate manager (MTCM) reads the local trigger decisions from each of the eight MTC05 and MTC10 cards and forms a trigger decision for each region. Finally a trigger manager reads the regional trigger decisions from each MTCM card and sends a global muon trigger decision to the trigger framework for use in physics triggers.

4.6.3 Event Generation and Simulation

The DØ upgrade detector was simulated using `GEANT`. All detectors that will be present in Run II were included, together with the iron, lead and polyethylene shielding surrounding the beam pipe and low beta quad as well as the polyethylene shielding between the EC calorimeter and EF toroids.

ISAJET two jet events with jet E_T from 2 to 500 GeV were used to model minimum bias events. Files containing one, two, four, six, and eight interaction events were passed through the detector simulation and then run though the trigger simulator described below.

4.6.4 Level 1 Muon Trigger Simulation

All Level 1 muon trigger logic described above has been implemented in FORTRAN routines in a muon trigger simulator. Triggers investigated include CFT·CMSCA, CFT·CMSCA·CMSC, CFT·FMSCA, CFT·FMSCA·FMSCB · FMSCC, A·B·C centroids from PDTs, A·B·C centroids from MDTs, and triggers corresponding to combining MTC05 and MTC10 local trigger decisions (much as the MTCM card does). (The "·" above refers to coincidence.) The validity of all trigger algorithms was checked by running various samples of single muons through the detector and trigger simulation and plotting the efficiency curves as a function of p_T, η, and ϕ.

All simulation results have loose time-of-flight (TOF) cuts applied to the time distributions on all scintillation counters. PDT and MDT centroids are found using hits in 3/4 decks in the A layer and 2/3 decks in the B and C layers. Full efficiency and no electronic noise hits are assumed for all detectors. We do not yet have trigger algorithms using the more complicated geometry of the central bottom octants and so in the central region we have multiplied all rates by a factor of 8/6.

Background rates for the MTCM triggers and p_T thresholds are given in Tables 7 and 8. Recall the MTCM triggers are the sum of coincident MTC05 (scintillator) and MTC10 (wire) triggers. The rates were determined by running `GEANT` samples of one, two, four, six, and eight interaction two-jet files through the muon trigger simulator. The rates shown in the tables were found by assigning a 40mb cross section to each of the samples. A luminosity of 2×10^{32} /cm^2/s was assumed. The three, five, and seven interaction rates were taken to be equal to the four, six, and eight interaction rates respectively. The rate for each multiple interaction sample was then multiplied by the percentage that multiple interaction contributes to the total cross section assuming 132 ns bunch crossing. After multiplying by this fraction, the rates

p_T Threshold	CFT	CF MTCM	EFN MTCM
GeV/c			
2.0	4227 kHz	62 kHz	35 kHz
4.0	878 kHz	0.7 kHz	0.3 kHz
7.0	353 kHz	0.2 kHz	0.1 kHz
10.	300 kHz	0.2 kHz	0.1 kHz

Table 7: Single muon rates at $\mathcal{L} = 2 \times 10^{32}/\mathrm{cm}^2/\mathrm{s}$ assuming 132 ns bunch spacing

p_T Threshold	CFT	CF MTCM	EFN MTCM
GeV/c			
2.0	1931 kHz	1.8 kHz	0.1 kHz

Table 8: Dimuon rates at $\mathcal{L} = 2 \times 10^{32}/\mathrm{cm}^2/\mathrm{s}$ assuming 132 ns bunch spacing

for each interaction were summed.

For all but the lowest threshold, these triggers require only a fraction of the total 10 kHz available bandwidth at Level 1. We conclude that the trigger system as currently designed will meet our goals of being able to trigger, without prescales, on single muons with transverse momenta $p_T \gtrsim 8\,\mathrm{GeV/c}$ and on dimuons with $p_T \gtrsim 3\,\mathrm{GeV/c}$.

4.7 Cost Estimate

The cost estimate for the muon system upgrade is summarized in Table 9. The existing CMSC C-layer scintillator (the Run I Cosmic Cap) counters have already been paid for and their \$1,056k M & S cost does not appear in Table 9.

Central Muon Detectors	M & S Cost
CMSC Bottom Counters	275
CMSC A-layer Counters	522
Upgrade LVPS and Cable Plant	168
Forward Muon Detectors	**M & S Cost**
MDT Detectors	1,158
FMSC Counters	1,759
Electronics	**M & S Cost**
WAMUS Front Ends	901
MDT Front Ends	1,830
CMSC and FMSC Front Ends	426
Movable Counting House Readout	430
Total Cost	**7,469**

Table 9: Cost estimate, in thousands of dollars, for the muon system upgrade.

5 Level 2 Trigger

5.1 Introduction

The DØ upgrade trigger system builds upon the existing system in place for Run I, and was described in our April 17, 1995 submission to the PAC. The Run I trigger proceeds by a multi-stage set of decisions. Level 0 is an inclusive interaction trigger based on scintillator hodoscopes in the forward directions. Level 1 is a deadtimeless trigger based on calorimeter and muon PDT inputs operating in about 3 μs. Increased power is provided by the so-called Level 1.5 trigger system, based on processors operating in the 100 μs time frame, which refines muon information and allows more flexible construction of electron and jet objects. The final stage of triggering is done at Level 2 with a farm of VAX processors in which a fully assembled event can be analyzed with variants of offline algorithms.

The upgrade trigger system proposed originally in outline in 1990, and approved by the Laboratory in 1991, simply extends the power of these systems to meet the increased event rates and shorter bunch crossing times – and rationalizes the naming convention, with the old Level 1.5 becoming Level 2 (L2), and the old Level 2 becoming Level 3 (L3). The upgrade Level 1 (L1) systems, described and approved previously, operate in a few μs upon the trigger signals from single detector systems — calorimeter, fiber tracker/central preshower, forward preshower and muon detectors. The L2 system described here makes decisions on the scale of a few hundred μs, typically combining information from several detectors to give refined information about physics objects present in the event. The L3 system remains a software trigger based on sophisticated algorithms operating on the full event.

The specifications for the input rates at each level of the upgrade triggering are: 10kHz out of L1: $\sim$ 1000 Hz out of L2, and $\sim$ 10 Hz out of L3. The L2 system must operate with deadtime less than a few percent, while providing a factor of 10 rejection. The combined effect of the trigger system is to reduce the raw inelastic collision rate by a factor of about 10^6 to identify the interesting physics candidate events.

The L2 system described below obtains its rejection power by considering the correlations between trigger information from different detectors. We expect the specific correlation algorithms to evolve as experience is gained and new physics is added to the menu. The generic algorithms are those of matching spatial information in different detectors, and in computing correlations (mass, etc.) for multiple objects. Specific examples envisioned include:

calorimeter – tracker matches; preshower – calorimeter matches, determination of jet parameters with reasonable jet cone definitions, determination of E/p, and rough mass calculations for dileptons, di-jets, lepton–jet, etc.. We require the L2 trigger to have a high degree of flexibility for implementing new algorithms that are necessary to address new physics. In Run I, this flexibility paid off in many instances – new triggers for rapidity gap events, for specific η-region muons and di-muons, and for dijet events, were all introduced rapidly and efficiently as the physics concerns dictated. It was also extremely useful in coping with the large range of instantaneous luminosities in Run I.

Our understanding of the rejection power afforded by the cross-detector algorithms operating in L2 has been developed through simulations and experience with Run I data. These rejection factors have been presented in earlier submissions to the PAC (April 1995) and give good understanding that the overall bandwidth goals are achievable in the face of the high rates and multiple interaction environment. The simulations are based on our understanding of the character of the signals available to the L2 system from L1 or the detector trigger outputs.

Since the last PAC submission, the understanding of the trigger system has been solidified with detailed timing simulations of the overall trigger system, which have led to the incorporation of L2 preprocessors which prepare lists of compacted information for transmission to the event processors. This feature is crucial in allowing affordable data transfer rates. We have adopted the design principle that generic choices for preprocessor and global processor hardware and software should be made to avoid the design and fabrication of expensive one-of-a-kind devices.

5.2 Requirements for the L2 Trigger

5.2.1 Outline of the L2 system

Many different arrangements can be thought of for the various components in the L2 Trigger and we have considered several of them. The case of a processor farm has been studied in some detail and based on those studies we have arrived at the current design. This system will consist of a set of preprocessors, which are detector specific and prepare the information to be sent to global processors. The global processors each work on one event at a time. An overview of this system is shown in Figure 37. In the following we describe the system in more detail.

The principal choice made in the L2 Trigger design was to not directly

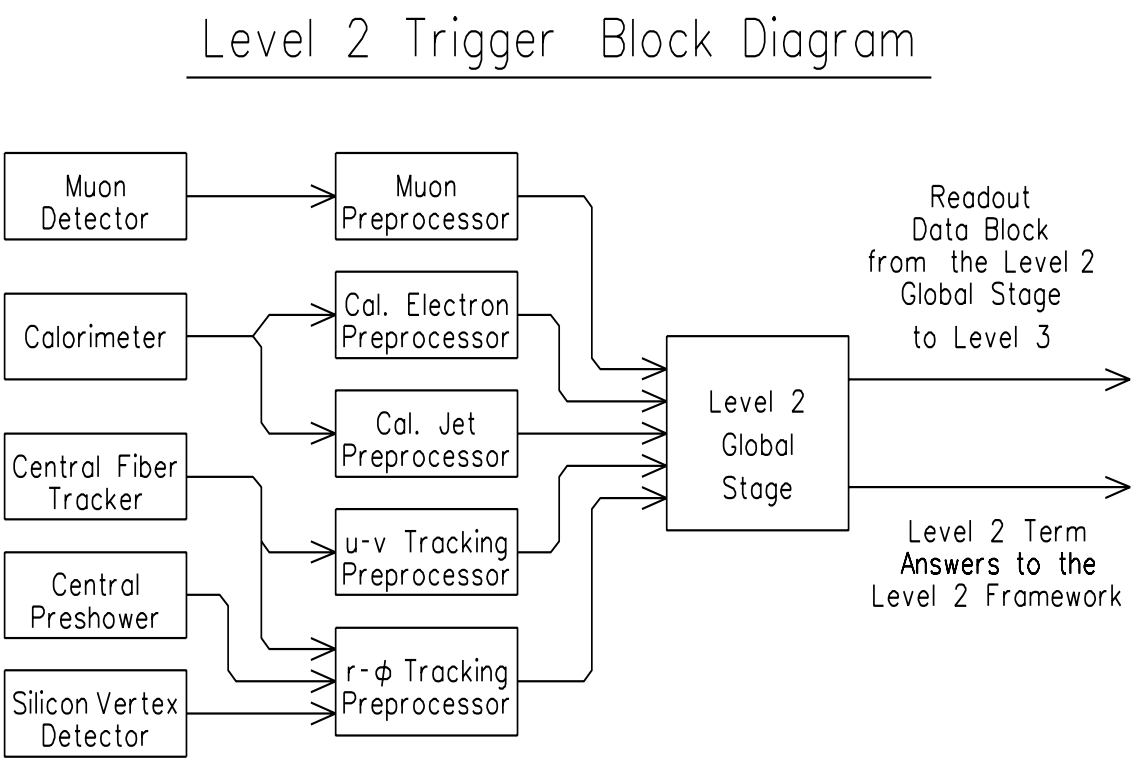

Figure 37: Overview of the L2 trigger components

work with the raw detector data but rather with "concentrated" information from the detectors. This choice is dictated by the very limited time available for the L2 system to reach a decision. The concentrated information is available from either the L1 Trigger system for a detector or else from the detector front-end (FE) through a special preprocessor. As shown in Fig. 37, each major detector system: muon, calorimeter, tracking (CFT), preshower and silicon vertex (Si) feeds data into a specific preprocessor. The result of each preprocessor is a list of candidate objects from that specific detector: muons, electrons, jets, tracks and secondary vertices. The number of preprocessors is limited and is determined by the number of detector systems.

5.2.2 Timing studies of the L2 system

A major requirement of the L2 system is to introduce a minimal amount of deadtime (<1%). To estimate this we have simulated the deadtime in the L2 trigger using a modeling package based on queuing theory. Many different simulations have been performed and we describe a representative one with realistic choices of parameters. In this simulation we have fixed the preprocessor times for different detectors as shown in Fig. 38; these include a cutoff on the processing time. For each distribution shown, the first time listed is the mean processing time for an exponential time distribution, and the second one is the data latency. The exponential time distribution was chosen

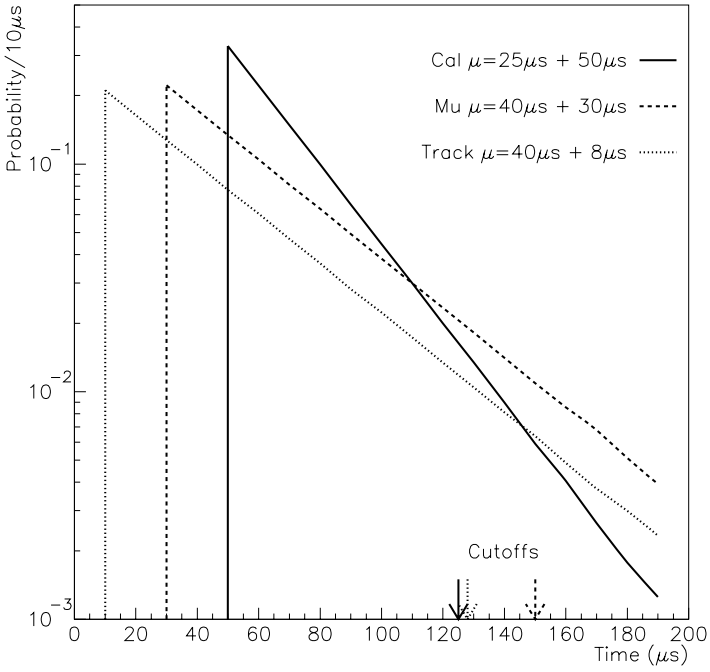

Figure 38: Distribution of the processing time/event in different preprocessors: muon (Mu), calorimeter (Cal) and tracking(Track).

because it has a moderately long tail with about 5% of the cumulative distribution above a cutoff of three times the mean. This is fairly conservative, and to maintain our conservative stance we charge the data latency against the total time of the preprocessors. By fixing the time of the preprocessors we can explore the requirements for the global processor. For all of the studies we will describe below, we have assumed a L1 accept rate of 10 kHz and a single global processor.

In Fig. 39 we show results from some of our studies. The solid and dashed curves show the effect of the tail on the processing time of the preprocessors. For reference, the deadtime for a mean global processing time of $80\mu s$ is $\sim 3.7\%$ if we apply the cutoff on the preprocessor time and $\sim 6.4\%$ if we do not apply a cutoff. As can also be seen from this plot, the two curves are converging as the mean global processing time increases. This is to be expected as increasing the mean processing time in the global processor begins to overshadow the time spent in the preprocessor. (The apparent dip in the curves around 60 μs is an artifact of a simple spline fit to the data points.) Another parameter we have investigated is the transfer time from the preprocessors to the global processor. We have assumed the memory for this transfer is local to the global processor and, thus, charged the transfer time against the preprocessors. The dotted curve in Fig. 39 illustrates this effect for an assumed transfer time of 10 μs. At a mean global processing

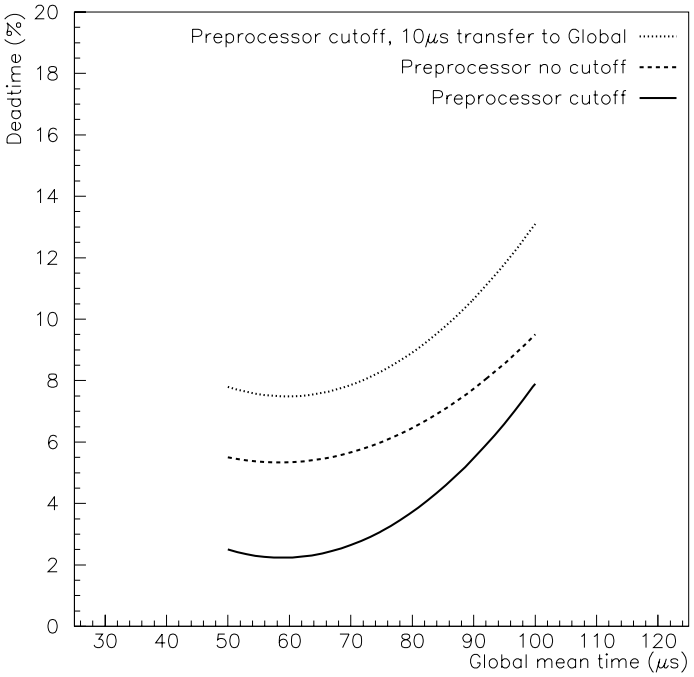

Figure 39: Deadtime as a function of processing time/event in the global processor for different assumptions.

time of 80 μs we find a deadtime of $\sim 8.8\%$ which can be compared directly with the $\sim 3.7\%$ from the solid curve. Again, these two curves are converging as the mean global processing time increases.

In addition to the preceding studies, we have also investigated the effects of processing time correlations between the preprocessor and the global processor. These correlations arise from events that produce many candidates in the preprocessor. For a mean global processing time of 80 μs we find a deadtime of $\sim 5\%$ compared with $\sim 3.7\%$. This effect now grows with mean global processing time so that the curves diverge.

Simulations like this have provided guidelines for the processing time available in the preprocessor and global processor to complete an event. Typically this time is of order 30-40 μs in the preprocessor and about 70 μs in the global processor.

5.2.3 Preprocessor tasks and time estimates

5.2.4 Muon preprocessor

The muon preprocessor is designed to find objects in the muon system using the digitized data for all the muon detectors, and report segments of muon tracks to the global L2 processor. The muon preprocessor will divide the muon system into geographically separate pieces consisting of 45 degree segments in ϕ in either the central or one forward region of the detector. The muon preprocessor is anticipated to require up to 20 μs for serial input from the detector, 20 μs for internal data transfer and buffering, 30 μs for calculations, and 20 μs for serial output to the global L2 processor.

In the central region the muon preprocessor input will be the drift time information from the wide-angle muon system drift tubes (WAMUS) and the time information from the central muon scintillator (CMSC) A and C-layer detectors. The preprocessor will consider groupings of drift times consistent with L1 muon trigger centroids in the WAMUS chambers and then use the drift times to calculate a position in z and an angle in $r-z$ for a straight line segment. For good segments the drift time information will be used to extract a delta-time measure of the position along the wire which will give a coordinate in the ϕ-direction and an angle in r-ϕ. The segment coordinates will point at an element of scintillator, and the segment will be tagged with the time for that element of scintillator, including any correction to the scintillator time for time-of-flight. Separate segments will be found inside and outside the iron toroid magnet.

Studies of algorithms have begun for the central inner segments. Samples of data from Run I were scanned and separated into good and bad muons. Events were required to have a L1 trigger centroid before the impact of the L2 preprocessor algorithm was determined. For 95 % efficiency on the good muons, a rejection factor of 7.8 on the background was measured. A study of scintillator timing found that with 99 % efficiency a rejection of 5 was possible.

In the forward region the input to the muon preprocessor will be the forward muon system drift tubes (FAMUS) and the forward muon scintillator (FMSC). The FAMUS data will come from the L1 input centroids from the MCEN cards and will not include the full drift time, but will include a pattern reference as well as position. The preprocessor will convert the MCEN output into an x- or y-coordinate from the beam and an angle between that coordinate and the z-direction. There is no wire information in the other coordinate, so that coordinate will be found using the position of the FMSC element with the time most consistent with the interaction. The matching

scintillator time(s) will be tagged to the segment with any corrections. As in the central region, separate segments will be found inside and outside the toroid.

The output of the muon preprocessor in all regions is a list of segments from all regions including the position and angle of the segment, quality of fit and scintillator time(s). By providing individual segments the global processor will be able to have the maximum efficiency for keeping muons that may miss either an inner or outer layer while having sufficient information in the calorimeter or fiber tracker to identify them as good muons.

5.2.5 Calorimeter preprocessor

The L1 calorimeter trigger is based on the transverse energy deposition in trigger towers covering 0.2×0.2 in $\Delta\eta \times \Delta\phi$. The minimum transverse energy(E_T) required in a trigger tower can be set as can the number of trigger towers above the threshold. Electromagnetic objects can be triggered on by putting a threshold on the minimum amount of transverse energy deposited in the electromagnetic portion of a trigger tower. This trigger is implemented out to $|\eta| \leq 4.0$, giving a total of 1280 trigger towers.

L2 will need to trigger on both electromagnetic (EM) objects and on hadronic (HAD) objects. The goal for the L2 preprocessors is to send object information to the global L2 processor within 100 μs. Given these time constraints on the L2 preprocessor, we will use two calorimeter preprocessors, one for electrons/photons and one for jets. Each preprocessor will use the E_T data in the 1280 trigger towers. In addition, the trigger towers (*seed towers*) which passed the specific L1 E_T threshold for each trigger, will be available to the L2 calorimeter preprocessors.

Since the L1 trigger information is available to the L2 preprocessors, we can save time by running the algorithm only once over each seed, using the lowest common thresholds of all triggers which passed at L1. The resulting objects (electrons, photons, jets) passing these "least common denominator" requirements will then be passed to the global L2 processor which will make decisions for each specific trigger based on the thresholds relevant to that trigger.

Finding objects in the L2 calorimeter preprocessors consists of several tasks, each of which will take a certain amount of time. The tasks include (i) getting the trigger tower data into the preprocessors ($\sim$ 13 μs), (ii) unpacking the L1 trigger information to get the η and ϕ position of the seed towers ($\sim$ 3 μs), (iii) running the object algorithm and (iv) creating the block of output data to be sent to the global L2 processor ($\sim$ 10 μs).

At the beginning of Run II, the Tevatron will operate with bunch crossings spaced 396 ns apart. With this spacing of the bunch crossings, the amplitude of the calorimeter trigger tower signals will be proportional to the energy deposited in the calorimeter from a single bunch crossing. Later in Run II, when the Tevatron begins operating with bunch crossings separated by only 132 ns, there is the possibility that it will take a few bunch crossing periods for the trigger tower signals to reach their full response due to the energy deposited in the calorimeter by a single bunch crossing. In this case, we anticipate that the L2 calorimeter preprocessor will need to read in and manipulate trigger tower information from several bunch crossings in order to extract the signal from the bunch crossing that actually caused the L1 trigger. We make the assumption that we will need to use information from four bunch crossings around the bunch crossing that caused the L1 trigger. Therefore, the time required by the L2 calorimeter preprocessor to complete certain of its event processing steps will increase by a factor of four.

The timing studies for the calorimeter preprocessor algorithms were done in the C programming language running on a Digital 3000/M300 ALPHA machine ($\sim$ 100 MIPS). Algorithms for finding electrons and jets similar to the ones used in Run I were coded and used to determine the processing times required. The total times for the calorimeter preprocessors are summarized in Table 10. The data input time shows a range due to four bunch crossings assumed needed at 132 ns. The algorithm time, which is described in detail below, is shown for an average event and the range again indicates the time assuming four bunch crossings are needed. The expected preprocessor times are comfortably within our time budget for 396 ns bunch crossings. At 132 ns, we will be pushing the system to its limit and will need all the time improvement we can get by using the fastest processor and fastest data input available.

	Electrons	Jets
Data Input	$13 - 50$ μs	$13 - 50$ μs
Unpacking seed info	3 μs	3 μs
Mean algorithm/event	$5 - 20$ μs	$15 - 60$ μs
Output data creation	10 μs	10 μs
Totals	$30 - 83$ μs	$41 - 123$ μs

Table 10: Calorimeter preprocessor time estimates.

Calorimeter: Electron/Photon Algorithm

The electron (and photon) algorithm consists of the following steps:

- Form a 1×2 (trigger towers) cluster from each seed using its highest E_T neighbor and compare this sum to the lowest threshold needed by the electron or photon triggers which passed L1.
- Compare the EM fraction of the 1×2 cluster to the lowest common EM fraction threshold. The EM fraction is defined as the ratio of the cluster EM E_T to the cluster total E_T (EM+HAD).
- Compare the isolation fraction of the 1×2 cluster to the lowest common isolation fraction threshold. The isolation fraction is defined as the ratio of the cluster EM E_T to the total E_T sum of a 3×3 cluster.
- Compare the number of EM clusters passing the above requirements to the minimum number of EM clusters required.

As can be expected, the algorithm time is highly correlated with the number of seeds. Since the latter steps in the algorithm are not run unless the EM cluster passes each previous step, there is a characteristic spread in the time distribution. For events with a single seed, the time distribution to run the electron algorithm for typical EM requirements is given in Fig. 40. The requirements were: 7 GeV EM E_T seed at L1, 10 GeV 1×2 cluster E_T, EM fraction of 0.80, and isolation fraction of 0.01. The average time is ~ 2.8 μs. About 1.0 μs of that time is for algorithm overhead. Each additional seed adds ~ 2.1 μs to the average time and EM seed multiplicity (for 7 GeV seeds) is on the order of $1 - 2$ seeds per event. The seed multiplicity, and hence algorithm time, increases slowly with luminosity.

Calorimeter: Jet Algorithm

The jet algorithm consists of the following steps:

- Form a 5×5 (trigger towers) cluster around each seed tower and compare this E_T sum to the lowest common jet E_T threshold needed by the jet triggers which passed L1.
- Order the clusters in E_T and check for any overlapping clusters (where overlapping is defined as having the center tower in the cluster within another cluster), keeping the higher E_T cluster as a jet.
- Compare the number of jets to the minimum number of jets required.

As with the electron algorithm, the jet algorithm time is very dependent on the number of seeds. However, as the number of seeds increases, so does the number of clusters above the jet E_T threshold which then need to

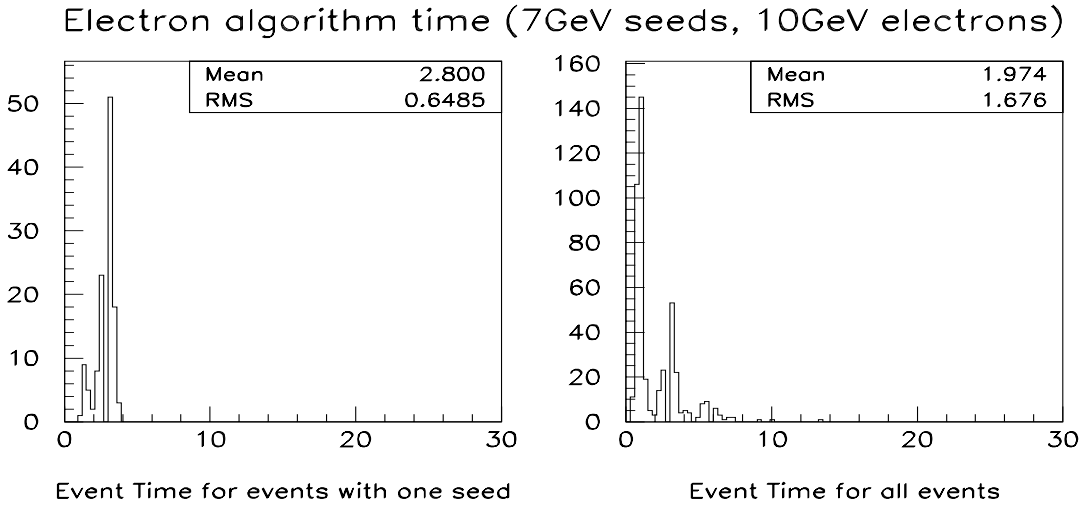

Figure 40: Event time for L2 Calorimeter preprocessor for electrons with a single (7GeV) seed in the event and for all events.

be checked for overlaps. Hence, there is also a dependence on the number of clusters. The average algorithm time for an event with a single 3 GeV seed and a cluster E_T threshold of 15 GeV is comparable to the electron algorithm, ~ 3.0 μs. Each additional seed adds ~ 2.2 μs to the average time with another ~ 1.1 μs from the increase in cluster multiplicity. The average seed multiplicity for 3 GeV seeds and low luminosity is ~ 3, growing to ~ 6.0 at high luminosities. Seed multiplicity for jets depends more on luminosity than in the electron case. The lower seed threshold, which applies to total trigger tower E_T (EM+HAD), is more easily reached due to the additional energy in the calorimeter from the multiple minimum bias events underlying the hard interaction. Hence, the total event time for jets is larger and the tail is much broader than for electrons.

5.2.6 Tracking preprocessor

The L1 central fiber tracking (CFT) trigger allows up to 6 track candidates in each of the 80 ϕ sectors of the tracking system. This multiplicity of candidates allows a minimum p_T threshold of 1.5 GeV up to the highest luminosities with high efficiency. For each track candidate the addresses of the axial fibers($r-\phi$) with u-v fiber (4 layers) information will be sent to the L2 tracking preprocessor for each L1 trigger. The u,v layers are at a ± 2degree stereo angle. In addition, the preprocessor will receive the p_T thresholds used in the L1 trigger for individual events and will use this information to determine which subset of L1 candidates to process.

For the track candidates surviving these criteria, the information from the u-v fibers crossing the selected axial fibers, will be requested from the front ends. Combining this information with the L1 information from the axial fibers allows the formation of three dimensional tracks in r, ϕ and z. Simulations of such matching algorithms have shown a reduction of fake tracks of more than a factor of 8. In a feasibility study it has been shown that an algorithm like this, implemented in a digital signal processor (DSP), can be used and results in the above quoted rejection.

The candidates passing such a matching track algorithm will be transferred to the global stage of the L2 trigger. The information sent will consist of η, ϕ and z position of the vertex for each resulting track candidate and the candidates would be ordered in p_T.

5.2.7 Silicon vertex preprocessor

The feasibility of a secondary vertex trigger(SVT) based on information from the silicon vertex detector and tracking system is being studied actively. At the time of the writing of this document, DØ has not explored the advantages and disadvantages of an impact parameter trigger sufficiently to warrant its inclusion in the upgrade. This is actively being investigated by a group dedicated to this problem and we expect to resolve this question by the time of the next PAC meeting.

In the meantime the design of the tracking trigger is progressing, keeping in mind that it may include a possible SVT in the future. The hardware implementation of the L2 tracking trigger and L2 secondary vertex trigger is expected to be very similar. The processors are likely to be identical or at least very similar. The design of triggers and DAQ is such that all the hooks and connections for a possible SVT are in place. Given the current state of funding we do not envision starting Run II with such a trigger, but feel that it may be a candidate for a staged upgrade after the start of Run II.

5.2.8 Global processor tasks and time estimates

The role of the global processor is to combine the object information from the various detector preprocessors to evaluate the L2 terms for each L1 trigger which fired. The goal is to perform those evaluations within a time budget of 100 μs. The general methodology is that the global processor will build *scripts* describing the tasks it needs to perform from the L1/L2 trigger information. At its simplest, a script may consist of the number of each type of object needed (jet, μ, e, γ, etc); the object definition which may require

combining information from multiple preprocessors; and the object E_T, η, or ϕ requirements. From our experience in Run I, we can envision quite complex scripts to pick out interesting events. After building the scripts for the triggers which fired, the global processor will evaluate each script for each relevant object or set of objects found by the preprocessors to form its decision.

The global processor will therefore have to perform a series of wide-ranging tasks. These tasks include: (i) getting the preprocessor data into the global processor; (ii) event consistency checking; (iii) script building; (iv) manipulation of preprocessor information to complete tasks preprocessors are unable to do (e.g., matching muon track segments from different parts of the muon detectors to find muons); (v) script evaluation; and (vi) reporting result to the L2 framework and creating the block of output data to be sent to Level 3.

The average amount of data expected per event from all preprocessors has been estimated to be 528 bytes for data packed into 4 byte words. The expected data through-put rate for the proposed global L2 processor (see following discussion on hardware) is 320 Mbytes/s. Thus the data input is expected to take ~ 1.7 μs/event.

Preliminary timing studies, again on a 3000/M300 ALPHA processor, were done for the script evaluation time. These studies indicate that script evaluation takes $\sim 0.5 - 1.5$ μs per object per trigger. Given object multiplicities on the order of $2 - 3$ per event and an estimate of 5 triggers per event, implies ~ 15 μs for complete script evaluation per event.

The timing is not fully understood for most of the other global processor tasks. It is also highly likely the list of tasks for the global processor will grow both during the upgrade preparations and during Run II. Therefore, the most critical requirements for the global processor are flexibility and speed.

5.3 Proposed hardware

5.3.1 Muon preprocessors

The muon preprocessor consists of two VME crates: one interface crate and one preprocessor crate. The interface crate includes the serial link interface cards and an interface control card. The preprocessor crate includes parallel processor cards, a processor control card, and a VME Buffer-Driver (VBD) card for data transmission to Level 3.

Each serial link interface card (SLIC) includes up to 21 receivers for the 160 Mbit/s serial links used by the muon front ends. The SLIC will have sufficient memory to buffer 8 input events and then transmit the bytes to the parallel processors at 40 Mbytes/s. The buffer control and transmission to the parallel processors is controlled by the interface control card over the user-defined lines of the VME crate.

The parallel preprocessor currently considered is the CNAPS-128 by Adaptive Solutions. It is available as a 6-U VME module and has a 40 MByte/s direct I/O link and 128 parallel processors. The 128 processors are arranged in a single-instruction multiple-data (SIMD) architecture and can handle 20 million multiply-accumulate operations per second. The processor control card would be required to read the results from the CNAPS-128 cards would provide connections to the trigger framework, global L2 trigger, and L1 muon trigger.

Each CNAPS-128 requires one SLIC for the input, and to utilize the SIMD architecture, each processor would operate on a narrow road within one region. Separate processors would handle each of the four possible segment finding algorithms. The entire muon detector requires 2 central inner, 4 central outer, 2 forward inner, and 4 forward outer SLIC - CNAPS pairs. Other than the CNAPS-128 and VBD, all other cards are cutsom-made.

5.3.2 Calorimeter Preprocessors

The calorimeter L2 preprocessor will be implemented using a RISC ALPHA based trigger processor board. This method of implementation was chosen for a number of reasons. It is fast enough to complete the L2 preprocessor algorithms within the required time budget. It retains much more flexibility in allowing a wide selection of triggering algorithms than hardwired logic implementation would. The processor-based implementation costs less than a L2 preprocessor based solely on custom built specialized hardware.

The ALPHA based trigger processor board that we plan to use is being developed jointly by CDF and DØ. This development is a continuation of the ALPHA based trigger processor that CDF began using during collider Run I. The principal feature of this trigger processor design that makes it useful in our applications is its high speed input data path that can feed the same information to multiple processor boards from multiple data sources. This feature is missing from most commercial processor board designs.

The input information to the preprocessor comes from the L1 calorimeter trigger. This information consists of electromagnetic and hadronic trigger tower signals (1280 of each) and masks showing which trigger towers were over

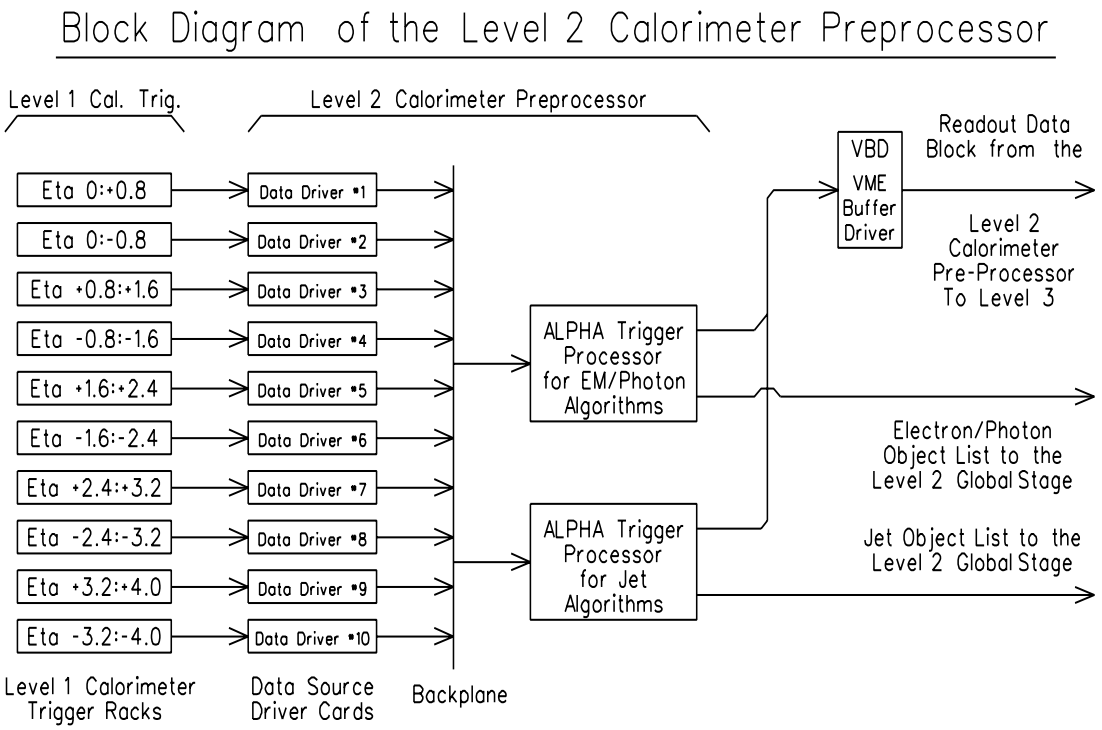

Figure 41: Input and output of the calorimeter L2 preprocessors.

the various L1 thresholds (4 EM thresholds and 4 Jet thresholds). Each of the 10 racks in the L1 calorimeter trigger delivers its section of this information to the L2 preprocessor over a separate data path. This is illustrated in Figure 41. By using these 10 data paths in parallel, all of the input information is delivered to the preprocessor in about 12 μs if only a single bunch crossing's worth of calorimeter data is needed. At the highest bunch crossing rates where the calorimeter trigger tower signals may not respond fast enough to separate the effects of individual bunch crossings, then the preprocessor may need up to 4 bunch crossings' worth of information. In this case the 10 data paths from the L1 calorimeter trigger would take about 50 μs to deliver this data to the preprocessor. The design of the data path between the L1 calorimeter trigger and the L2 preprocessor will be similar to the equipment used in Run I to feed data to the Level 1.5 calorimeter trigger.

When the data arrives at the preprocessor, it is distributed via the processor crates custom backplane to a number of the ALPHA trigger processor boards. This distribution mechanism is flexible and it will be used to simultaneously deliver the input data to two processor boards. One processor board will use this data with the Electron/Photon algorithm and the other processor board will use this data with the Jet algorithm.

When input data arrives in the preprocessor crate, it is driven onto the crate's backplane by data-source driver cards. There can be up to 15 of these data source driver cards in a crate. Memory on each of the ALPHA trigger processor boards receives this data. Up to 7 trigger processor boards may be installed in a crate. Any combination of these trigger processor boards

may be enabled to receive the calorimeter data from a particular event. The memory on the trigger processor boards can be organized as an input event FIFO. The information in this memory is directly accessible by the ALPHA processor on each of the trigger processor boards and it is also visible over VME for readout or diagnostic purposes.

There are two outputs from the preprocessor. One output is the Lists of Identified Objects (Electron/Photon and Jet) that the preprocessor sends to the L2 Global Stage. The other output is a readout to the Level 3 DAQ system. The readout to Level 3 DAQ uses the same setup and equipment as is used by all of the other data sources to the DAQ system (e.g. detector front-end crates).

5.3.3 Tracking preprocessors

The information from all the central tracking front end systems is transmitted to the counting house over fast optical serial links. A passive optical splitter near the destination will split each link into two and the second link will be routed to the L2 preprocessor input. This can easily be done for all the central tracking systems (fibers, silicon and central preshower), because they all read out by means of the SVX readout chip.

The L2 system obtains the data through 16 receiver modules, located in two VME crates. Each VME crate contains 7 processor boards for performing the track matching described earlier. The requirements for these boards are well established at this time and they will probably be commercially available DSP based processor boards with high bandwidth I/O capability.

5.3.4 Data transfer

Each of the L2 preprocessors sends its list of identified objects (LIO) to the L2 Global Stage. Each list begins with a header which contains the L1 trigger number of the event and other flags (e.g. the number of entries in the following list). This header allows the Global Stage to verify that each preprocessor has sent data to it from the proper L1 accept.

For some subset of the L1 triggers, the LIO from a particular preprocessor may not be required for making the trigger decisions in the L2 Global Stage or for subsequent analysis of the event in the Level 3 stage. For those events where only L1 triggers from this subset have fired, then this particular L2 preprocessor does not need to actually process the event. However, it still must transfer a header to the Global Stage for this event. The header indi-

cates the L1 trigger number of the event and flags that the preprocessor did not actually analyze the event. Because for every event, every preprocessor sends to the Global Stage a data block consisting of a header plus normally a LIO, it is a simple job for the Global Stage to implement its input buffering. The Global Stages input buffer is setup as an event FIFO. Each of the preprocessors sends its data block for a given event to the Global Stage asynchronously as soon as it has completed its work on that event. When the Global Stage is ready to begin processing of a given event, it pulls from its side of the FIFO buffers the next data block from each of the preprocessors. The first step in the L2 Global Stage's processing of a new event is to examine the headers from the data blocks from all of the preprocessors to verify that they contain the proper L1 trigger number.

5.3.5 Global processors

The Global Stage of the L2 trigger uses information from the various L2 preprocessors (the LIO) to evaluate L2 terms. For each event, the L2 Global Stage is told by the L2 Framework which L2 terms the Global Stage will need to evaluate in order for the L2 Framework to make the Accept/Reject decisions for each of the L1 Triggers that fired on a given event. In this way, the Global Stage only performs the work that is actually necessary for the L2 Accept/Reject decisions to be made for each event.

The L2 Global Stage uses the same ALPHA-based trigger processor hardware as is used in the calorimeter preprocessor. The block diagram arrangement of these two systems looks similar. Each of the L2 preprocessors sends its data to the Global Stage over a link that connects to a Data Source Drive Card(DSDC) on the backplane in the Global Stage's crate. These DSDC's can distribute the information from the preprocessors in a flexible way. If the work performed in the Global Stage is relatively simple, a single processor board can handle it. If this work is more complicated, the same preprocessor information can be sent to two or more processor boards with each of the processor boards working to evaluate a subset of the L2 Terms.

The output from the L2 Global Stage consists of two parts. One output is the L2 term answers. The Global Stage returns to the L2 Framework the pass/fail answers to all of the L2 terms that it was asked to evaluate for each event. The other output is the data block that the Global Stage sends to the Level 3 DAQ system for events that have been passed by the L2 Framework. This data block from the L2 Global Stage will contain information about why its was able to pass or fail each of the L2 Terms that it evaluated for a given event.

5.4 Cost Estimate

While the L2 system design will evolve somewhat in the next year, it has become better defined in the last 4 months. Based upon the current system architecture, module counts, our experience with the Level 1.5 trigger for Run I, and emphasizing the use of commercially available products and developing a high speed VME based processor with CDF, we feel reasonably confident about the cost estimates for the system. The total estimated M&S cost for the full L2 system is summarized in Table 11. The estimated need for engineering and design is approximately fifteen FTE-years, most of which we anticipate to come from the staff of collaborating institutions in the U.S. and abroad.

Muon preprocessors	\$340k
Calorimeter preprocessors	\$270k
Tracking preprocessor for $(r-\phi)$	\$170k
Tracking preprocessor for stereo $u-v$	\$450k
Global processor stage	\$170k
Totals	\$1,400k

Table 11: M&S budget summary for the Level-2 trigger system.

6 Summary and Conclusions

We have described the Forward Preshower, Muon System and Level 2 Trigger of the DØ Upgrade detector.

Many measurements that we intend to carry out in Run II require acceptance for leptons over a large rapidity region. In order to fully exploit the capabilities of the DØ detector we must be able to trigger on electrons in the end calorimeters. Without the FPS, the upgraded detector would only have the same trigger capabilities as the present detector in this region. This would be inadequate at the high luminosities expected for Run II and would result in prescaled triggers for many important measurements. We have described the design of Forward Preshower Detectors which will improve the rejection for electron triggers in the end calorimeter region by factors of 2–4 at Level 1 and 3–7 at Level 2. In addition they will also augment the electron and photon identification capabilities of the DØ detector during offline analysis. These detectors will cover the region $1.4 < |\eta| < 2.6$ in pseudorapidity and fit smoothly against the cryostats of the End Calorimeters. They will consist

of a lead converter sandwiched between planes of scintillator detectors. The scintillator planes are segmented in a u-v geometry and consist of triangular strips that are read out with wave length shifting fibers and VLPCs. In total the detectors will have about 16,000 channels. Our estimate of the cost of the FPS detectors is \$632,200 for the detector and \$620,000 for the VLPC readout.

Just as in the case of electrons, the physics goals of Run II demand uniform geometric accpectance and an efficient trigger for muons beyond $|\eta| \sim 1$. Based on experience and data from Run I, the present proportional drift tubes (PDT's) of the wide angle muon system will not survive the luminosities of Run II in the forward region. In light of this, we have developed a muon system upgrade that will replace them with three layers of plastic Mini-Drift Tubes (MDT's) in the region $1 < |\eta| < 2$. MDT's offer good radiation resistance, relatively fast time response, and adequate resolution. New electronics will be used for both the PDT's and MDT's. A thick iron, lead and polyethylene shield will surround the beam line where sprays of background particles are most intense: the low beta quadrupole and the exit of the End Calorimeter. (To be effective, the shielding necessarily displaces the present small angle SAMUS stations and defines the Run II muon pseudorapidity coverage to be $|\eta| < 2$.) The shielding will reduce the energy deposited by non-muon backgrounds in the forward chambers by a factor of 100, thus lowering both radiation damage and accidental trigger rates. Scintillator planes will be added both in the central and forward regions, to associate muon tracks with particular crossings and to form the trigger. We have demonstrated that at $\mathcal{L} = 2 \times 10^{32}$ cm^{-2} s^{-1} we will be able to use an unprescaled trigger on single muons with transverse momenta $p_T \gtrsim 8$ GeV/s and dimuons with $p_T \gtrsim 3$ GeV/c. The total cost estimate of the muon system upgrade is \$7,469,000, excluding contingency.

The Level 2 Trigger must reduce the 10 kHz rate from the first level trigger by a factor of 10, while introducing less than a few percent deadtime. The system proposed consists of five preprocessors acting on the data from subdetector systems and feeding "concentrated" information to an array of global processors (each of which works on one event at a time). The global processor considers correlations between the trigger information from the different subdetectors to realize the necessary rejection. The processing time available is 30–40 μs in the preprocessors and about 70 μs in the global processor. We have outlined the preprocessor algorithms, time estimates and hardware. The cost estimate for the L2 system is \$1,400,000.

References

[1] "The DØ Upgrade", unpublished (1990);
"P823 (DØ Upgrade): Responses to the Physics Advisory Committee" DØ note 1148 (1991);
"E823 (DØ Upgrade): R& D and Optimization Progress Report, DØ 1322 (1992);
"E823 (DØ Upgrade): Step-1 and Beyond", DØ 1421 (1992);
"E823 (DØ Upgrade): DØ$_\beta$", DØ 1733 (1993);
"E823 (DØ Upgrade): Magnetic Tracking", DØ (1993);
"The DØ Upgrade", DØ Note 2542, Fermilab-FN-639 (April 1995);
"The DØ Upgrade: Forward Preshower, Muon System, Level 2 Trigger", (January 1996).

[2] For a review, see "The Standard Model and Beyond," DØ Collaboration, Fermilab-FN-640 (December 1995).

[3] U. Baur, S. Errede, G. Landsberg, Phys. Rev. **D50** 1917 (1994).

[4] G. Landsberg in "Report of the *tev_2000* Study Group on Future Electroweak Physics at the Tevatron," D. Amidei and R. Brock (eds.), DØ Note 2589.

[5] J. Ellison in "Report of the *tev_2000* Study Group on Future Electroweak Physics at the Tevatron," D. Amidei and R. Brock (eds.), DØ Note 2589.

[6] "The Muon Upgrade Intermediate Eta A-Layer Scintillation Counters," H.T. Diehl *et al.*, DØ Note 2719.

[7] CTEQ Collaboration (J. Botts *et al.*), Phys. Lett. **B304** (1993) 159.

[8] A.D. Martin, R.G. Roberts and W.J. Stirling, Phys. Lett. **B306** (1993) 145; **B309** (1993) 492(E).

[9] CDF collaboration, (F. Abe *et al.*), Phys. Rev. Lett. 74, 850 (1995).

[10] R. W. Brown et al., Phys. Rev. **D20**, 1164 (1979); K. O. Michaelian et al., Phys. Rev. Lett. **43**, 746 (1979).

[11] DØ Collaboration (S.Abachi *et al.*), FERMILAB-Pub-95/385-E, accepted by Phys. Rev. Lett.

[12] G. Landsberg, DØ note 2709.

[13] DØ Collaboration (S.Abachi *et al.,*), FERMILAB-Pub-96/072-E, March 1996, submitted to Phys. Rev. Lett.

[14] M. Adams *et al.*, "A Detailed Study of Plastic Scintillating Strips with Axial Wavelength Shifting Fiber and VLPC Readout", FERMILAB Pub-95/027 (July, 1995); M. Adams *et al.*, "A New Detector Technique Using Triangular Scintillating Strips to Achieve Precise Position Measurements for Minimum Ionizing Particles", FERMILAB Pub-95/285-E (October, 1995); "Design Report of the Central Preshower Detector for the DØ Upgrade", M. Adams *et al.*, DØ Note in preparation.

[15] D. Adams *et al.*,, FERMILAB-Conf-94/318-E; M. Atac *et al.*, *Nucl. Instr. and Meth.* **A314** (1992) 56; M.D. Petroff and M.G. Stapelblock, *IEEE Trans. Nucl. Sci.* **NS-36** (1989) 158; M.D. Petroff and M. Atac, *ibid.*, p. 163.

[16] "Characterization of the SVXIIb Chip", B. Abbott *et al.*, DØ Note 2842 (February, 1996).

[17] "Timing Resolution and Linearity Measurements for a Scintillating Fiber Detector Instrumented with VLPCs", A. Bross *et al.*, *Nucl. Instr. and Meth.*, to be published.

[18] S. Margulies and M. Chung, "Development of a Multi-channel Fiber-to-Fiber Connector for the DØ Upgrade Tracker", Conference Record, *1995 IEEE Nuclear Science Symposium*, 1995 (in press).

[19] S. Margulies and M. Chung, "Fabrication and Testing of Clear Light-guide Fiber Bundles for the DØ Prototype Fiber Tracker Cosmic Ray Test", in *Scintillating Fiber Technology and Applications II*, E.J. Fenyves, ed., *Proc. SPIE* 2551, pp. 2-9 (1995).

[20] S. Margulies and M. Chung, "Estimation of Radiation Doses in the DØ Upgrade Scintillating Fiber Tracker and Central Preshower Counter", DØ Note 2394 (1994).

[21] "DØ Muon Chamber Pulse Heights: June 1992 to September 1994 Shutdown," J.M. Butler, DØ Note 2319.

[22] `http://www-d0.fnal.gov/~darien/darien.html`

[23] "Crud Removal from Muon Drift Chamber Wires Using 'Zap' Cleaning," T. Marshall and H. Haggerty, DØ Note 2556.

[24] "DØ-SAMUS background simulations", N. Mokhov, DØ Note 721, Fermilab 1988.

[25] J.M. Butler *et al.*, "Reduction of Tevatron and Main ring induced backgrounds in the DØ detector", DØNote 2559, FNAL TN-629, Fermilab, 1995.

[26] "Simulation of the test shielding in the DØ forward muon system", S. Striganov, DØ Note 2711, Fermilab 1995.

[27] H. T. Diehl, "Aggressive Shielding Strategies for the Muon Upgrade", DØ Note 2713, September 1995.

[28] N. V. Mokhov and V. Sirotenko, "Possible Minimal Solutions for DØ Detector Shielding Based on GCALOR and MARS13 Simulations", DØ Note 2601, July 1995.

[29] U. Baur and D. Wood in "Report of the *tev*_2000 Study Group on Future Electroweak Physics at the Tevatron," D. Amidei and R. Brock (eds.), DØ Note 2589.

[30] "Muon System Pixel Trigger Rates in EF," D. Green, DØ Note 2551.

[31] "High P_t Single Muon Trigger Rate Estimates for the Intermediate Eta Region During Run II," H.T. Diehl, DØ Note 2605.

[32] "Progess on DØ Detector Shielding Optomization with GCALOR",V. Sirotenko, DØ Note 2835.

[33] R. Brock, "DØ Full Scintillator Coverage", Report to a Review Panel, May 1992.

[34] H. T. Diehl and S.C. Eno *et al.*, "Proposal for Central Muon A-Layer Scintillator Trigger Counters", DØ Note 2213, January 1995.

[35] G. Alexeev *et al.*, " Studies of stability and systematics of operation of the DELPHI plastic tubes", NIM, A292, 551, 1990.

[36] S. Boyarinov *et al.*, "Neutron and gamma sensitivity of gas detectors", GEM-TN-93-345, SSCL 1993.

[37] B. Baldin *et al.*, "Upgrade of the DØ forward muon system with pixel scintillation counters", IEEE Transaction on Nuclear Science, No. 4, August 1995, pp. 736-742.

[38] Yu. Nikolaev *et al.*, "The efficiency of plastic scintillators to neutrons and gammas", SDC-93-512, SSCL 1993.

[39] B. Baldin, *et al.*, "DØ Upgrade Muon Electronics Design", IEEE Transactions on Nuclear Science, Vol 42, (1995) 736.

[40] Y.Arai, F.Sudo and T.Emura, "Developments of Time Memory Cell VLSI's." KEK Preprint 93-49, June 1993 H.

[41] J.M.Butler *et al.*, Nucl. Inst. Meth. **A290** (1990) 122.

[42] DØ Collaboration (S. Abachi *et al.*), Phys. Rev. Lett. **74** (1995) 3548.